



Engineering Considerations for the Self-Energizing Magneto-plasmadynamic (MPD)-Type Fusion Plasma Thruster

Chan K. Choi
Larry T. Cox

Purdue University
School of Nuclear Engineering
1290 Nuclear Engineering Building
West Lafayette IN 47907-1290



August 1994

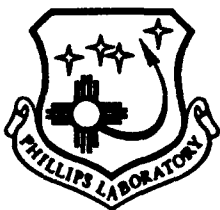
98px 94-27941

Final Report

APPROVED FOR PUBLIC RELEASE; DISTRIBUTION UNLIMITED

94 8 29 235

DTIC QUALITY INSPECTED 8



PHILLIPS LABORATORY
Propulsion Directorate
AIR FORCE MATERIEL COMMAND
EDWARDS AIR FORCE BASE CA 93524-7001


NOTICE

When U.S. Government drawings, specifications, or other data are used for any purpose other than a definitely related Government procurement operation, the fact that the Government may have formulated, furnished, or in any way supplied the said drawings, specifications, or other data, is not to be regarded by implication or otherwise, or in any way licensing the holder or any other person or corporation, or conveying any rights or permission to manufacture, use or sell any patented invention that may be related thereto.

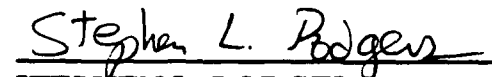
FOREWORD

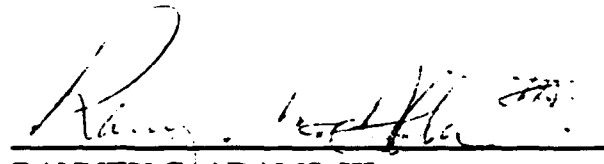
This report was prepared by Purdue University, West Lafayette IN, under contract F04611-90-K-0054, for Operating Location AC, Phillips Laboratory, Edwards AFB, CA 93524-7048. Project Manager for Phillips Laboratory was Dr. Franklin B. Mead.

This report has been reviewed and is approved for release and distribution in accordance with the distribution statement on the cover and on the SF Form 298.


FRANKLIN B. MEAD
Project Manager

 for
STEPHEN L. RODGERS
Chief, Emerging Technologies Branch


STEPHEN L. RODGERS
Acting Director,
Fundamental Technologies Division


RANNEY G. ADAMS, III
Public Affairs Director

REPORT DOCUMENTATION PAGE

Form Approved
OMB No 0704-0188

Public reporting burden for this collection of information is estimated to average 1 hour per response, including the time for reviewing instructions searching existing data sources gathering and maintaining the data needed, and completing and reviewing the collection of information. Send comments regarding this burden estimate or any other aspect of this collection of information, including suggestions for reducing this burden to Washington Headquarters Services, Directorate for Information Operations and Reports, 1215 Jefferson Davis Highway, Suite 1204, Arlington, VA 22202-4302, and to the Office of Management and Budget, Paperwork Reduction Project (0740-0188), Washington DC 20503.

1. AGENCY USE ONLY (LEAVE BLANK)		2. REPORT DATE August 1994		3. REPORT TYPE AND DATES COVERED Final July 1992 - Dec 1993	
4. TITLE AND SUBTITLE Engineering Considerations for the Self-Energizing Magnetoplasma dynamic (MPD) - Type Fusion Plasma Thruster				5. FUNDING NUMBERS C: F04611-90-K-0054 PE: 62302F PR: 3058 TA: 00AF	
6. AUTHOR(S) Chan K. Choi Larry T. Cox, Jr.					
7. PERFORMING ORGANIZATION NAME(S) AND ADDRESS(ES) Purdue University School of Nuclear Engineering 1290 Nuclear Engineering Building West Lafayette IN 47907-1290				8. PERFORMING ORGANIZATION REPORT NUMBER	
9. SPONSORING/MONITORING AGENCY NAME(S) AND ADDRESS(ES) Phillips Laboratory OL-AC PL/RKFE 9 Antares Road Edwards ABF CA 93524-7860				10. SPONSORING/MONITORING AGENCY REPORT NUMBER PL-TR-94-3037	
11. SUPPLEMENTARY NOTES COSATI CODE(S): 2013					
12a. DISTRIBUTION/AVAILABILITY STATEMENT Approved for Public Release; Distribution is Unlimited				12b. DISTRIBUTION CODE A	
13. ABSTRACT (MAXIMUM 200 WORDS) With a Dense Plasma Focus (DPF) device as the central concept, studies have been done to determine its feasibility as a propulsion system for space. In this report, past work in the areas of propulsion system code development is discussed, as well as the recent work dealing with stability analysis and scaling laws in the pinch region. A modeling based on a tokamak-like $m=0$ instability relating to the electron drift velocity wavelength is established. Magnetic field and kinetic temperature profiles are calculated based in certain assumptions about the plasma. It is found that the results of the pinch equilibrium profiles agree with the assumed current-squared scaling of kinetic temperature density, and that the total fusion power released from the pinch scales as: $P_f \sim I_p^{5.4}$. This is found to correlate well with the reaction rate parameter data for the utilized fuel of deuterium and helium-3. The resulting profile shape for kinetic temperature agrees in form with the proposed modeling. Using the more detailed pinch calculations in the already existent DPF propulsion code, it is found that for optimal performance a current range of 30 to 40 [MA] is needed to obtain results found in earlier work.					
14. SUBJECT TERMS fusion propulsion; dense plasma focus; magnetoplasma dynamic thruster; MPD thruster; advanced fuel (D- ³ He) fusion				15. NUMBER OF PAGES	
				16. PRICE CODE	
17. SECURITY CLASSIFICATION OF REPORT Unclassified	18. SECURITY CLASSIFICATION OF THIS PAGE Unclassified	19. SECURITY CLASSIFICATION OF ABSTRACT Unclassified	20. LIMITATION OF ABSTRACT SAR		

ABSTRACT

With a Dense Plasma Focus (DPF) device as the central concept, studies have been done to determine its feasibility as a propulsion system for space. In this report, past work in the areas of propulsion system code development is discussed, as well as the recent work dealing with stability analysis and scaling laws in the pinch region. A modeling based on a tokamak-like $m=0$ instability relating to the electron drift velocity wavelength is established. Magnetic field and kinetic temperature profiles are calculated based in certain assumptions about the plasma. It is found that the results of the pinch equilibrium profiles agree with the assumed current-squared scaling of kinetic temperature density, and that the total fusion power released from the pinch scales as: $P_f \sim I_p^{5.4}$. This is found to correlate well with the reaction rate parameter data for the utilized fuel of deuterium and helium-3. The resulting profile shape for kinetic temperature agrees in form with the proposed modeling. Using the more detailed pinch calculations in the already existent DPF propulsion code, it is found that for optimal performance a current range of 30 to 40 [MA] is needed to obtain results found in earlier work.

TABLE OF CONTENTS

Section	Page
INTRODUCTION	1
PRELIMINARY ANALYSIS AND REVIEW OF PREVIOUS WORKS	2
EQUILIBRIUM PROFILES AND STABILITY ANALYSIS	9
PINCH SCALING RELATIONS AND THEIR APPLICATION TO THE DPF PROPULSION SYSTEM	18
Review of Pinch Scaling Relations	18
DPF Propulsion System Application of Scaling Relations	28
CONCLUSION AND RECOMMENDATIONS	44
LIST OF REFERENCES	46
APPENDIX A	49
APPENDIX B	80

Accession For	
NTIS	<input checked="" type="checkbox"/>
CRA&I	<input type="checkbox"/>
DTIC	<input type="checkbox"/>
TAB	<input type="checkbox"/>
Unannounced	
Justification	
By	
Distribution /	
Availability Codes	
Dist	Avail and/or Special
A-1	

LIST OF FIGURES

Figure	Caption	Page
2.1	Mather vs. Filippov Plasma Foci Aspect Ratios [7]	4
3.1	Modeling of Plasma Pinch as One-Half Electron Drift Velocity $m=0$ Instability Wavelength	10
3.2	Hybrid Coordinate System for Purposes of Drift Instability Calculations	11
3.3	Streamline Map for Half of the Pinch Region for Radial vs. Axial Distances ...	15
3.4	Schematic of Diamagnetic Degradation of Azimuthal B Field [31]	16
4.1	Plasma Current Scaling of Pinch Length [30]	19
4.2	Plasma Current Scaling of Pinch Radius [30]	20
4.3	Deuterium Filling Pressure Scaling of Pinch Length [30]	21
4.4	Deuterium Filling Pressure Scaling of Pinch Radius [30]	22
4.5	Typical Test Axially Averaged Profiles of Ion Number Density n , Ion Kinetic Temperature kT , Ion Axial Velocity v_z , and Fusion Power Density	23
4.6	Computational Mesh Used in Pinch Calculations (20-by-20)	24
4.7	Typical Test Input Ion Number Density Profile	25
4.8	Typical Test Local Magnetic Field Profile	26
4.9	Typical Test Resultant Ion Kinetic Temperature Profile.....	27
4.10	Scaling of Fusion Power Output with Axial Current.....	29
4.11	Current-Squared Scaling of Plasma Energy (Kinetic Temperature) Density	29
4.12	Typical Mission-Required Axially Averaged Profiles of Ion Number Density n , Kinetic Temperature kT , Ion Axial Velocity v_z , and Fusion Power Density	32
4.13	Typical Mission-Required Input Ion Number Density Profile	33
4.14	Typical Mission-Required Local Magnetic Field Profile	34

4.15	Typical Mission-Required Resultant Kinetic Temperature Profile	35
4.16	Pinch Currents Associated with the 18 Test Case Combinations of Ion Number Density and Axial Velocity	36
4.17	Effect of Propellant Mass Flow Rate on Specific Impulse and Thrust-to- Weight Ratio in 18 Test Cases at 3 Different Rates for a Δv of 10 km/s Using a 4-Thruster System	38
4.18	Pinch Current, Specific Impulse, and F/W Ratio for Propellant Mass Flow Rate of 1 kg/s and $\Delta v = 10$ [km/s] with (a) 1 Thruster and (b) 2 Thrusters	39
4.19	Pinch Current, Specific Impulse, and F/W Ratio for Propellant Mass Flow Rate of 1 kg/s and $\Delta v = 10$ [km/s] with (b) 3 Thrusters and (b) 4 Thrusters	40
4.20	DPF Operating Energies vs. Thrust-to-Weight Ratios and Specific Impulse Values for Propellant Flow Rates of 10, 20, and 30 [kg/s] Using 4 Thrusters with a Mission Velocity Increment of 10 [km/s]	41
4.21	Effect on Performance Parameters for Various Scalings of Fusion Number Yield with Current ($Y_p \sim I^n$, with $n = 2,3,4,5$)	42
A.1	Pinch Current, Specific Impulse, and F/W Ratio for Propellant Mass Flow Rate of 1 kg/s and $\Delta v = 10$ [km/s] with (a) 1 Thruster and (b) 2 Thrusters	50
A.2	Pinch Current, Specific Impulse, and F/W Ratio for Propellant Mass Flow Rate of 1 kg/s and $\Delta v = 10$ [km/s] with (b) 3 Thrusters and (b) 4 Thrusters	51
A.3	Pinch Current, Specific Impulse, and F/W Ratio for Propellant Mass Flow Rate of 1 kg/s and $\Delta v = 20$ [km/s] with (a) 1 Thruster and (b) 2 Thrusters	52
A.4	Pinch Current, Specific Impulse, and F/W Ratio for Propellant Mass Flow Rate of 1 kg/s and $\Delta v = 20$ [km/s] with (b) 3 Thrusters and (b) 4 Thrusters	53
A.5	Pinch Current, Specific Impulse, and F/W Ratio for Propellant Mass Flow Rate of 1 kg/s and $\Delta v = 40$ [km/s] with (a) 1 Thruster and (b) 2 Thrusters	54
A.6	Pinch Current, Specific Impulse, and F/W Ratio for Propellant Mass Flow Rate of 1 kg/s and $\Delta v = 40$ [km/s] with (b) 3 Thrusters and (b) 4 Thrusters	55
A.7	Pinch Current, Specific Impulse, and F/W Ratio for Propellant Mass Flow Rate of 5 kg/s and $\Delta v = 10$ [km/s] with (a) 1 Thruster and (b) 2 Thrusters	56
A.8	Pinch Current, Specific Impulse, and F/W Ratio for Propellant Mass Flow Rate of 5 kg/s and $\Delta v = 10$ [km/s] with (b) 3 Thrusters and (b) 4 Thrusters	57
A.9	Pinch Current, Specific Impulse, and F/W Ratio for Propellant Mass Flow Rate of 5 kg/s and $\Delta v = 20$ [km/s] with (a) 1 Thruster and (b) 2 Thrusters	58
A.10	Pinch Current, Specific Impulse, and F/W Ratio for Propellant Mass Flow Rate of 5 kg/s and $\Delta v = 20$ [km/s] with (b) 3 Thrusters and (b) 4 Thrusters	59

A.11	Pinch Current, Specific Impulse, and F/W Ratio for Propellant Mass Flow Rate of 5 kg/s and $\Delta v = 40$ [km/s] with (a) 1 Thruster and (b) 2 Thrusters ...	60
A.12	Pinch Current, Specific Impulse, and F/W Ratio for Propellant Mass Flow Rate of 5 kg/s and $\Delta v = 40$ [km/s] with (b) 3 Thrusters and (b) 4 Thrusters ...	61
A.13	Pinch Current, Specific Impulse, and F/W Ratio for Propellant Mass Flow Rate of 10 kg/s and $\Delta v = 10$ [km/s] with (a) 1 Thruster and (b) 2 Thrusters ...	62
A.14	Pinch Current, Specific Impulse, and F/W Ratio for Propellant Mass Flow Rate of 10 kg/s and $\Delta v = 10$ [km/s] with (b) 3 Thrusters and (b) 4 Thrusters ...	63
A.15	Pinch Current, Specific Impulse, and F/W Ratio for Propellant Mass Flow Rate of 10 kg/s and $\Delta v = 20$ [km/s] with (a) 1 Thruster and (b) 2 Thrusters ...	64
A.16	Pinch Current, Specific Impulse, and F/W Ratio for Propellant Mass Flow Rate of 10 kg/s and $\Delta v = 20$ [km/s] with (b) 3 Thrusters and (b) 4 Thrusters ...	65
A.17	Pinch Current, Specific Impulse, and F/W Ratio for Propellant Mass Flow Rate of 10 kg/s and $\Delta v = 40$ [km/s] with (a) 1 Thruster and (b) 2 Thrusters ...	66
A.18	Pinch Current, Specific Impulse, and F/W Ratio for Propellant Mass Flow Rate of 10 kg/s and $\Delta v = 40$ [km/s] with (b) 3 Thrusters and (b) 4 Thrusters ...	67
A.19	Pinch Current, Specific Impulse, and F/W Ratio for Propellant Mass Flow Rate of 20 kg/s and $\Delta v = 10$ [km/s] with (a) 1 Thruster and (b) 2 Thrusters ...	68
A.20	Pinch Current, Specific Impulse, and F/W Ratio for Propellant Mass Flow Rate of 20 kg/s and $\Delta v = 10$ [km/s] with (b) 3 Thrusters and (b) 4 Thrusters ...	69
A.21	Pinch Current, Specific Impulse, and F/W Ratio for Propellant Mass Flow Rate of 20 kg/s and $\Delta v = 20$ [km/s] with (a) 1 Thruster and (b) 2 Thrusters ...	70
A.22	Pinch Current, Specific Impulse, and F/W Ratio for Propellant Mass Flow Rate of 20 kg/s and $\Delta v = 20$ [km/s] with (b) 3 Thrusters and (b) 4 Thrusters ...	71
A.23	Pinch Current, Specific Impulse, and F/W Ratio for Propellant Mass Flow Rate of 20 kg/s and $\Delta v = 40$ [km/s] with (a) 1 Thruster and (b) 2 Thrusters ...	72
A.24	Pinch Current, Specific Impulse, and F/W Ratio for Propellant Mass Flow Rate of 20 kg/s and $\Delta v = 40$ [km/s] with (b) 3 Thrusters and (b) 4 Thrusters ...	73
A.25	Pinch Current, Specific Impulse, and F/W Ratio for Propellant Mass Flow Rate of 30 kg/s and $\Delta v = 10$ [km/s] with (a) 1 Thruster and (b) 2 Thrusters ...	74
A.26	Pinch Current, Specific Impulse, and F/W Ratio for Propellant Mass Flow Rate of 30 kg/s and $\Delta v = 10$ [km/s] with (b) 3 Thrusters and (b) 4 Thrusters ...	75
A.27	Pinch Current, Specific Impulse, and F/W Ratio for Propellant Mass Flow Rate of 30 kg/s and $\Delta v = 20$ [km/s] with (a) 1 Thruster and (b) 2 Thrusters ...	76
A.28	Pinch Current, Specific Impulse, and F/W Ratio for Propellant Mass Flow Rate of 30 kg/s and $\Delta v = 20$ [km/s] with (b) 3 Thrusters and (b) 4 Thrusters ...	77

- A.29 Pinch Current, Specific Impulse, and F/W Ratio for Propellant Mass Flow
Rate of 30 kg/s and $\Delta v = 40$ [km/s] with (a) 1 Thruster and (b) 2 Thrusters ...78
- A.30 Pinch Current, Specific Impulse, and F/W Ratio for Propellant Mass Flow
Rate of 30 kg/s and $\Delta v = 40$ [km/s] with (b) 3 Thrusters and (b) 4 Thrusters .79

LIST OF TABLES

Table	Caption	Page
I	Researchers with Theoretical Neutron Yield Scaling Proposed	5
II	Researchers with Device Parameters and Experimentally-Determined Neutron Yield Scaling Relations (NS=None Stated)	7
III	Comparison of Plasma Pinch Length h in Various Mather-type DPF Experiments Using Empirical Scaling Relation (Eq.(3.1)) [30]	8
IV	Comparison of Performance Parameters for Livermore-I DPF, Enhanced Electrode Design DPF, and Detailed Pinch DPF Propulsion System Test Cases	31

INTRODUCTION

In this third, final report of the three-year project, primary work is centered on the equilibrium and stability analyses of pinch plasmas and the scalings of dense plasma focus (DPF) properties with respect to various parameters. The primary properties of interest in the pinch scalings are the plasma pinch length and radius and the fusion product yield. A model based on a tokamak-like $m=0$ sausage instability relating to the electron drift velocity wavelength was developed as described in the later section. Regarding the length and radius of the pinch region, the parameters of interest have been the average ion current, the plasma kinetic temperature within the pinch, and the plasma number densities within the pinch. For the fusion product yield, it has been investigated how it varies with the ion current flowing in the pinch region of the plasma focus structure.

For the properties of pinch length and radius, a model was developed based on the electron drift velocity. At its heart is the coupling of the wave number of the electron drift velocity and the wave number associated with the ion gyromagnetic drift (the Larmor radii). A variant form of the traditional cylindrical coordinate system used with the DPF has been developed to illustrate how this model is to be applied.

With regard to the fusion product yield, a two-dimensional grid was used to divide the pinch region into divisions along the traditional r and z coordinates. Assuming an axial velocity profile and an initial number density profile along these axes, as well as a parabolic contour for the edge of the pinch region, the ion kinetic temperature profiles were found. This was done based on the magnetic field penetrating to the centerline of the pinch before going to zero. It was assumed that the total pressure from the sum of the magnetic field pressure and the plasma particle pressure remained constant throughout the region of the pinch. After determining the kinetic temperature profiles, the fusion product yield is found based on the reaction rate parameter data and the calculated volume of the pinch region. This may be correlated with the calculated current within the pinch region in order to determine the scaling of the fusion product yield with varying pinch current.

Use was made of the codes developed earlier in project history [1,2] in order to determine the effects of the recent work on propulsion performance parameters for various mission specifications. The effects on mission parameters such as velocity increment (Δv), propellant mass flow rate, number of thrusters used, thrust-to-weight (F/W) ratio, and specific impulse (I_{sp}) have been investigated.

PRELIMINARY ANALYSIS AND REVIEW OF PREVIOUS WORKS

The dense plasma focus (DPF) is one of a class of magnetically-confined fusion (MCF) devices known as Z-pinches. One-dimensional (1-D) Z-pinch devices are characterized by a "straightened" toroidal geometry with a purely poloidal magnetic field. They possess a toroidal geometry from the standpoint that the plasma behavior is quite similar to that which would be expected in a single, extracted section of a torus device. Using cylindrical coordinates, as shall be the system of choice throughout this report, only the B_θ component of the magnetic field \mathbf{B} will be considered to be non-zero. It is induced by a longitudinal current I_z flowing in the plasma. When the plasma current vanishes, no background \mathbf{B} field remains. The following arguments show the derivation of the radial pressure balance in a 1-D Z-pinch [3].

Assuming azimuthal symmetry of \mathbf{B} , the equation:

$$\nabla \cdot \mathbf{B} = 0 \quad (2.1)$$

appears as:

$$\frac{1}{r} \frac{\partial B_\theta}{\partial \theta} = 0 \quad (2.2)$$

Applying Ampere's Law shows that $J_z(r)$ is the only non-zero component of the current density:

$$J_z = \mu_0^{-1} \frac{1}{r} \frac{d}{dr} (r B_\theta) \quad (2.3)$$

Also, only the radial component of the momentum equation is nontrivial:

$$J_z B_\theta = -\frac{dp}{dr} \quad (2.4)$$

If Eq. (2.3) is substituted into Eq. (2.4):

$$\frac{dp}{dr} + \frac{B_\theta}{\mu_0 r} \frac{d}{dr} (r B_\theta) = 0 \quad (2.5)$$

which may also be written in the form:

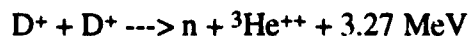
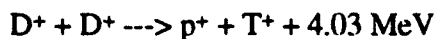
$$\frac{d}{dr} \left(p + \frac{B_{\theta}^2}{2\mu_0} \right) + \frac{B_{\theta}^2}{\mu_0 r} = 0 \quad (2.6)$$

Eq. (2.6) is the basic radial pressure-balance relation for a 1-D Z-pinch. The two terms within the parentheses represent the particle pressure and the magnetic pressure, respectively. The final term represents the tension force generated by the \mathbf{B} field line curvature. This tension force is of utmost importance in a Z-pinch device, as its presence provides the radial confinement of the plasma. Later, the DPF will be studied from a two-dimensional standpoint in the r and z coordinates, moving from the 1-D argument in r presented above. Azimuthal symmetry will continue to be assumed to account for the θ component.

The Dense Plasma Focus (DPF) was first engineered in separate endeavors by Filippov [4] in 1962 and Mather [5] in 1964. Most of the DPF experimental devices fall into one of two primary geometries, accompanied by the corresponding name of one of these two initial researchers. The Mather-type plasma focus device uses axial injection and radial compression of the plasma to form the pinch, employing an electrode geometry having an aspect ratio $a < 1$, while the Filippov device is characterized by $a > 1$. The aspect ratio is defined as the ratio of cathode diameter to anode length. A schematic comparison is shown in Figure 2.1. The DPF combines aspects of two other Z-pinch designs: the compressional Z-pinch and the gas-embedded (imploding liner) Z-pinch. It forms in much the same manner as the compressional pinch, but has higher plasma densities on the order of those found in the gas-embedded pinch [6]. More than 40 laboratories in Europe, the United States, Russia, India, and Japan, among other nations, currently perform DPF experimental and theoretical research [7].

Of utmost interest to the success of a DPF device as a power source and a propulsion device is the production of energetic particles from the thermonuclear processes which occur in the pinch region of the compressed plasma. Most experimental work done to date has used a fusion fuel mixture of deuterium. Deuterium has the advantages of being both plentiful (and therefore inexpensive) and non-radioactive, as opposed to the usage of tritium in conjunction with deuterium.

The deuteron (D) - deuteron (D) reaction occurs through two primary pathways:



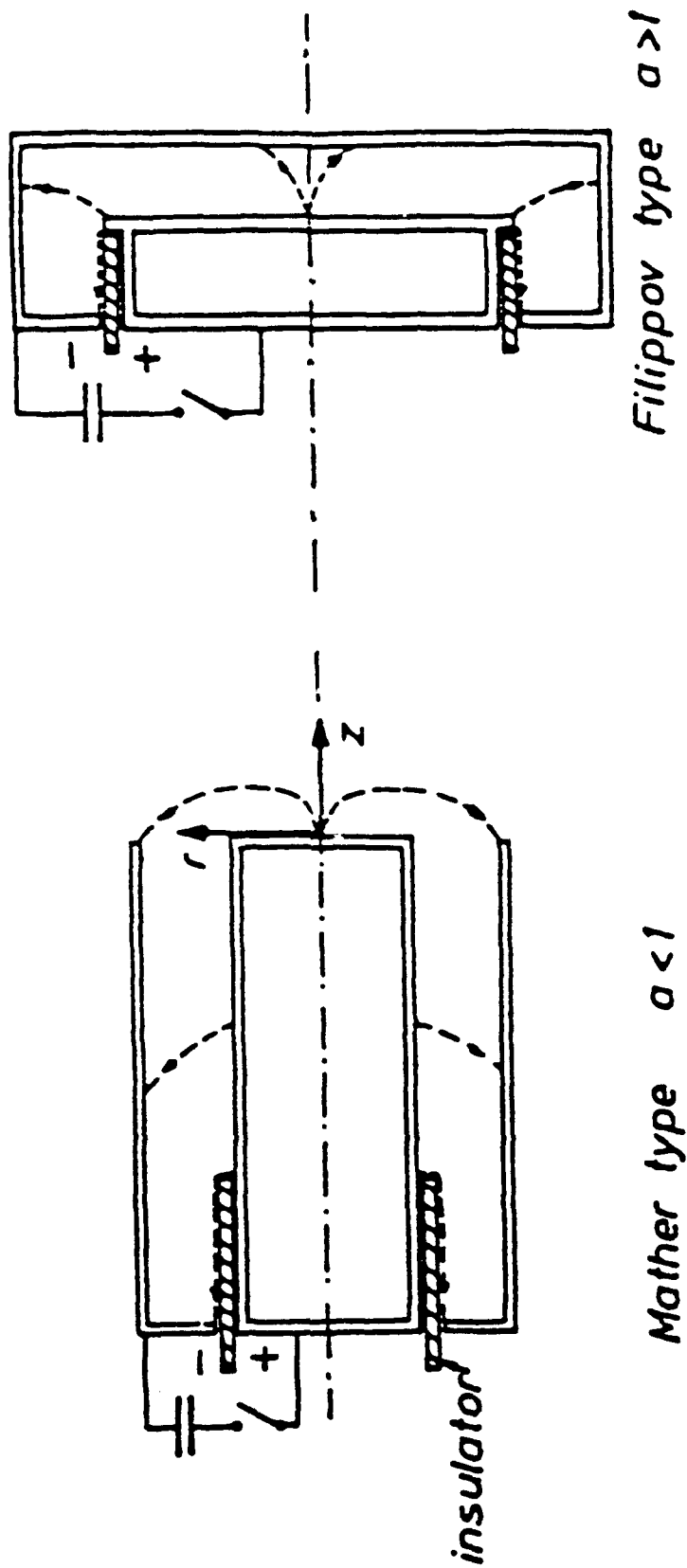


Figure 2.1
Mather vs. Filippov Plasma Foci Aspect Ratios [7]

Because the DPF has long been used as a laboratory neutron source, one of the primary goals of research has been to maximize neutron yield. This necessarily indicates a large thermonuclear reaction rate. In working to maximize neutron production, it was necessary to determine which parameters of DPF operation affected the neutron yield and to what degree. One of the key parameters in this work has been the current within the plasma pinch. Much has been done from both a theoretical and an experimental standpoint to determine the degree of effect these currents have on the neutron yield.

Some of the first theoretical scaling work was done by Kaeppeler in 1974 and 1976 [8,9], who determined that the neutron yield Y_n should scale with the pinch plasma current as I_p^4 . Decker deduced in 1977 [10] a scaling relation of $Y_n \sim I_{max}^b$, with I_{max} being the maximum main bank capacitor discharge current and the exponent b varying between 3.5 and 4.6. Table I lists a summary of the theoretical work found in the literature.

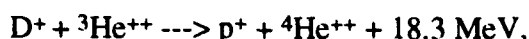
Table I
Researchers with Theoretical Neutron Yield Scaling Proposed

<u>Researcher/Year</u>	<u>Location/Device</u>	<u>Y_n</u>
Kaeppeler/1974[8]	Stuttgart	I_p^4
Rapp/1974[12]	Stuttgart/Nessi	I_p^4
Decker/1977[11]	Stuttgart	$I_{max}^{3.5 \text{ to } 4.6}$

Moving to the experimental front, in 1978 Shyam and Srinivasan found using a 100-Joule DPF that Y_n scaled with $W^{1.73}$ and $I^{4.29}$ [13], where W is the capacitor bank energy and I is the discharge current of the bank. Mather found $Y_n \sim I^4$ in 1971 [14] and Bernard found $Y_n \sim I^{3.3}$ in 1976 [15,16], based on their experimental findings. In more recent years, scaling law development has focused on the use of the plasma current I_p in scaling relations, rather than the discharge current I . This is due to the fact that the current flowing within the pinch is directly characteristic of the pinched region, where the fusion reactions occur, and should, therefore, be closely interwoven with the mechanisms involved with fusion particle production in the pinch. Scaling with the discharge current fails to account for the current loss during the rundown phase of the plasma sheath which forms the pinch. Recognizing that the presence of such current losses leaves a degree of uncertainty in the number of particles trapped in the pinch and that improvements in measuring pinch plasma currents in recent years have taken place, the scaling laws have surely been directed away from using the discharge current as a key parameter when considering fusion yield. Experiments have shown $Y_n \sim I_p^{4.1}$ for the Minifokus device at Stuttgart in 1977 [17] and Conrads has found $Y_n \sim I_p^{3.3}$ based on agreement of the SPEED II device at the Institut für Plasmaphysik in Germany with worldwide research in recent years [6]. Stygar, *et al.* determined a

scaling of $I_p^{4.4}$ in 1982 [18]. A summary of these experimentally determined scalings are presented in Table II, along with some device characteristics of those used by the researchers indicated below.

Of other recent interest has been the study of using the combination of the fusion fuels, deuterium and helium-3 [1,2,23-27], as opposed to the traditional D-D combination used in experimental facilities and the radioactive D-T combination used in tokamak facilities in the recent past. The advantages of such a fuel combination are illustrated by observing the fusion products produced in the reaction:



where the products are evidently only charged particles. Such reaction products have the advantage of being directed using a magnetic nozzle, a characteristic which lends itself for use in a propulsion system, where uni-directional thrust is desirable. Also, looking to future technological operations, the presence of charged ions makes such a fuel combination attractive for use in a direct conversion scheme to produce electricity [28]. The possible D-D background fusion reactions are considered to be suppressible by polarizing the spin of the interacting deuterons [29].

Turning to the scaling of the pinch size (radius and length) itself, some of the most current work has been done by Gerdin, *et al.* using a device at the University of Illinois [30]. During the late 1980's they measured the pinch current I_p and filling pressure p_0 in order to determine their scaling relation with the plasma pinch length h , in keeping with the original notation. The results of the pressure scaling measurements are included for the sake of completeness, but the investigation of the pressure dependence is not a primary focus of this report. Resulting from the work of Gerdin, *et al.* is the relation:

$$h \sim I_p^x p_0^y, \quad (2.7)$$

where $x = -0.02 \pm 0.12$ and $y = 0.26 \pm 0.13$. The dependence of the plasma radius r_0 was found to relate as:

$$r_0 \sim I_p^a p_0^b, \quad (2.8)$$

where $a = -0.18 \pm 0.11$ and $b = 0.2 \pm 0.03$. The graphs showing plasma length and radius versus the plasma current will be reproduced in a later section on the pinch scaling relations. Also present in Ref. [30] is a comparison of other devices where the value of h has been predicted using the

scaling law presented in Eq. (3.1). The pertinent device locations studied, along with the results, are found in Table III.

Table II
Researchers with Device Parameters and Experimentally-Determined
Neutron Yield Scaling Relations (NS=None Stated)

Researcher(s) Author(s)	Device (Location)	W (kJ)	P ₀ (torr)	r _A (cm)	r _C (cm)	r _p (cm)	cm	Y _n ~
Bernard[15,16]	(Limeil) Focus 1 Focus 2 Focus 3 Focus 4 Focus 5 Focus 6	15 16 30 32 32 48						I ^{3.3}
Decker[11] (Conrads[6])	SPEED II (Stuttgart)	1000	0.1-10					I _p ^{3.3}
Decker[19,20]	Nessi (Stuttgart)	30-60						I ⁴
Decker[11]	HV-Focus	12	8	1.20	3.0			NS
Herold[21]	Poseidon (Stuttgart)	280-500	4-6	6.55- 10.4	13.3- 14.6			I _{max} ^{3.3}
	PF-360 (Stuttgart)	200	12	5.0- 6.0	7.5- 11.25			I _{max} ^{3.2}
Mather[14]								I ⁴
Schmidt[7]	Various							I ^{3.3} I _p ⁴
Shyam/ Srinivasan[22]	TPF-1 (Bombay)	0.41- 2.15				0.2- 0.26	0.8- 1.8	NS
Shyam/ Srinivasan[13]	TPF-1 (Bombay)	0.1	0.1-10	1.1	3.6			I ^{4.29}
Stygar[18]	(Illinois)	6-12.5	3					I ^{4.4±0.3} (Peak Y) I ^{4.6±0.3} I ^{4.6} (hot target) I ^{5.2} (cold target)
Oppenländer [17]	Minifokus (Stuttgart)	12	1.9	2.5	4.5			I _p ^{4.1}

Table III
Comparison of Plasma Pinch Length h in Various Mather-type DPF Experiments
Using Empirical Scaling Relation (Eq.(3.1)) [30]

<u>Location and/or Device</u>	<u>r_A (cm)</u>	<u>I_p (kA)</u>	<u>p_0 (torr)</u>	<u>r_0 (cm)</u>	<u>Exper. h (cm)</u>	<u>Eq.(3.1) h (cm)</u>
U. of Illinois	2.5	550	3.0	0.15	1.3	1.3
Stuttgart Nessi	3.3	290	1.5	0.15	2	1.3
Swierk	5.0	1000	1.5	0.38	2 - 2.5	3.3
Darmstadt	0.8	200	2.6	0.04	0.25	0.35
Stevens Inst. Tech.	1.7	400-500	8	0.2	1.0 - 1.5	1.7

EQUILIBRIUM PROFILES AND STABILITY ANALYSIS

By studying the equilibrium profiles of the pinch properties, one can determine the effects of pinch current, pinch radius, pinch length and other parameters on such properties. Determination of the relations between such properties as pressure, plasma temperature, and local magnetic field strength with pinch radius and length allows one to see how such properties can be motivated to produce a pinch which yields the maximum thermonuclear yield of particles and energy.

As an attempt at relating the pinch radius and length to another property, one may consider modeling the pinch length as one-half of the wavelength of the $m = 0$ instability which forms the pinch. This is illustrated in Figure 3.1. The $m = 0$ instability presents a bridge of similarity to a tokamak device, where disruptions can occur along the toroidal plasma due to the uneven magnetic field profile. Now, to assess the feasibility of the aforementioned model, equilibrium profiles need to be assumed. If such profiles are assumed to behave in a similar manner to those of a tokamak device, which is also a device of toroidal geometry exhibiting $m = 0$ instabilities, then the following relations are plausible:

$$\frac{n(r)}{n_0} = \frac{kT_e(r)}{kT_{e,0}} = \frac{kT_i(r)}{kT_{i,0}} = 1 - 0.9 \frac{r^2}{r_{\max}^2} , \quad (3.1)$$

where n is the number density, kT is the kinetic temperature of the plasma, and r is the radius of the pinch, with r_{\max} being the maximum pinch radius. For this calculation, the coordinate system shown in Figure 3.2 is used. In order to have the same arrangement of magnetic field as in a tokamak, the DPF region is viewed as a cross section of the tokamak torus. The traditional r -axis of the pinch is relabeled the z -axis, which is shown coming out of the page. The magnetic field also is coming out of the page at the upper edge of the pinch region. The traditional direction of the θ -axis has been rotated 90 degrees, as shown in Figure 3.2, which the r -axis used in Figure 3.2 represents the distance from the center of the pinch to any given point within or at the edge of the pinch. The curves extending behind and to the left of the pinch represent the tokamak torus which is used as the basis for coupling the drift instability to the DPF pinch. It is further assumed that r_{\max} is constant for a given z in the new coordinate system, although in reality it would be a function of θ in the new coordinate system.

Now, since particle pressure is given by $p = nkT$, the electron pressure is given by:

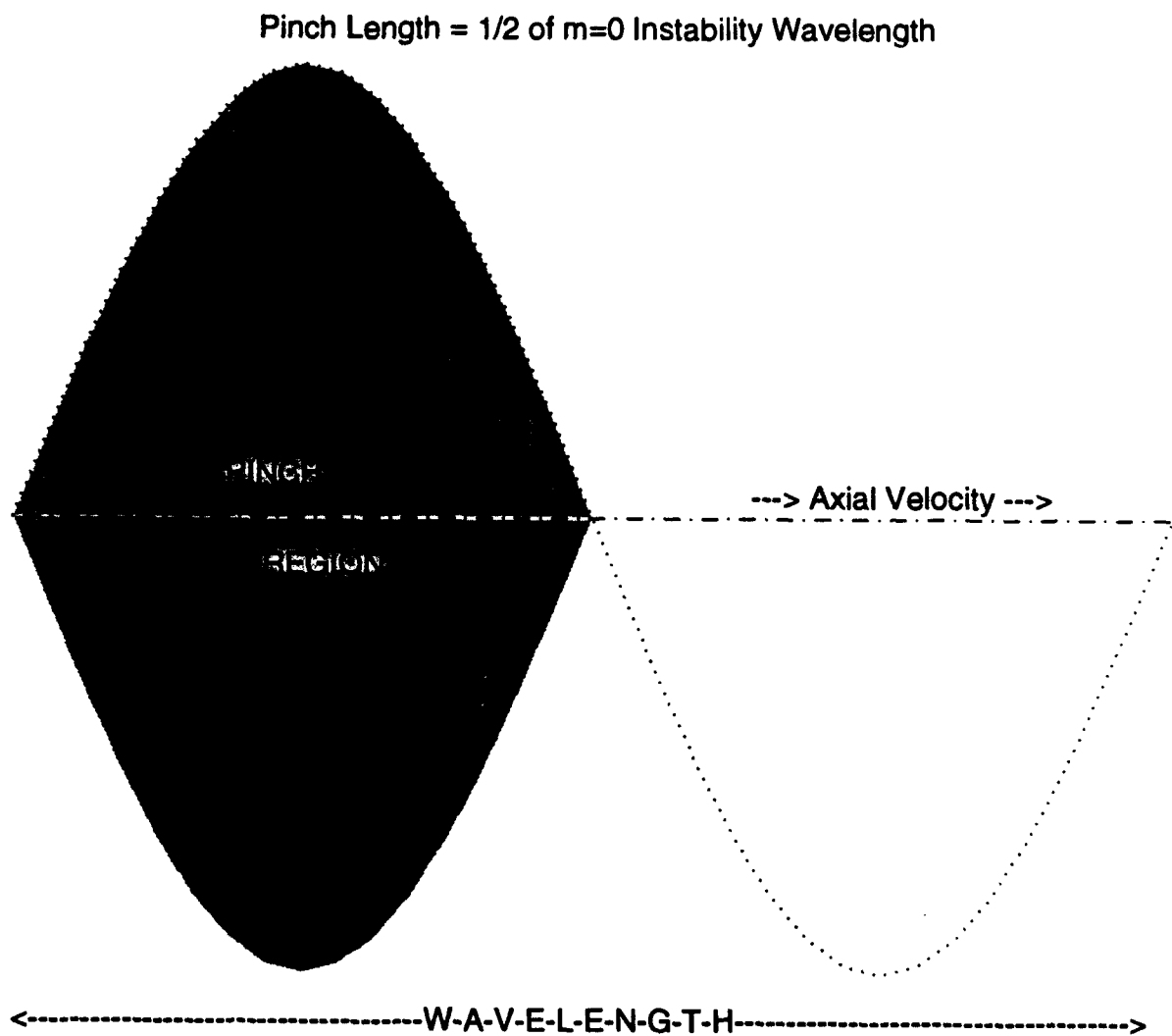


Figure 3.1
Modeling of Plasma Pinch as One-Half Electron Drift Velocity $m=0$ Instability Wavelength

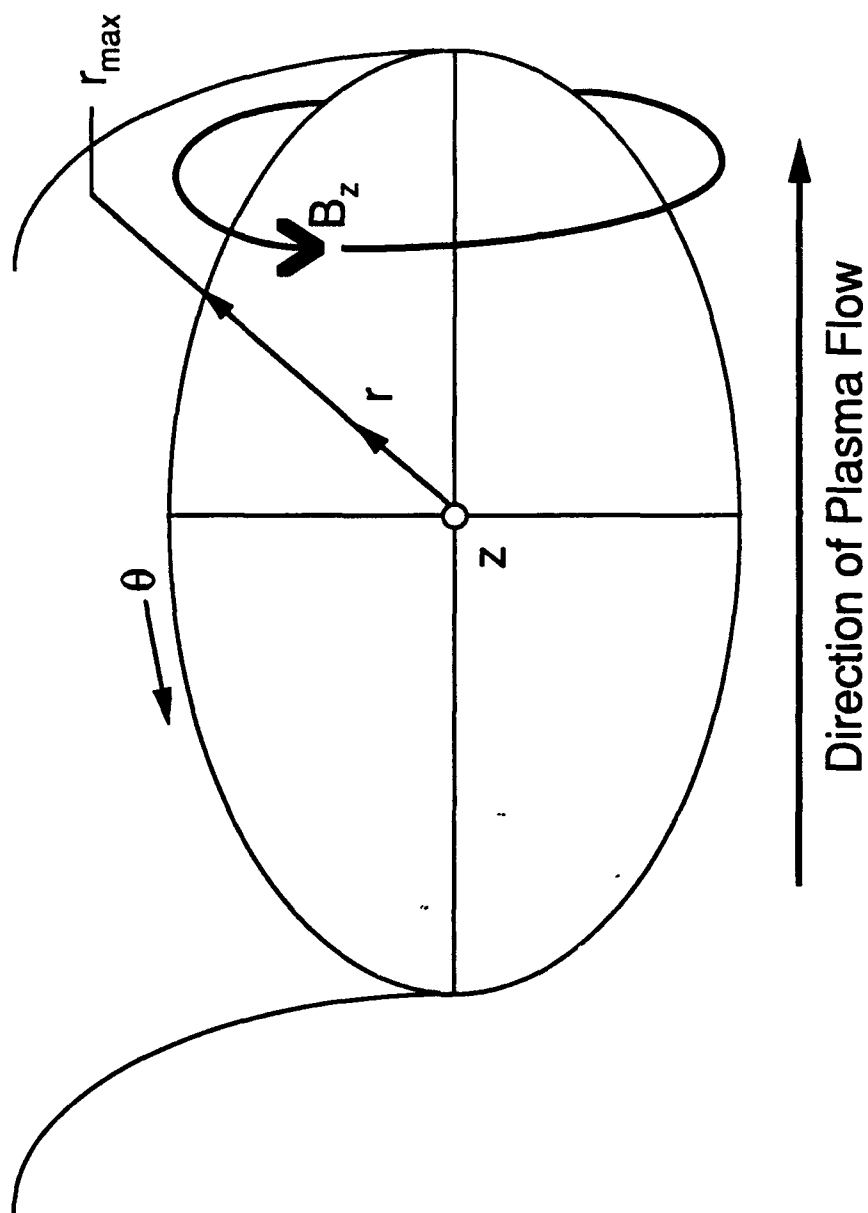


Figure 3.2
Hybrid Coordinate System for Purposes of Drift Instability Calculations

$$p_e = nkT_e = n_{oe}kT_{oe} \left(1 - 0.9 \frac{r^2}{r_{max}^2} \right)^2 . \quad (3.2)$$

According to Dolan [31], the electron drift velocity v_{de} is given by:

$$v_{de} = - \left(\frac{\partial p_e / \partial r}{n_e e B_z} \right) \Big|_{r=r_{max}} , \quad (3.3)$$

in terms of the present hybrid coordinate system. The wave number associated with this drift velocity matching the wave number associated with the ion cyclotron frequency is given by:

$$k_\theta = \frac{\omega_{ci}}{v_{de}} = \frac{2\pi}{\lambda_e} , \quad (3.4)$$

where ω_{ci} is the cyclotron frequency and λ_e is the wavelength of the drift wave. Combining Eqs. (3.2-3.4) yields the expression for λ_e , using $\omega_{ci} = eB/m_i$:

$$\lambda_e = \frac{7.2\pi m_i k T_{oe}}{e^2 r_{max} B_z^2} . \quad (3.5)$$

Next, it is assumed that the sum of the particle kinetic pressure and the confining magnetic pressure is constant:

$$p + \frac{B_z^2}{2\mu_o} \approx \text{const} = \frac{B_{ov}^2}{2\mu_o} , \quad (3.6)$$

where μ_o is the permeability of free space, $4\pi \cdot 10^{-7}$ [H/m], and B_{ov} is the value of the magnetic field at the vacuum boundary. Now, Eq. (3.6) is solved for B_z^2 and coupled with Eq. (3.5), yielding:

$$\lambda_e = \frac{2.93 \cdot 10^{19}}{r_{max} n_{oe}} , \quad (3.7)$$

where the m_i value used is the mass of a deuteron in order to compare with experimental devices, which use deuteron-deuteron fusion fuel mixtures. Since the length of the pinch (l_p) is equal to one half of λ_e , and assuming values of $l_p = 0.013$ [m] and $r_{max} = 0.0015$ [m] [30], the value of n_{oe}

is found to be $7.54 \cdot 10^{23} \text{ [m}^{-3}\text{]}$. This is $\sim 10^{24} \text{ [m}^{-3}\text{]}$, which is on the order of those number densities found in Z-pinchs by Choi of $2 \cdot 10^{24} \text{ [m}^{-3}\text{]}$ and in dense plasma foci by Herold, *et al.* of $3 \cdot 10^{24} \text{ [m}^{-3}\text{]}$ [7]. Increases of one to two orders of magnitude in number density will be required for space propulsion applications, as will be made evident by observing the values of parameters in test cases shown later. It is generally accepted, however, that present devices can readily attain ion number densities of $10^{25} \text{ [m}^{-3}\text{]}$.

Building on this novel approach to pinch dimensions, attention is turned to the range of influence of the magnetized plasma in the pinch. The drift is found to proceed along the approximately elliptical pinch boundaries in a rough, counter-clockwise motion. This drift motion, in turn, induces a magnetic field which opposes the applied B_θ field. This is known as the diamagnetic effect. The diamagnetism decreases the magnetic field as r approaches the central pinch axis. The qualitative significance of this will be illustrated later. To see the degree of effect diamagnetism has in the DPF, the Larmor radius of the deuterons in the plasma is calculated, as well as the skin depth. The Larmor radius (r_L) is given by:

$$r_L^i = \frac{\sqrt{2m_i k T_i}}{ZeB} , \quad (3.8)$$

where 'i' denotes the form for ions. Here, the mass m_i is the average mass of a deuteron and a helium-3 ion, while kT_i is the kinetic temperature, or energy, of both ion species. A plasma of these two components requires an ignition temperature of $\sim 30 \text{ [keV]}$, so this value is chosen for the calculation [24,25]. For a deuteron the atomic number $Z = 1$, while $Z = 2$ for a helium-3 ion, so $Z = 1.5$ is used. The electronic charge e is $1.602 \cdot 10^{-19} \text{ [C]}$. To determine the value of B needed, a balance of the magnetic compressional pressure and the particle inertial pressure is assumed, i. e., the commonly referred to " $\beta = 1$ " condition, where:

$$\beta = \frac{p_{\text{part}}}{p_{\text{mag}}} = \frac{\sum_s n_s k T_s}{\left(\frac{B^2}{2\mu_0} \right)} , \quad (3.9)$$

and the summation is over the s many species of ions plus the electrons as another species, with p_{part} representing the particle pressure and p_{mag} representing the confining magnetic pressure. Using the number density $n = 7.54 \cdot 10^{23} \text{ [m}^{-3}\text{]}$ found using Eq. (3.7), the value of B is determined and substituted above to yield a Larmor radius of $3.71 \cdot 10^{-4} \text{ [m]}$. This is \sim one fourth of the assumed pinch radius of 0.0015 [m] .

From a qualitative standpoint, then, the diamagnetic effect is quite dominant, as the Larmor radii of the pinch-edge deuterons show that they gyrate into the pinch considerably. Away from the pinch center, toward the ends of the pinch, the effect is more noticeable because the Larmor radii comprise a larger radial fraction of the pinch volume.

In developing a two-dimensional code, a traditional cylindrical coordinate system was chosen, for the pinch exhibits approximately cylindrical shape. For the shape chosen to model the pinch with, the only digression from a cylindrical shape is the narrowing of the pinch at the axial ends of the pinch region, thus resulting in the parabolic contour at the pinch edge. For one half of the pinch, examples of the assumed "streamlines" of particles flowing in the pinch are shown in Figure 3.3. The streamlines should be considered as computational grid tools *only*, for they are used to represent the general velocity of a group of particles around a particular grid point. The "streamlines" do *not*, then, necessarily represent the *actual* paths of particles through the pinch, as the pinch is assumed to be in equilibrium. In this case it is assumed that no particles leave the pinch, save those that are products of thermonuclear fusion within the pinch. To determine the equilibrium profiles using the numerical grid computation, it is necessary to use the correct value of the azimuthal magnetic field induced by the plasma current at each axial division of the pinch region.

Here is where the results of diamagnetism come into play. It is of key importance to understand to what degree the azimuthal magnetic field is assumed nullified by the diamagnetic field induced by the magnetic current flowing in the pinch. If its effect is near-complete dominance within a skin layer at the edge, then the magnetic field within the pinch volume is considered to be near zero. For the computations used to produce the results in this report, the azimuthal magnetic field is assumed to fall off in linear fashion, reaching zero at the pinch axis. An illustration of this magnetic field degradation is shown in Figure 3.4, where the B_θ term is being driven to zero by the diamagnetic current in the plasma. Where the illustration shows the field to degrade sharply at first, then more gradually approaching the zero value, the assumption here is that the degradation exhibits a straight-line behavior. A 20 by 20 grid was used for the pinch region model.

Fusion power density calculations were done using the averaged values of ion number densities and using a reaction rate parameter value based on the average kinetic temperature within the pinch. The fusion power density is given by:

$$PD_{\text{fusion}} = n_1 n_2 \langle \sigma v \rangle E_{12} , \quad (3.10)$$

where n_1 and n_2 are the number densities of the two reactant species, $\langle \sigma v \rangle$ is a term known as the reaction rate parameter, or average product of the thermonuclear cross section σ and the relative speed v between species 1 and 2, and E_{12} is the energy yield per thermonuclear reaction of one pair

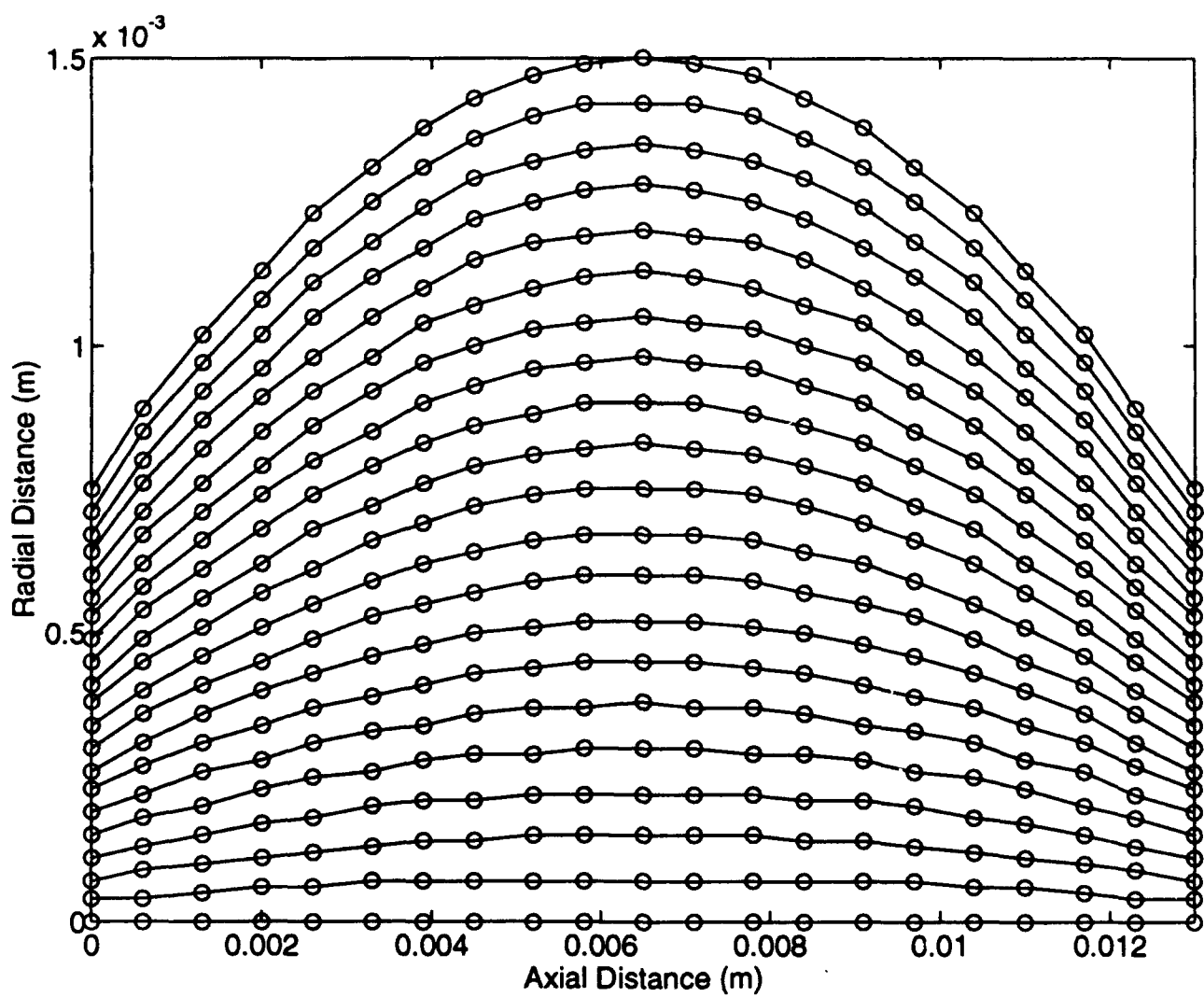


Figure 3.3
Streamline Map for Half of the Pinch Region for Radial vs. Axial Distances

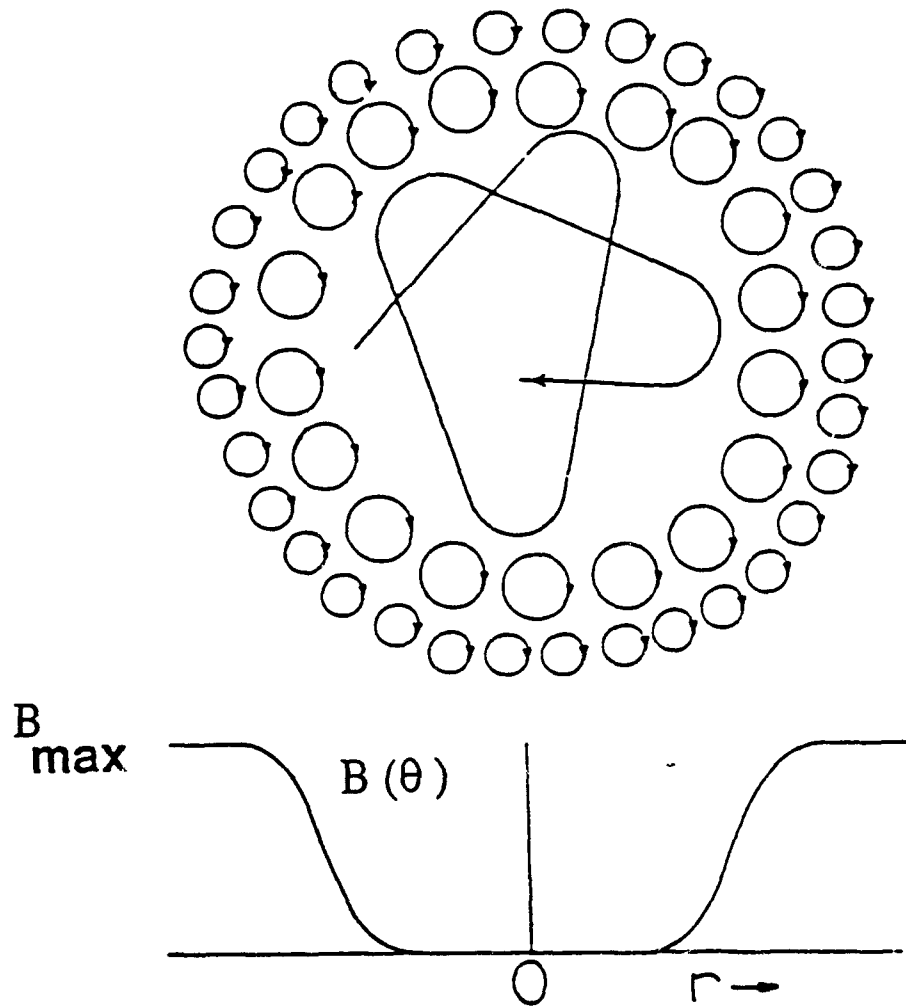


Figure 3.4
Schematic of Diamagnetic Degradation of Azimuthal B Field [31]

of reactant species. Values of the reaction rate parameter are well-documented in various texts [25], as are the energy yields per reaction, obtained through a simple conservation of mass/energy calculation for the appropriate thermonuclear reaction. The energy yields for the D-D and D-³He reactions are 3.65 [MeV] and 18.3 [MeV], respectively, where the value for D-D is the average energy yield of the two major reaction pathways, which have approximately equal occurrence probabilities. Since $\langle\sigma v\rangle$ is a function of the energy kT of the pinch particles, the profiles of n and kT obtained in the next section on pinch scaling relations can be used with available $\langle\sigma v\rangle$ data and Eq. (3.10) to yield the fusion energy density output of the pinch

Assuming the pinch to have a circular cross section, which follows from assuming azimuthal symmetry, the volume of the pinch is equivalent to $V = \pi(r_{av}^2)(l_{pinch})$. Thus, a typical pinch volume would be: $1.50 \cdot 10^{-7}$ [m³]. If a D-³He fuel mixture is considered, with $n_D = n_{He-3} = 0.5n$, then Eq. (3.10) becomes:

$$PD_f = \frac{1}{4} \langle n \rangle^2 \langle (\sigma v)_{D^3He} \rangle E_{D^3He} + \frac{1}{8} \langle n \rangle^2 \langle (\sigma v)_{DD} \rangle E_{DD} , \quad (3.11)$$

where the second set of averaging signs surrounding each $\langle\sigma v\rangle$ and each n value indicates an average over the pinch region, both radially and axially. Such averages are computed during the execution of the numerical computation, just as the $\langle r \rangle$ value discussed above is computed. For energies in the range of ~ 1 to 100 [keV], the $\langle\sigma v\rangle$ values are given by the log base-10 curve fits found in [25]. The kT values used in the equations found there are input in units of [keV], while the resulting values of $\langle\sigma v\rangle$ are in units of [cm³/s]. Keeping with the MKS system used in this report, the $\langle\sigma v\rangle$ values are multiplied by a factor of 10^{-6} to obtain units of [m³/s]. The fusion power output is computed by multiplying the fusion power density by the volume of the pinch. From this, a graphical representation can be made of the fusion power versus pinch current to determine a scaling relation.

PINCH SCALING RELATIONS AND THEIR APPLICATION TO THE DPF PROPULSION SYSTEM

Review of Pinch Scaling Relations

Experiments at the University of Illinois have investigated the scaling of pinch dimensions in a dense plasma focus (DPF) device [30]. For a deuterium filling pressure of 3.0 [torr], the current in the plasma was found to have little, if any, effect on the pinch length (Figure 4.1). However, with regard to the radius of the pinch, a small dependence was observed (Figure 4.2). Concerning the scaling of the pinch radius and length with the filling pressure, the length scaling was not obvious due to the large spread in data (Figure 4.3), while the radius scaling was quite well-behaved (Figure 4.4), as compared to the three afore-mentioned scaling plots. For each of the four observed relationships, the power fit law is stated on the appropriate figure from Figures 4.1-4.4. In each case the exponent value is considerably less than unity; perhaps even exhibiting zero dependence on the property in question. These experimental results show the most recent work found regarding experimentally determined pinch size scaling studies of the DPF.

In the research described in this report, differing values of pinch radius and length were specified to obtain the temperature and number density profiles, and currents associated with each set of values. It was also possible to change the given values of maximum number density and drift velocity in order to obtain how the fusion power output scaled with the plasma current. The number density profile for tokamak-like plasmas was assumed in the radial direction of the pinch, with the maximum value of number density occurring at the center of the pinch, while along the axial direction of the pinch, a modified form of the tokamak profile exhibiting a lesser gradient was used in order to agree with the axial profiles given by Potter [32].

For comparison, use was made of work done by Potter [32] in order to see how the average ion number density (n), average ion kinetic temperature (kT), average fusion power density, and average axial velocity (v_z) vary over the length of the pinch region, per Figure 4.5 showing typical results from the present work. Using a two-dimensional 20-by-20 mesh (Figure 4.6) and the plasma ion axial current based on the given ion number density profile (Figure 4.7) and the axial velocity, the local magnetic field profile (Figure 4.8) and the kinetic temperature profile (Figure 4.9) were determined. The B profile follows the earlier conservation relation set forth in Eq. (3.6). From the appearance of the kT profile, it can be seen that the radial profile has the same general behavior of the n profile which was assumed to be tokamak-like. The only

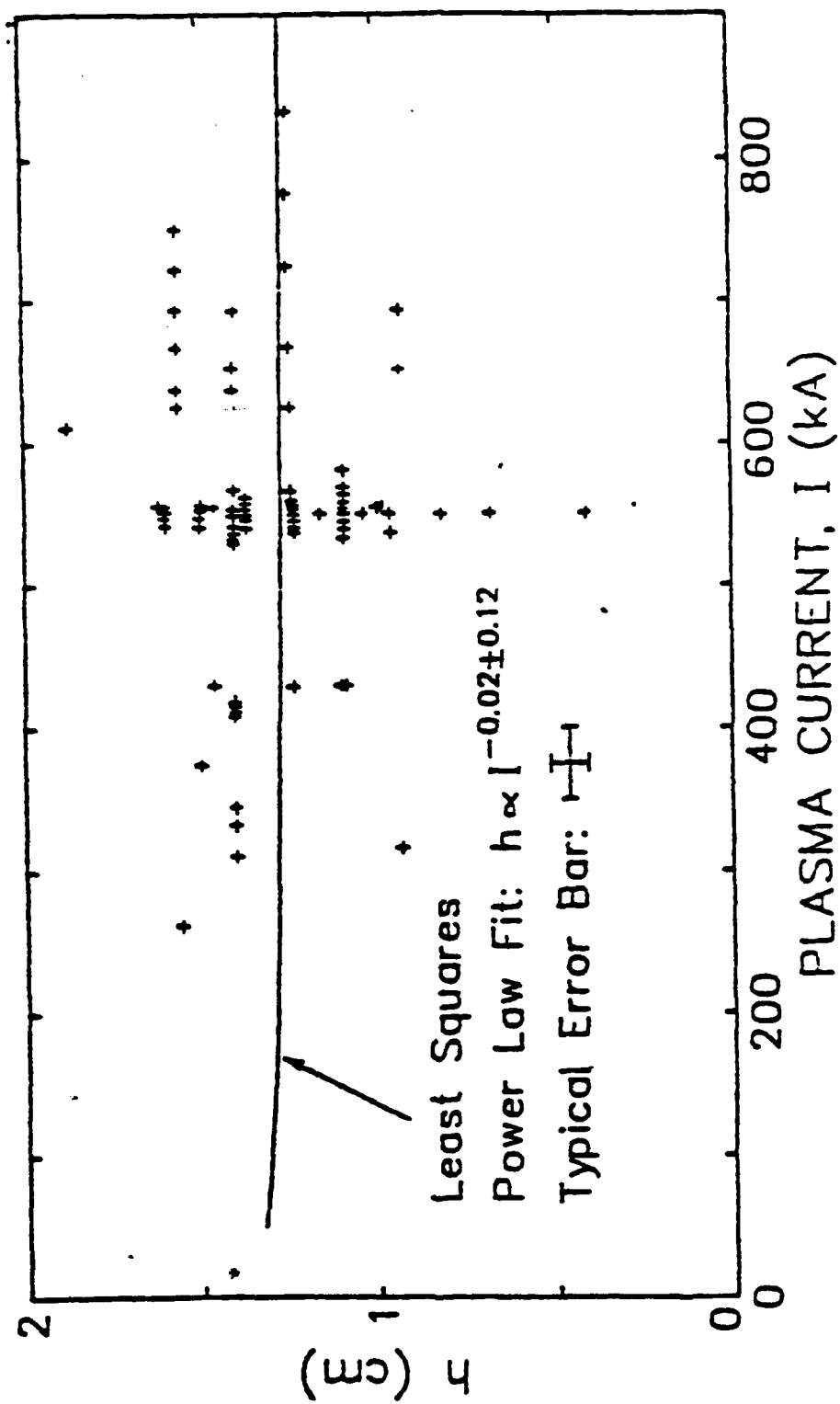


Figure 4.1
Plasma Current Scaling of Pinch Length [30]

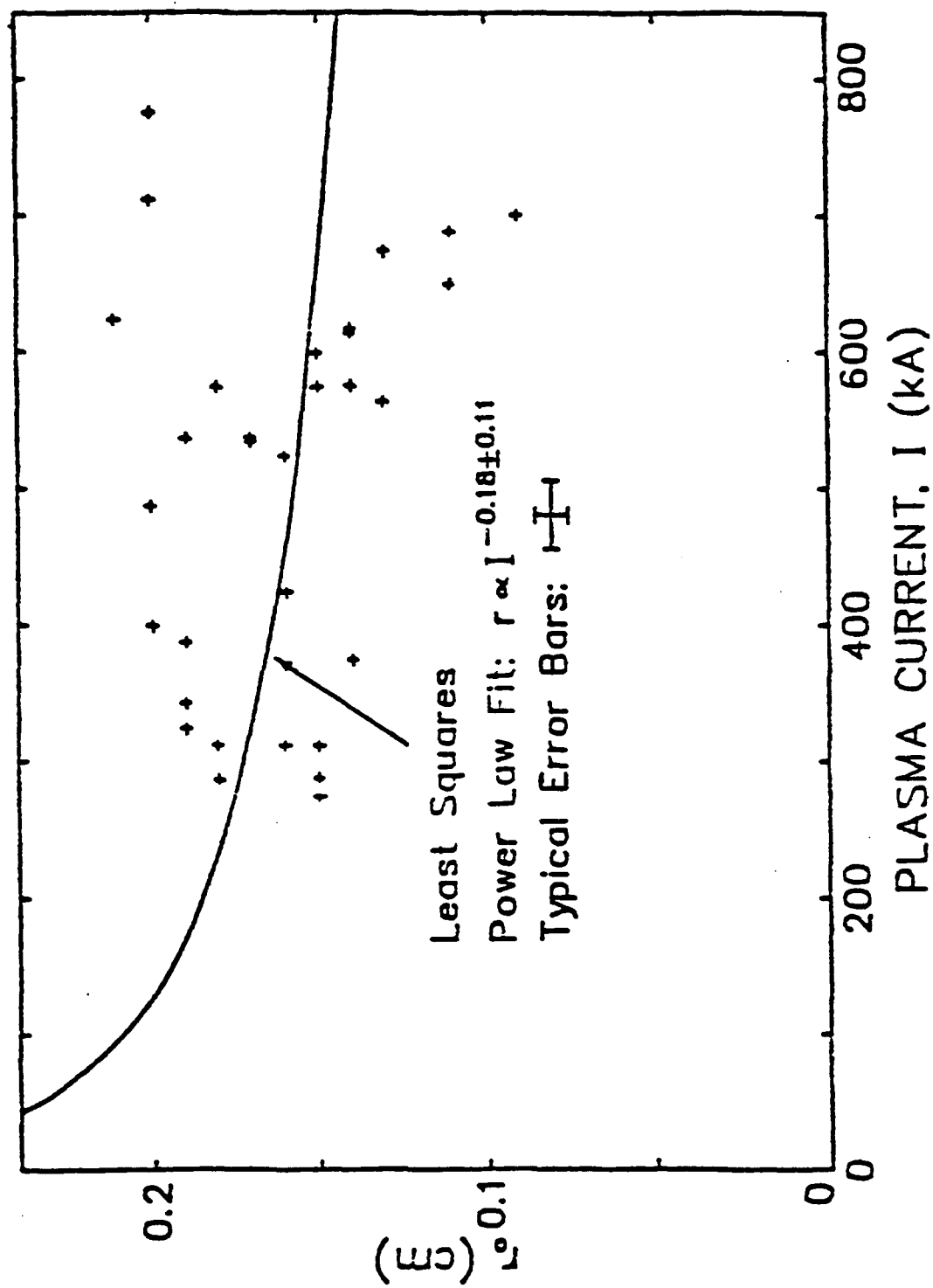


Figure 4.2
Plasma Current Scaling of Pinch Radius [30]

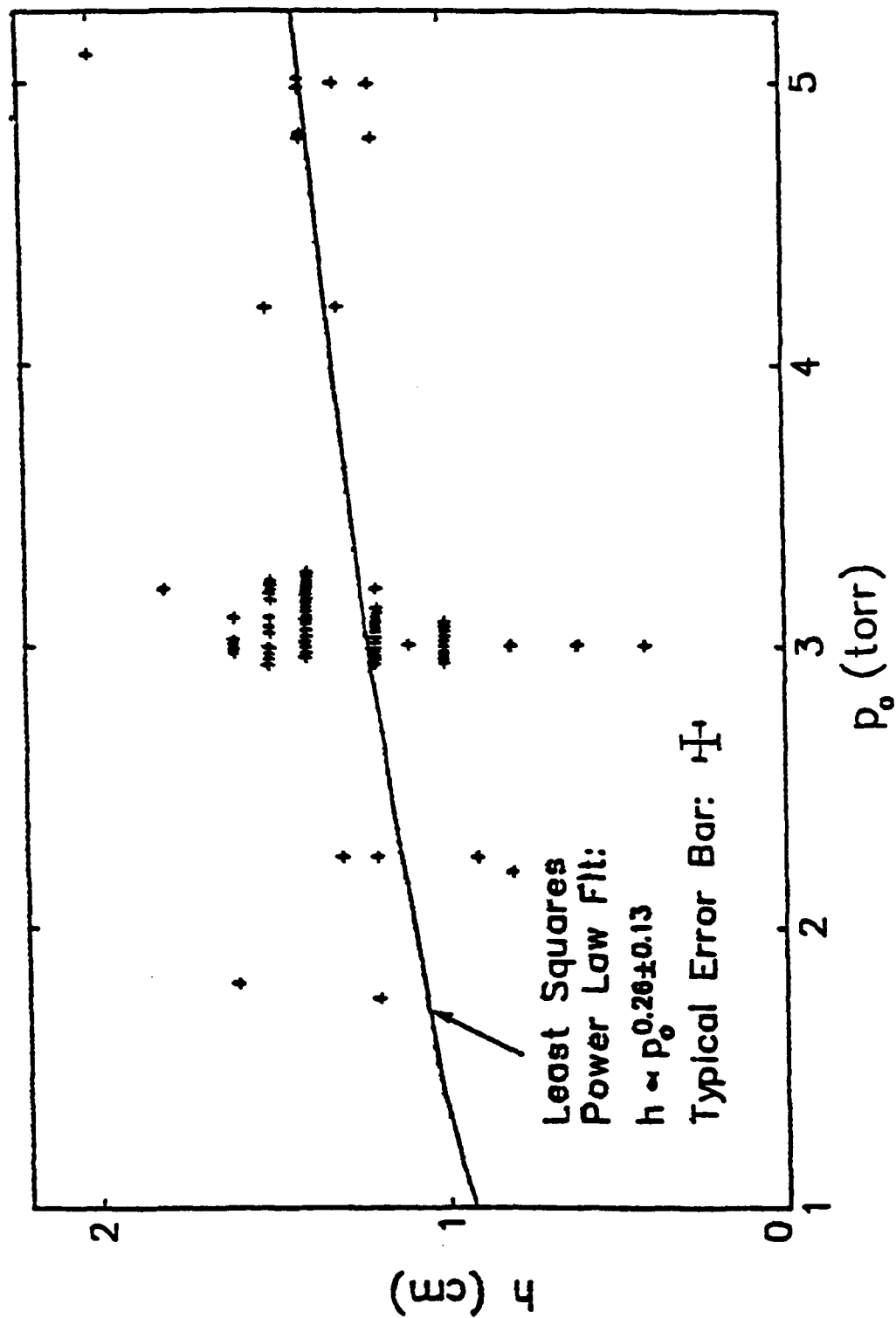


Figure 4.3
Deuterium Filling Pressure Scaling of Pinch Length [30]

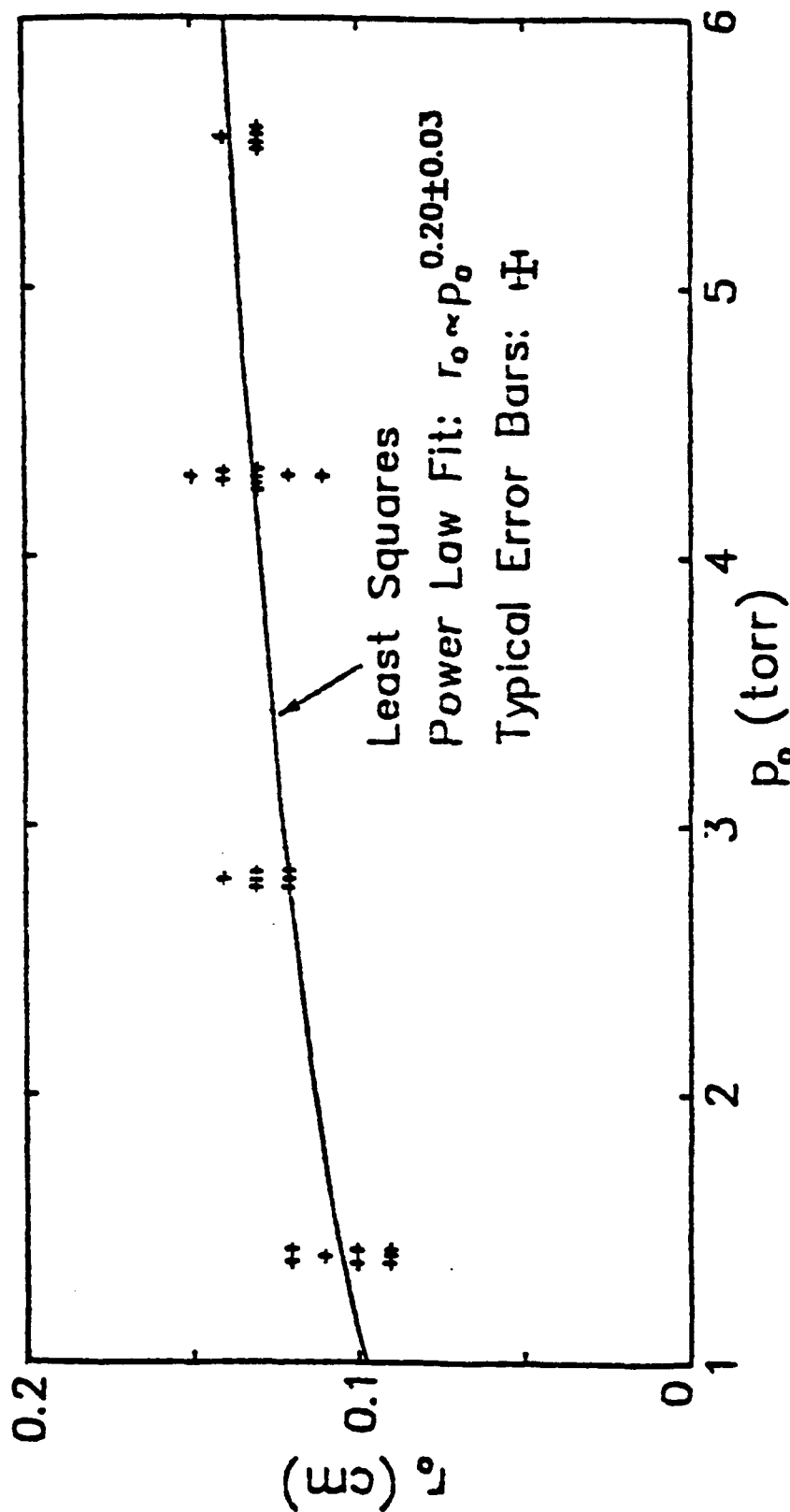


Figure 4.4
Deuterium Filling Pressure Scaling of Pinch Radius [30]

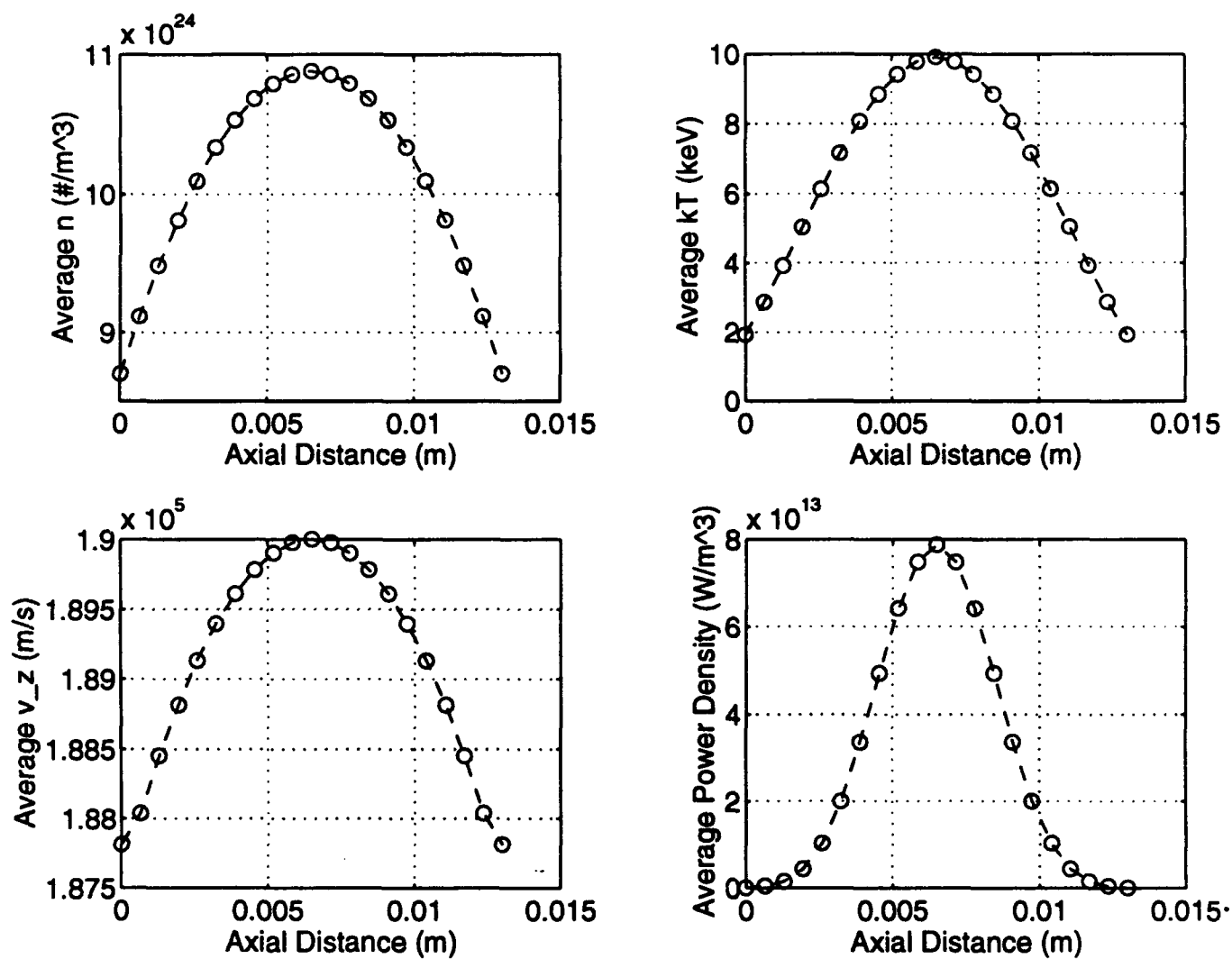


Figure 4.5
Typical Test Axially Averaged Profiles of Ion Number Density n , Kinetic Temperature kT , Axial Velocity v_z , and Fusion Power Density

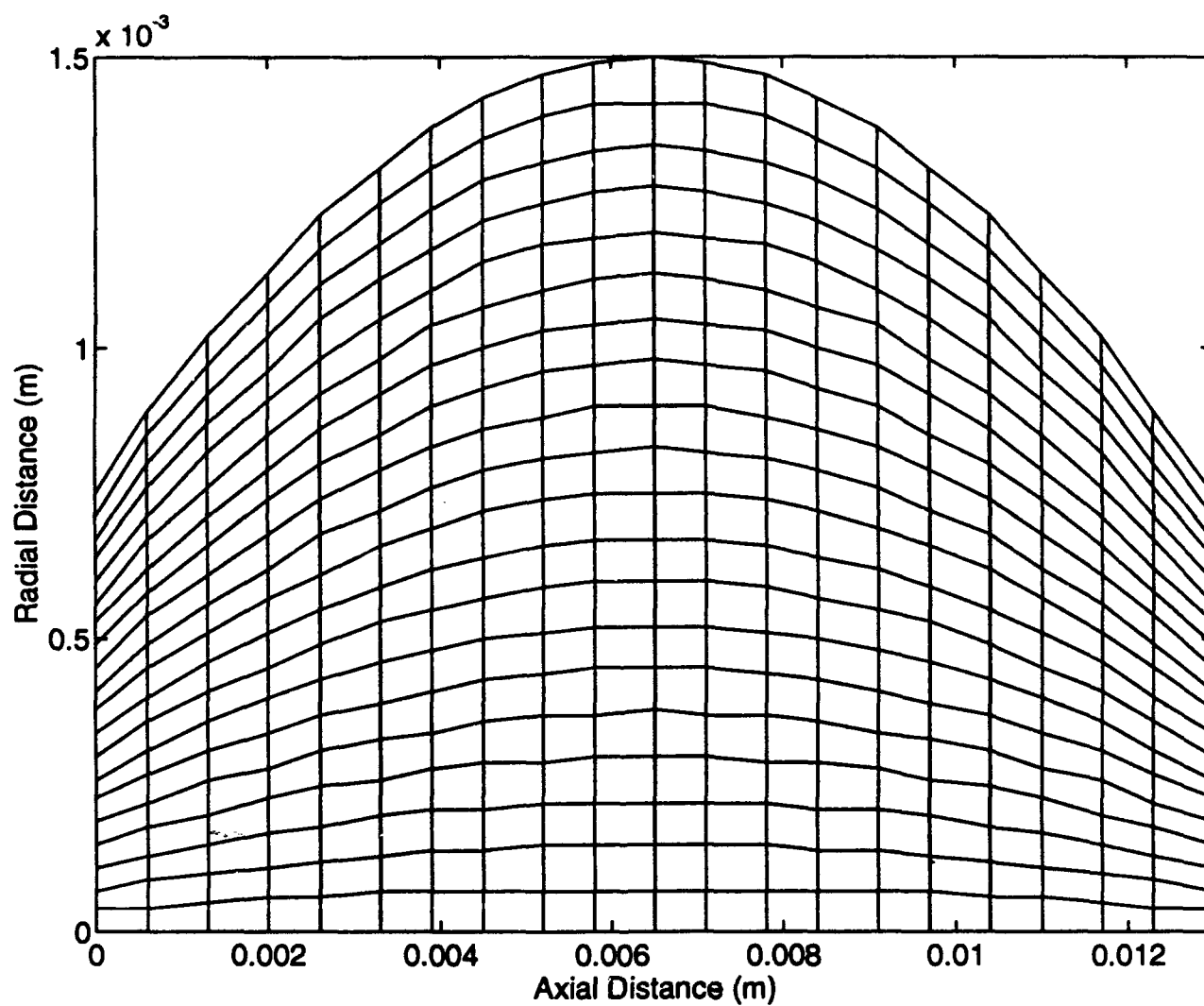


Figure 4.6
Computational Mesh Used in Pinch Calculations (20-by-20)

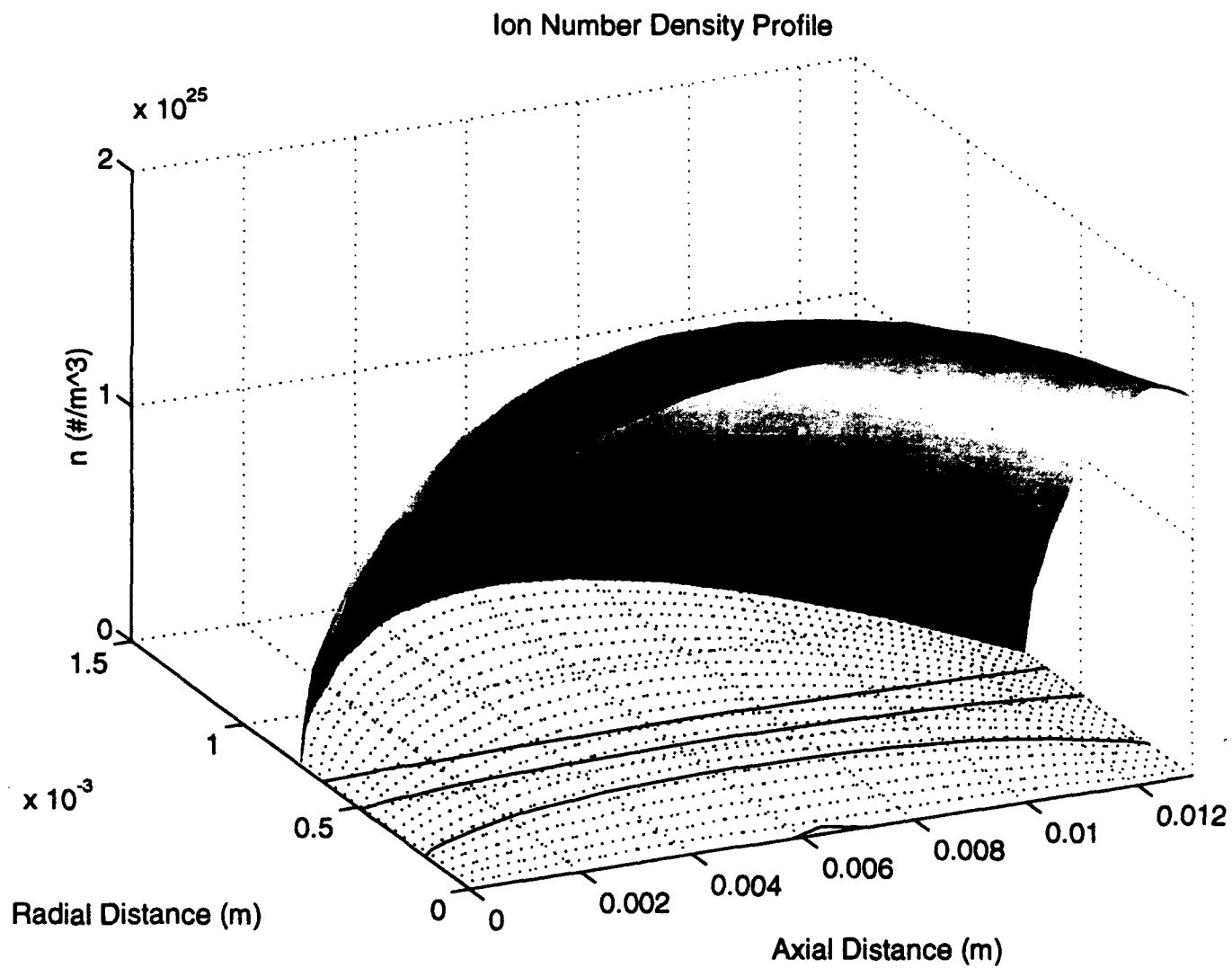


Figure 4.7
Typical Test Input Ion Number Density Profile

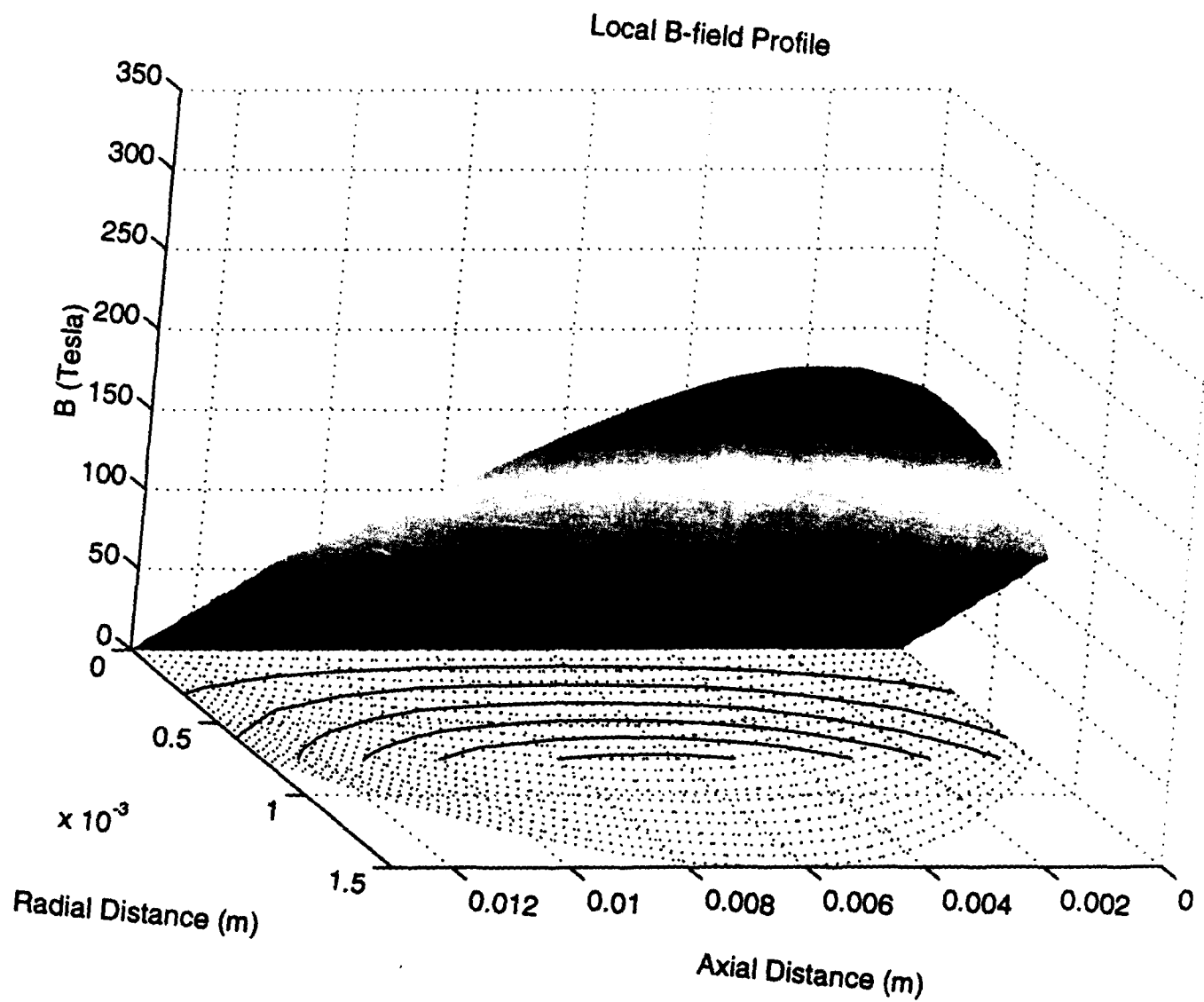


Figure 4.8
Typical Test Local Magnetic Field Profile

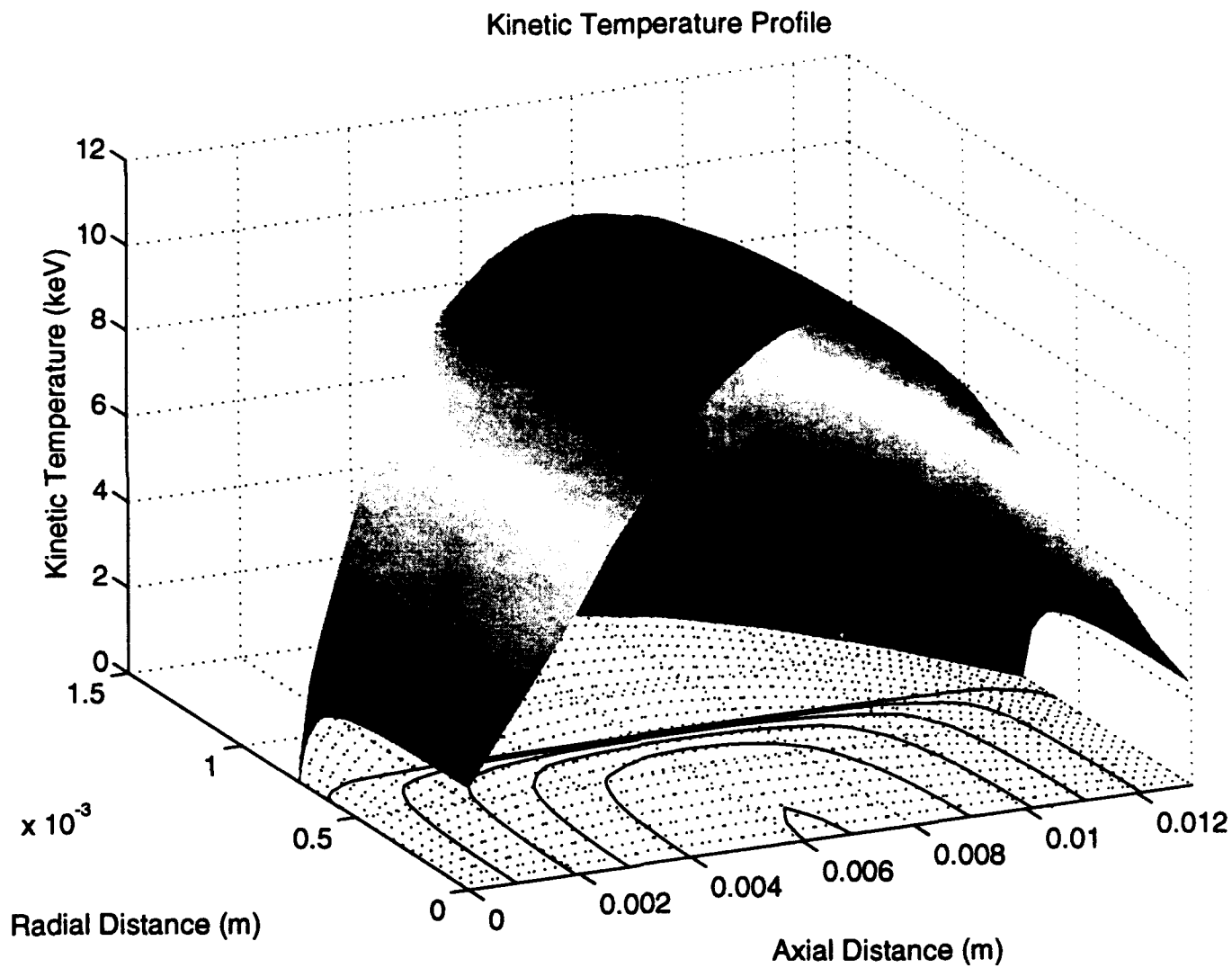


Figure 4.9
Typical Test Resultant Kinetic Temperature Profile

digression from the tokamak shape for the kT profile is that the profile approaches maximum values much more rapidly moving into the pinch radially than does the n profile. Thus, the factor in the kT profile may be more appropriately given by 0.1 rather than the assumed 0.9 of the tokamak profile used in establishing the $m = 0$ drift model's feasibility (see Eq. (3.1)). This is also evidenced by the kT contour lines (solid lines) appearing in Figure 4.9, while the streamlines in the pinch are marked by the dashed lines, which follow the shape of the pinch. By varying the current, a number of runs yielded the corresponding thermonuclear reaction power yields, giving the relation illustrated in Figure 4.10, from which a scaling of $P_f \sim I_p^{5.4}$ is found. Figure 4.11 shows that the inherent current-squared scaling of kinetic temperature density (or energy density) as assumed in this study holds. Closer investigation will reveal a slope of 2 on the log-log plot of Figure 4.11. One should bear in mind that Figures 4.10 and 4.11 are log-log plots. Calculating the slopes on such plots yields the scaling exponent directly.

Now earlier it was established that experimental scalings of neutron yield with current were characterized by an exponent value of 3.3 to 4.0 for the pinch current in the scaling relation. Of course, such relations were based on the use of a D-D fuel mixture, while here we are utilizing a D- ^3He fuel mixture. The use of this fuel mixture in experiments has been rare, but a group led by Hirano did make use of it [33]. They used the ratio of D-D neutrons produced to D- ^3He protons produced to determine the temperature of the plasma. In the kinetic temperature (kT) region of interest for the runs which were performed (typically average kT values between 8 and 15 keV), the reaction rate parameter curve for D- ^3He varies more rapidly than the D-D curve, thus offering a reason for the scaling exponent of the pinch current being larger than those reported for D-D systems. Because fusion power is directly proportional to the reaction rate, the fusion power should also be directly proportional to the number of particles produced for a given reaction. Therefore, it is the reaction rate parameter curves which are responsible for the favorable scaling of the fusion power with pinch current.

DPF Propulsion System Application of Scaling Relations

From the findings discussed in the previous section on pinch scaling relations, the application of such results was introduced into a DPF propulsion code developed earlier [1,2,23]. Before relating the results, a brief explanation of appropriate performance characteristics for a space propulsion system is warranted. Continuing from a discussion of fusion power output calculations mentioned previously in pinch scaling relations, one remembers that the fusion power output is equal to the product of fusion power density and pinch volume. The usable fraction of this power is reduced by radiation loss power in the form of bremsstrahlung and synchrotron

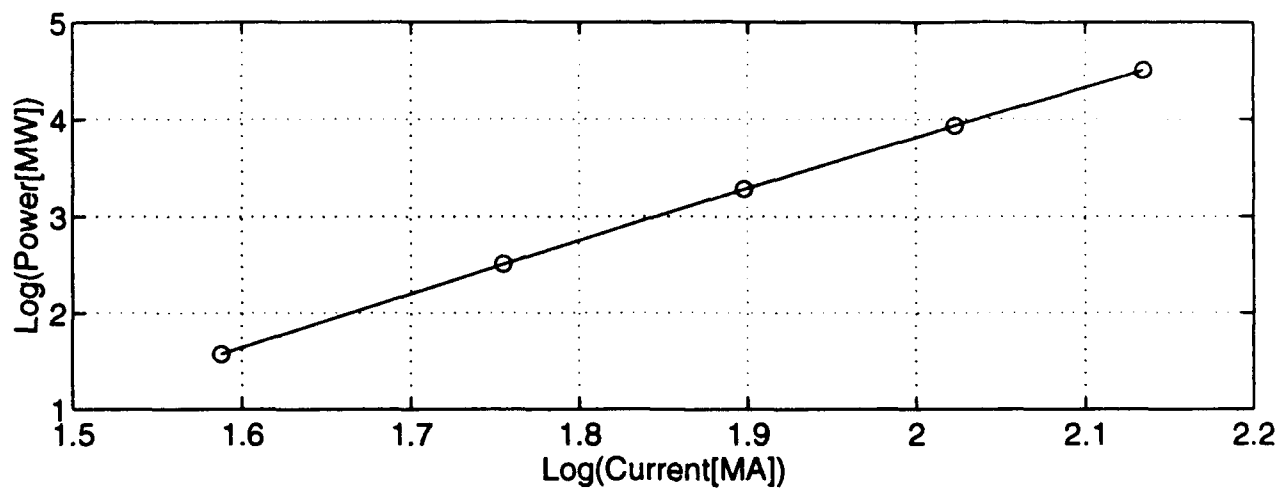


Figure 4.10
Scaling of Fusion Power Output with Axial Current

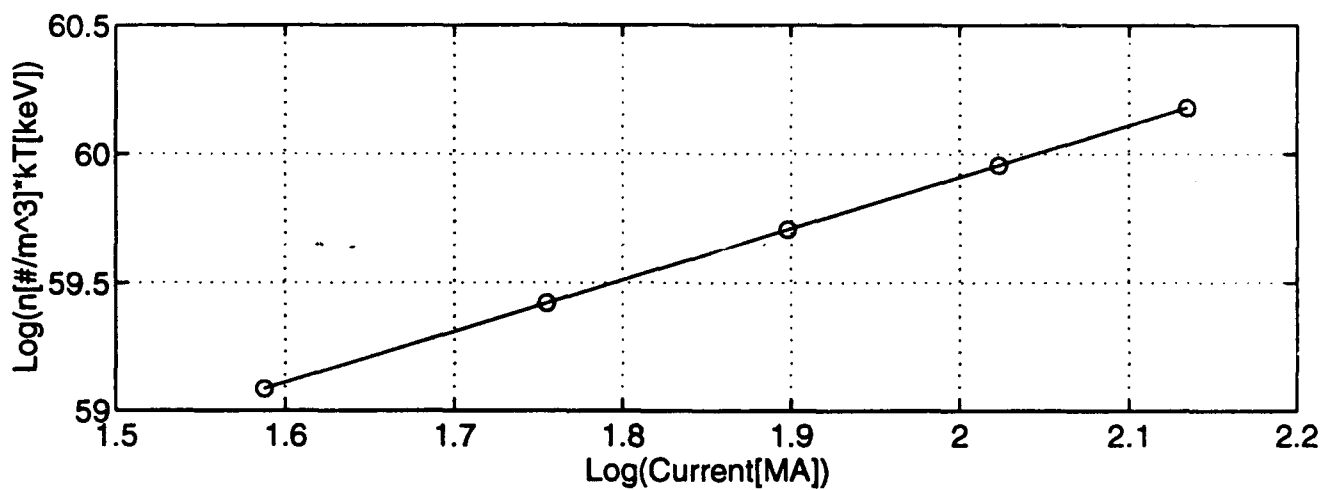


Figure 4.11
Current-Squared Scaling of Plasma Energy (Kinetic Temperature) Density

radiation [26]. The remaining power recharges the capacitor banks on board the DPF propulsion system and heats the propellant released during its operation.

The portion which heats the propellant is the exhaust power P_{ex} . The combination of reaction products and propellant spewing forth from the exit of the DPF system creates the thrust which propels the vehicle. The exhaust velocity of the propellant is written in terms of the exhaust power and the exhaust thrust F_{ex} as [23]:

$$v_{ex} = 2.0 \frac{P_{ex}}{F_{ex}} \quad , \quad (5.1)$$

where the factor of 2.0 has come from exhaust velocity enhancement due to the use a magnetic nozzle to direct the exiting fusion reaction products and ionized propellant particles. From the value of v_{ex} , one of the primary performance parameters is determined--the specific impulse (I_{sp}). Roughly, I_{sp} can be considered as the efficiency of the vehicle's propulsion system as a whole, i.e., its "miles per gallon" value. High values of I_{sp} can enable missions requiring interplanetary traveling distances and large changes in vehicle velocity that systems with low specific impulses cannot achieve. For a thrust parallel to the exhaust velocity ($F_{ex} \cdot v_{ex} = F_{ex} v_{ex}$), the specific impulse of the system is written as:

$$I_{sp} = \frac{v_{ex}}{g} \quad , \quad (5.2)$$

and the thrust by:

$$F_{ex} = m_{propellant} v_{ex} \quad . \quad (5.3)$$

Here, $m_{propellant}$ is the mass flow rate leaving the vehicle. Of the mass flow, the fraction of it which is propellant is much, much greater than the portion of it which is fusion product particles, so the mass flow rate is approximated by the mass flow rate of the propellant alone with very little error. The term g is simply the gravitational acceleration of the earth at sea level. With g as the chosen constant of acceleration, I_{sp} is used as a gauge of performance to compare space propulsion systems.

Rather than the thrust alone being used as a benchmark for space vehicle performance, a quantity of greater importance is the thrust-to-weight [F/W] ratio, which is simply the ratio of the thrust F to the total weight of the vehicle ($W = m_{veh} g$) at a given time, i.e., the system "horse

power." Use of the thrust-to-weight ratio and the specific impulse together provides a good way of comparing space propulsion system performances.

Utilizing the resulting profiles obtained in this study, the existent propulsion system code was altered to include the detailed pinch calculations considered in previous sections. For a one-thruster base case of $\Delta v = 10$ [km/s], pinch current ≈ 20 [MA], and propellant mass flow rate = 30 [kg/s], the major performance parameters listed in Table IV are obtained. Also shown are the results given in the earlier study of enhanced electrode designs [2]. In that work, the parameters shown in Table IV were obtained for this base case considering the use of the Livermore-I DPF and then the use of the enhanced electrode design (EED) DPF which was determined. It is evident that a more detailed treatment of the pinch region has led to less promising values of the F/W ratio and specific impulse for the given pinch current of 20 [MA], although at higher pinch currents of 30 to 40 [MA], the more detailed treatment produces results perhaps even more favorable than those mentioned in earlier reports.

Table IV
Comparison of Performance Parameters for Livermore-I DPF,
Enhanced Electrode Design DPF, and Detailed Pinch DPF Propulsion System Test Cases

<u>Parameter</u>	<u>Livermore-I DPF</u>	<u>EED DPF</u>	<u>Detailed Pinch DPF</u>
Total Mass [kg]	3.69E5	3.59E5	5.59E5
Total Thrust [N]	4.73E5	4.84E5	9.07E4
Thrust-to-Weight	0.131	0.137	0.0165
Specific Impulse [s]	1583	1607	973.6

After running various cases with the new scaling considerations and pinch calculations incorporated into the existing propulsion code [1], some typical mission-required axial profiles are shown in Figure 4.12. In comparing these profiles with the earlier test case profiles of Figure 4.5, it is evident that the parameters required in space propulsion are greater value. In the two cases being compared, the axial velocity distribution is the same, while the number density profile has been increased by an order of magnitude. The resulting kT axial profile shows the same behavior, but its value has increased an order of magnitude as well. What is striking is the considerable increase in the fusion power density emerging from the pinch--an increase of over 4 orders of magnitude. The distribution of power emerging from the pinch has also become less centralized axially. For illustration, the assumed ion number density profile for a typical mission-required regime of operation is shown in Figure 4.13, while the subsequently determined profiles of local magnetic field and kinetic temperature are presented in Figures 4.14 and 4.15, respectively.

In order to gain an understanding of the effects on propulsion performance, a set of 18 test cases were considered, in which the basic variables were the axial velocity in the pinch and the ion number density in the pinch. Figure 4.16 gives a surface representation to each of these 18 test

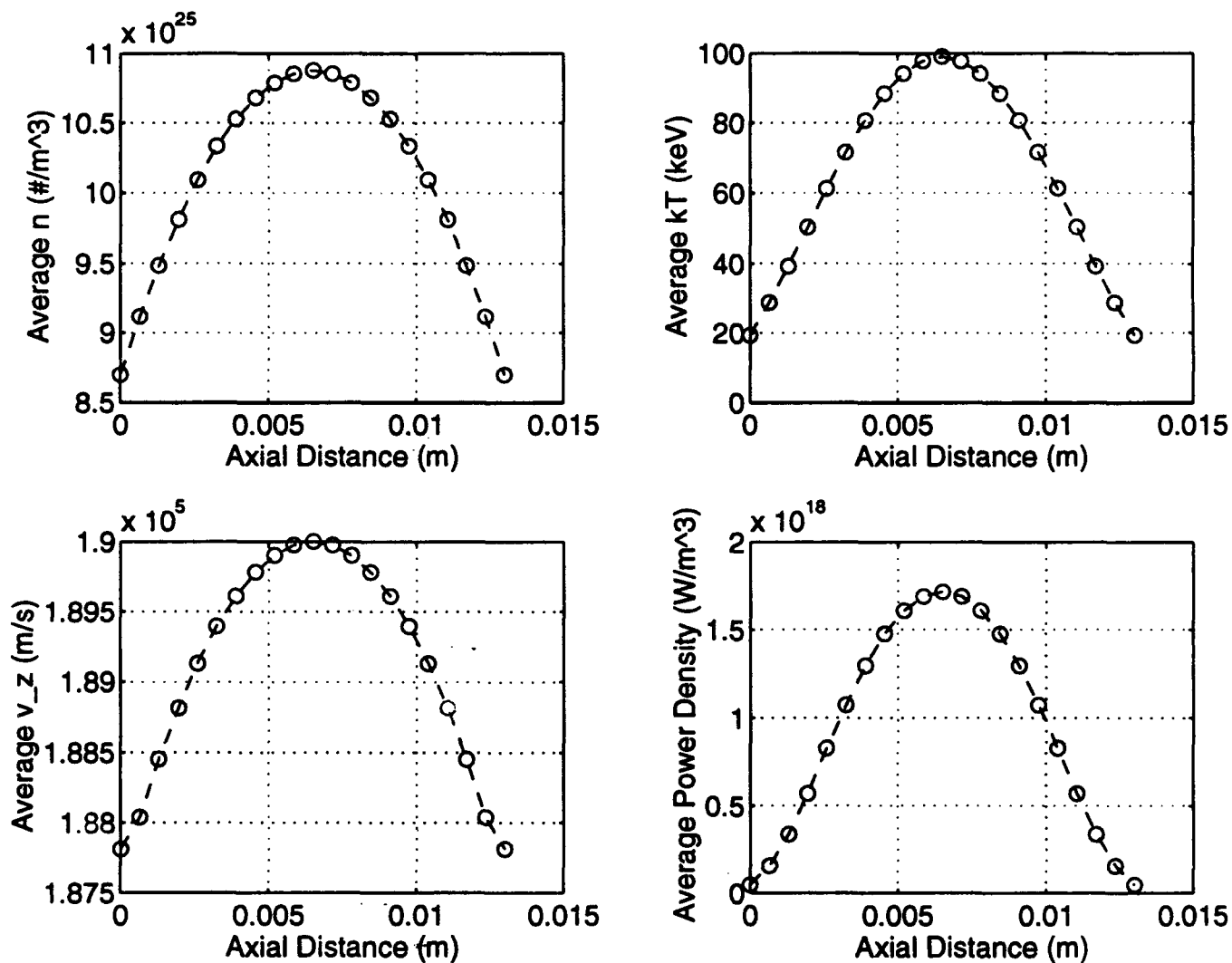


Figure 4.12
Typical Mission-Required Axially Averaged Profiles of Ion Number Density n , Kinetic Temperature kT , Axial Velocity v_z , and Fusion Power Density

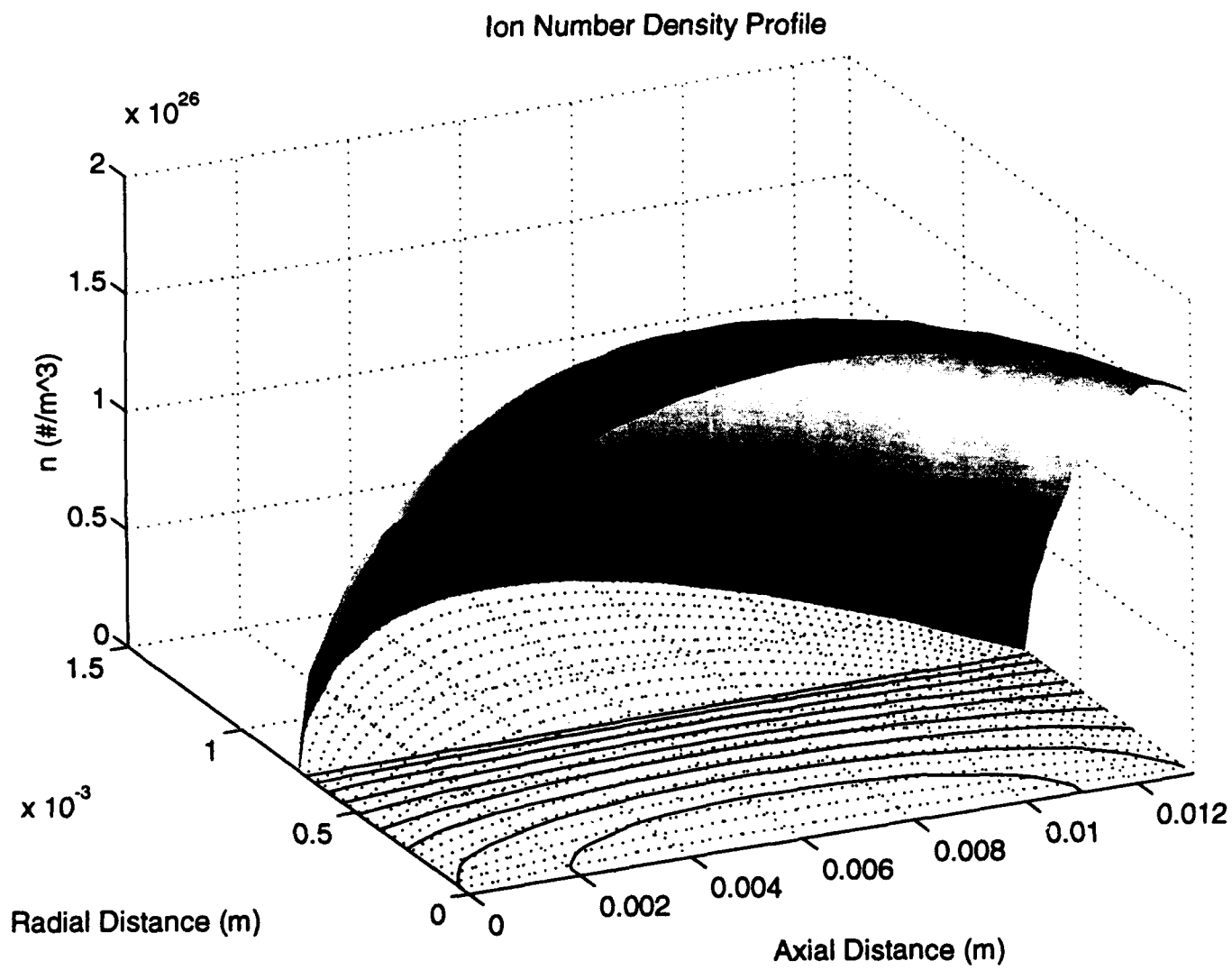


Figure 4.13
Typical Mission-Required Input Ion Number Density Profile

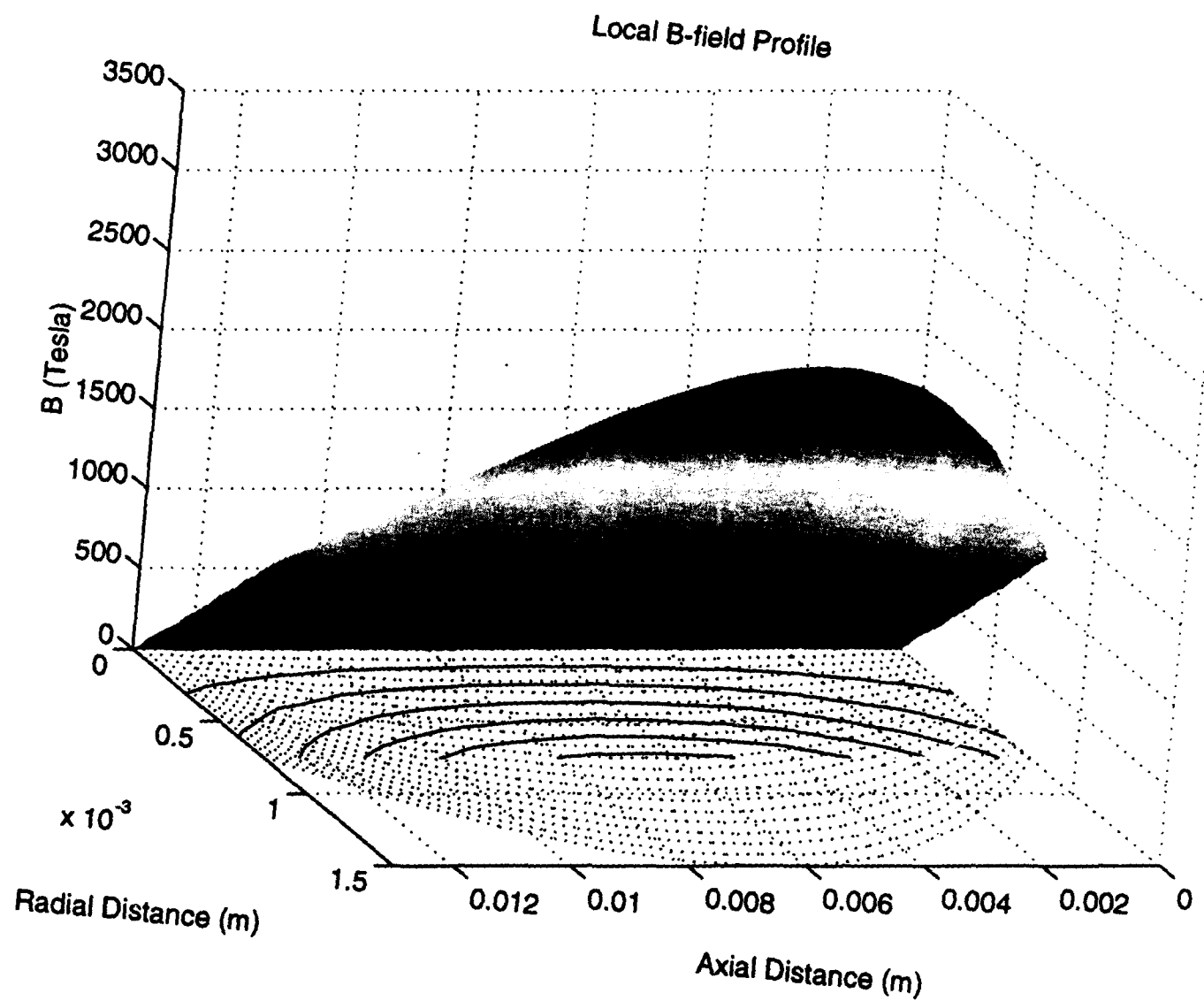


Figure 4.14
Typical Mission-Required Local Magnetic Field Profile

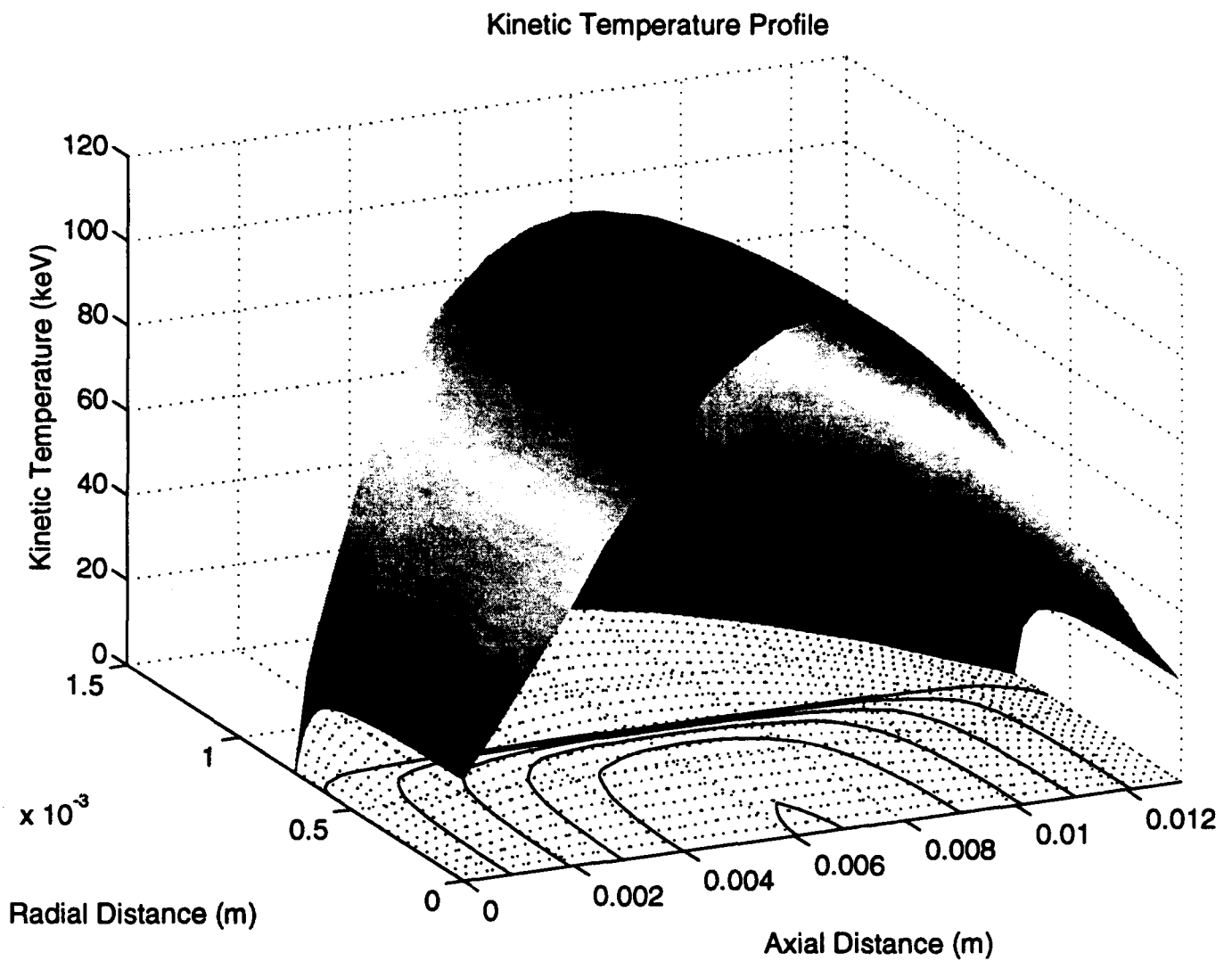


Figure 4.15
Typical Mission-Required Resultant Kinetic Temperature Profile

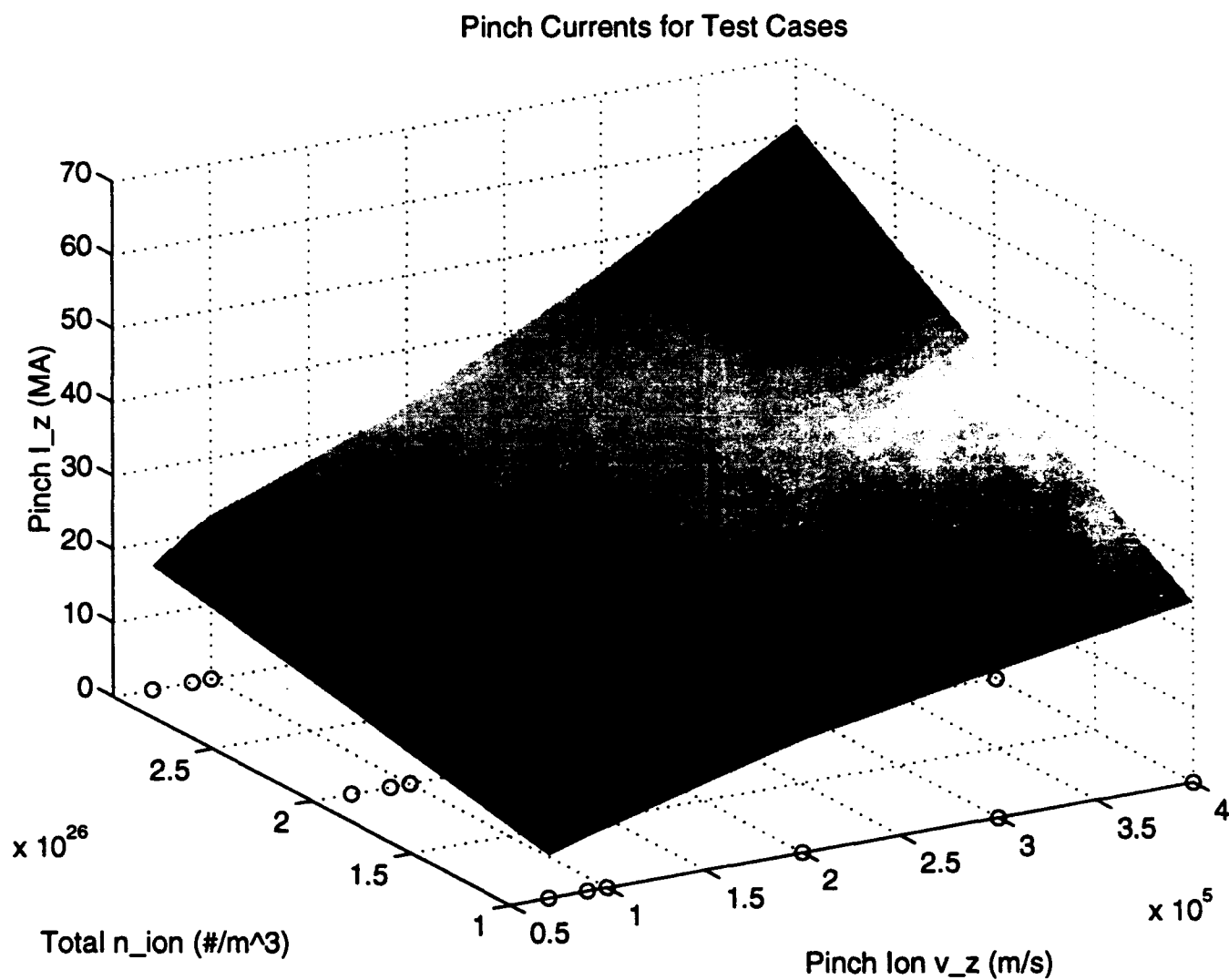


Figure 4.16
Pinch Currents Associated with the 18 Test Case Combinations of Ion
Number Density and Axial Velocity

cases. Three values of ion number density were used: 1.0, 2.0, and $3.0 \cdot 10^{26} \text{ [m}^{-3}\text{]}$, while six values for the pinch axial velocity were chosen: 0.7, 0.9, 1.0, 2.0, 3.0, and $4.0 \cdot 10^5 \text{ [m/s]}$. In choosing these values, the previous project work regarding the propulsion code was considered, as well as observances of the results obtained from making a number of test runs before deciding on a precise test grouping. By observing the $I = 0$ plane of Figure 4.16, the projections of the test case points from the surface are visible. It was generally noted that velocities below $0.7 \cdot 10^5 \text{ [m/s]}$ could not generate enough fusion power to heat any propellant mass, while number densities and axial velocities *beyond* those chosen yielded unheard of values for the pinch current, meaning currents on the order of 100 [MA] or greater.

Some general findings will now be presented. Figure 4.17 presents a base set of parameters including a 4-thruster device and a mission velocity increment of 10 [km/s]. By varying the propellant mass flow rate from 10 to 20 to 30 [kg/s], it was shown that increasing the rate increases the F/W ratio and decreases the specific impulse. This remains consistent with the results found in earlier project reports [1,2], as expected. The vast majority of the output found in this report is akin to that shown in Figures 4.18 and 4.19, where for specified values of n , v_z , Δv , and propellant mass flow rate, the resulting values of pinch current, specific impulse, and thrust-to-weight ratio are plotted as a surface for a number of thrusters varying from 1 to 4. In total, five values of propellant mass flow rate (1, 5, 10, 20, and 30 [kg/s]) and three values of Δv (10, 20, and 40 [km/s]) were chosen to vary with the 1, 2, 3, and 4-thruster configurations. This results in 60 total *mission* cases, not to be confused with the 18 *test* cases previously mentioned. Only the 1 [kg/s] flow, 10 [km/s] Δv cases are shown in the present section, with the remainder of them found in Appendix A.

In Figure 4.20 a surface plot of the variance of DPF system operating energy as a function of the F/W ratio and the specific impulse is presented for the purpose of visualizing the energy requirements of such a system, while in Figure 4.21, scaling laws for the fusion yield are revisited. It was observed how the key performance parameters for the 18 test cases varied when considering fusion number yield scaling of pinch current to the 2nd, 3rd, 4th, and 5th powers. It is evident that for a given test case, the *lower* scaling is more favorable, at least for the higher performance cases, coinciding with the 30 to 40 [MA] "magic" zone of operation before performance begins falling. This magic zone behavior is present in all of the plots of the type found in Appendix A. Physically, it seems that the culprit behind the lessened performance is the reaction rate parameter curve for the D-³He reactions, which begins to plateau and decrease for kinetic temperatures exceeding 100 [keV]. Also, regarding the seemingly better performance for lower scalings, it should be noted that a fuel cycle modeling is not present in the propulsion code. Once a fusion fuel particle has reacted, it is considered to not have any effect on subsequent fusion reactions. The decreasing number density and, thus, the decreasing current over the lifetime of the

Effect of Propellant Mass Flow Rate on Isp and F/W Using 4 Thrusters

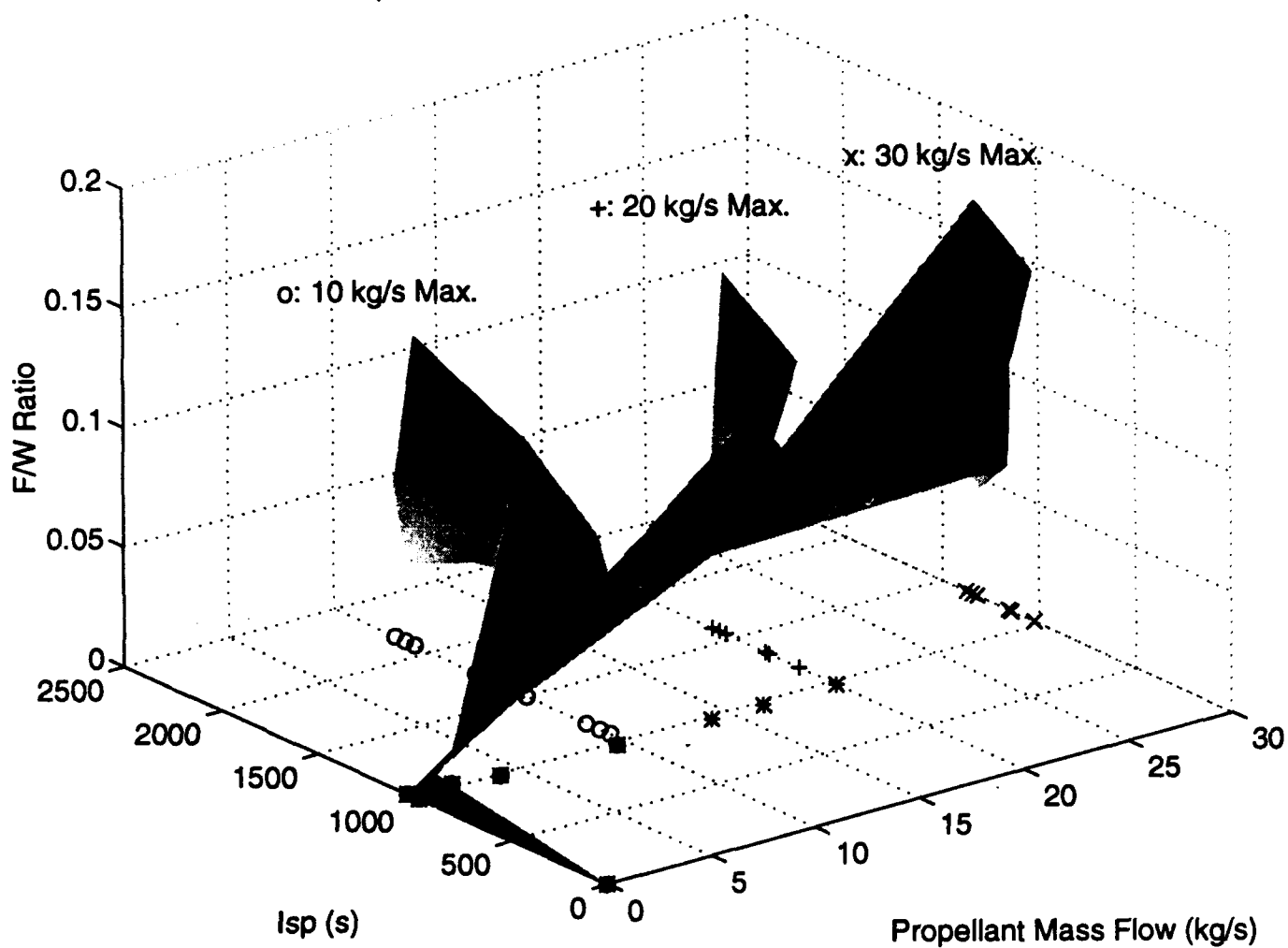


Figure 4.17
Effect of Propellant Mass Flow Rate on Specific Impulse and F/W Ratio in 18 Test Cases at 3 Different Rates for a Δv of 10 [km/s] Using a 4-Thruster System

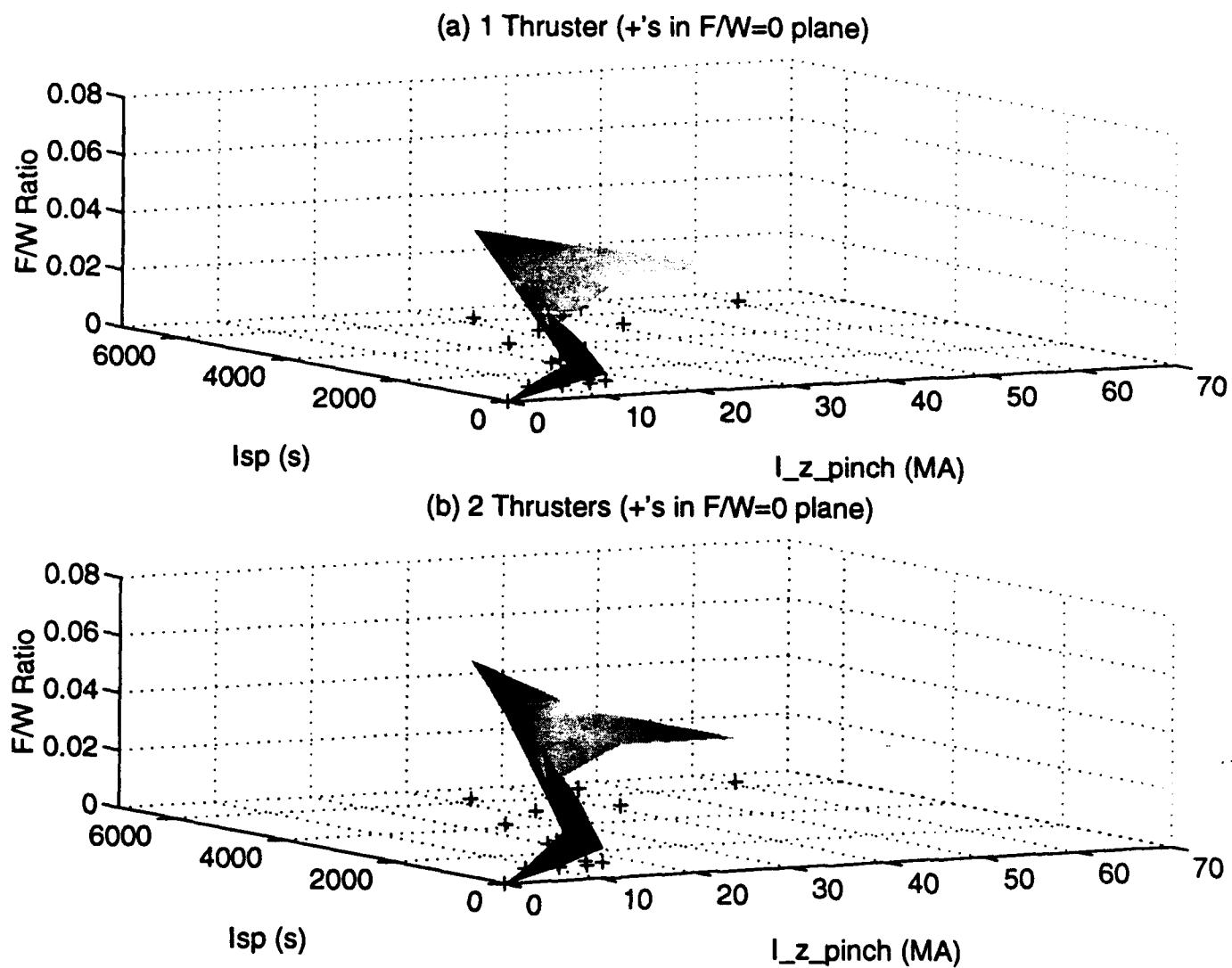


Figure 4.18
Pinch Current, Specific Impulse, and F/W Ratio for Propellant Mass Flow Rate of 1.0 [kg/s] and $\Delta v = 10$ [km/s] with (a) 1 Thruster and (b) 2 Thrusters

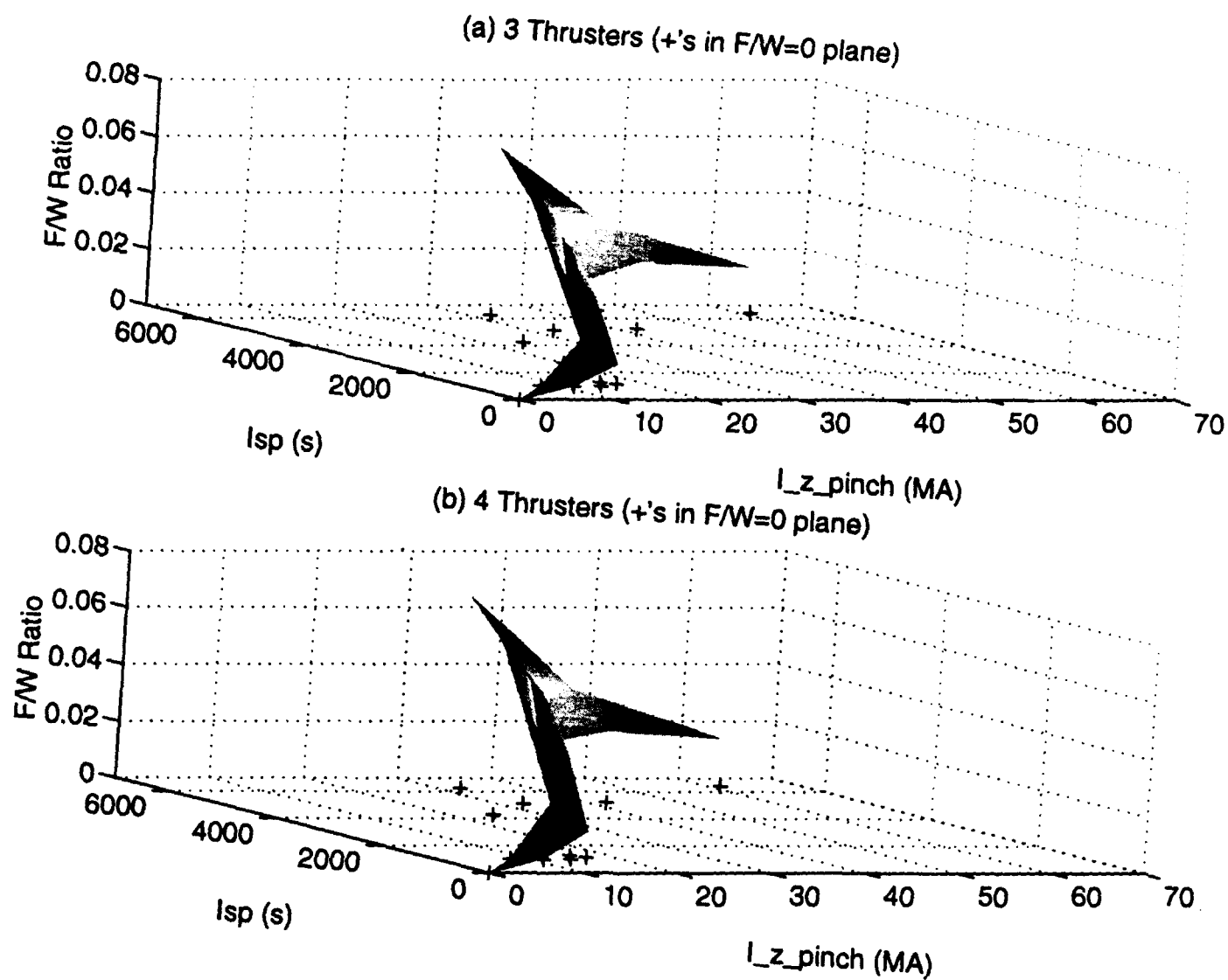


Figure 4.19
Pinch Current, Specific Impulse, and F/W Ratio for Propellant Mass Flow Rate of 1.0 [kg/s] and $\Delta v = 10$ [km/s] with (a) 3 Thrusters and (b) 4 Thrusters

Operating Energies for Test Cases at 3 Propellant Flow Rates Using 4 Thrusters

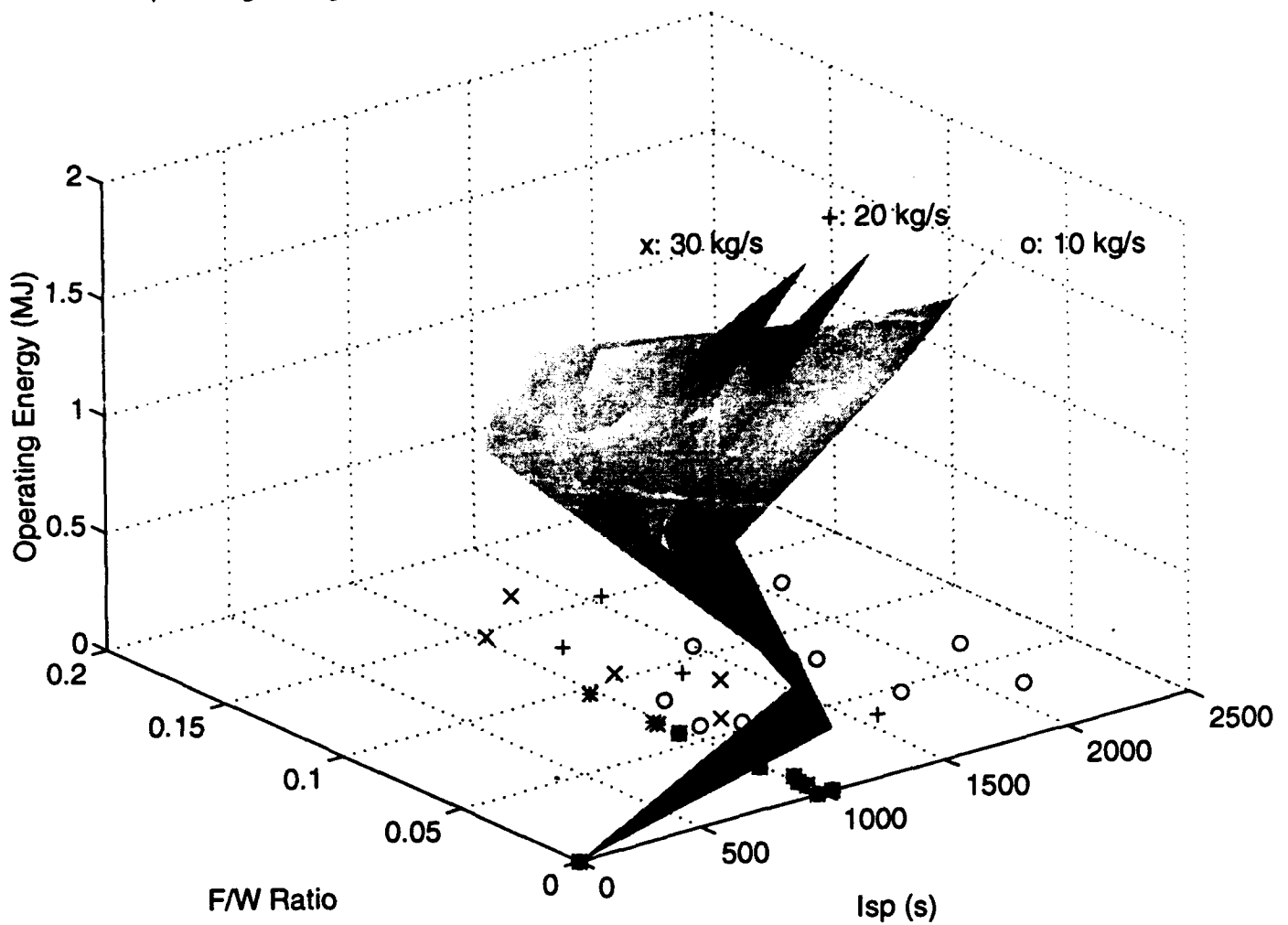


Figure 4.20
DPF Operating Energies vs. F/W Ratios and Specific Impulse Values for Propellant Flow Rates of 10, 20, and 30 [kg/s] Using 4 Thrusters with a Δv of 10 [km/s]

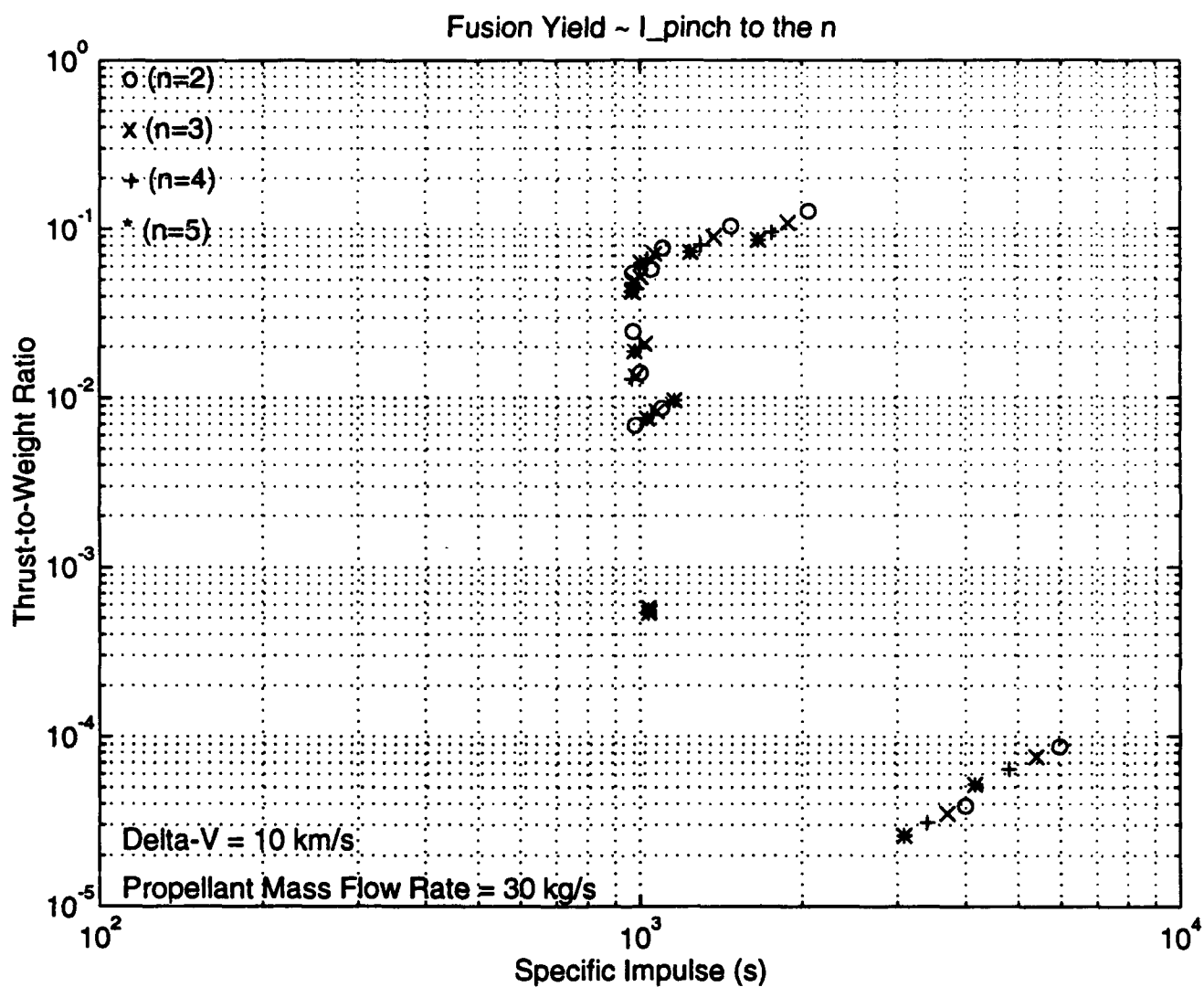


Figure 4.21
Effect on Performance Parameters for Various Scalings of Fusion Number Yield with Pinch
Current ($Y_p \sim I^n$, with $n = 2, 3, 4, 5$)

pinch are more noticeable at the higher scaling exponents. It would seem that the quicker depletion of the resource fuel particles early in the pinch phase, while leading to higher initial power output, also leave fewer particles at the end of the pinch phase to react. Thus, the lifetime of the pinch seems to also play a key role in the scaling considerations for the pinch, at least as far as propulsion performance is concerned.

CONCLUSION AND RECOMMENDATIONS

In completing this current three-year project, work has moved from an overall propulsion system standpoint inwardly to the mechanisms which are at work in the pinched plasma itself. It was determined during the first year's work that an impulsive mode of operation gave the best propulsion system performance. For a mission requiring a Δv of 40 [km/s], a F/W ratio of almost 0.08 and a specific impulse of 4000 [s] were possible with 4 thrusters operating at 20 [MA]. This was the optimum operating regime for the impulsive mode. Continuous firing modes fell two orders of magnitude short of the required F/W ratios for manned space travel. Also researched in the first year of the project was the benefits derived from spin polarization of the D-³He fusion fuel. Power output increases from the fusion reactions of 20% to 50% were found to be possible in relation to the reaction rates of the thermonuclear reactions. This consequently increases both the F/W ratio and the specific impulse of the system. Spin polarization may also work to suppress the D-D side reactions, thus meaning that the power increase of 50% could be considered a total power increase in the system [1].

Moving into the second year of work in the project, the effects of the electrical system configuration on the propulsion performance figures of merit were investigated. An equivalent circuit of the DPF device was devised for use in a 1-D transient code to determine sheath dynamics during the rundown phase. The leakage current was modeled as a constant resistance which removed current from the plasma sheath. The Livermore-I DPF was used for comparison with the test cases thus obtained. Various radial and axial anode variations were studied as a means of modifying the Livermore-I device to achieve the necessarily high current needed to heat the pinch. It was found that the electrodes did not need to undergo formidable changes in order to achieve the high current requirements of 10 to 20 [MA]. Instead, it was the charging voltage which needed drastic increases, with those increases being greater than what is available today. For the state of the art in high current pulse power technology, the reference is the SHIVA experiment at Kirtland Air Force Base, which utilizes a load current of 9 [MA] at a charging voltage of 125 [kV]. An increase of ~25% in the charging voltage would be required, as well as a circuit which could handle the high current levels. The end result of altering the electrode configuration is a lessening of the required capacitor bank mass, which necessarily increases the F/W ratio. The study provided a more realistic view of the requirements needed for space propulsion feasibility of the DPF, but the study also provided a more optimistic view of DPF thruster performance as a result of the electrode modification investigation [2].

These first two years of work led into the final phase of the project: scaling laws and plasma pinch phase physics. Such work has been alluded to in the conclusions of the past two annual reports. Looking at the scaling of pinch size with pinch current has shown that modeling the pinch column as a half wavelength of the $m = 0$ instability based on the electron drift velocity appears to be feasible, having shown that number densities obtained in such a model are of the correct order of magnitude for a DPF device. It remains to be investigated, however, if this model holds for higher current configurations, as the model used here is essentially independent of the pinch current. An appropriate dependency on the current would need to be determined in order to test the model's validity. From the standpoint of the fusion yield scaling with pinch current, a scaling of $P_f \sim I_p^{5.4}$ has been found based on assumed tokamak number density profiles resulting from the pinch size scaling model. P_f is the total fusion power produced in the pinch region, with D-³He and D-D reactions considered in developing the reaction rate parameter [25]. Using the assumption that the magnetic field penetrates into the plasma until reaching a value of zero at the axis of the pinch, the widely accepted I_p^2 -scaling of the energy density (or kinetic temperature density) is obtained. This was done by assuming the vacuum magnetic boundary pressure at the edge of the pinch is equal at all times to the sum of the particle and local magnetic pressures.

In looking to further research in the pinched plasma region, another key parameter is the fill pressure of the fusion fuels. Further work should be done to see what effects the pressure has on the size and shape of the pinched region, as well as its effect on trapped particle fraction in the pinch. From such a study, one could determine if a low or high-pressure mode of operation is desirable for DPF operation from a flight performance standpoint. Within this idea of pressure mode operation, it is desirable to know if treatment of the plasma kinetic temperature as Maxwellian is appropriate. Hirano, *et al.* [33] indicate a thermonuclear treatment may not be viable for their low-pressure mode operation of 1.5 [torr] made up of equal parts of deuterium and helium-3. They determine a temperature of 11 [keV], while neutron time-of-flight measurements give a value of 3 [keV], thus owing to the uncertainty of the appropriate treatment. Decker, *et al.* make the assertion that if $kT_i \leq 3kT_e$, then the measured neutron outputs cannot be explained by thermonuclear processes [19]. Also, advances in determining the fusion reaction mechanisms, such as the role of filamentary pinch structures, could provide enlightenment as to the desired pressure mode of operation [34]. Other areas of possible research include a study of the effects of electrode and insulator materials [35], the fraction of particles which can be utilized as thrust using the enhancements from a magnetic nozzle, and a design of the DPF propulsion system and vehicle as a whole, beyond the current schematic diagrams.

LIST OF REFERENCES

- [1] Choi, C. K., "Engineering Considerations for the Self-Energizing MPD-Type Fusion Plasma Thruster," PL-TR-91-3087, Phillips Laboratory, February 1992.
- [2] Choi, C. K., and Nakafuji, G. T., "Engineering Considerations for the Self-Energizing MPD-Type Fusion Plasma Thruster," PL-TR-92-3043, Phillips Laboratory, February 1993.
- [3] Friedberg, J. P., Ideal Magnetohydrodynamics, Plenum Press, New York, 1987.
- [4] Filippov, *et al.*, Nuclear Fusion Supplement, Vol. 2, p. 577 (1962).
- [5] Mather, J. W., Physics of Fluids Supplement, Vol. 7, S, p. 28 (1964).
- [6] Conrads, H., "Dense Plasma Focus as a Neutron Source for Fusion Research," Nuclear Science & Engineering, Vol. 106, pp. 299-307 (November 1990).
- [7] Schmidt, H., "The Plasma Focus -- A Review," Atomkernenergie/Kerntechnik, Vol. 36, No. 3, pp. 161-166 (1980).
- [8] Kaeppler, H. J., "Ähnlichkeitsbetrachtungen und Skalierungsgesetze für den Plasmafokus," IPF-74-7, Universität Stuttgart, 1974.
- [9] Kaeppler, H. J., 6th International Conference on Plasma Physics and Controlled Nuclear Fusion Research, IAEA-CN 35 E/18-1, Berchtesgaden, 1976.
- [10] Decker, G., *et al.*, "Current and Neutron Yield Scaling of Fast High Voltage Plasma Focus," IPF-77-2, Stuttgart (1977).
- [11] Decker, G., *et al.*, "Current and Neutron Yield Scaling of Fast High Voltage Plasma Focus," Plasma Physics, Vol. 22, pp. 245-260 (1980).
- [12] Rapp, H., "Experimentelle Untersuchung der Betriebscharakteristik eines Plasmafokus," IPF-74-1, Universität Stuttgart, 1974.
- [13] Shyam, A., and Srinivasan, M., "Neutron Emission from a 100 Joule Plasma Focus," Journal of Applied Physics, Vol. 17, pp. 425-426 (1978).
- [14] Mather, J. W., 4th Conference on Plasma Physics and Nuclear Fusion, University of Wisconsin, 1971.
- [15] Bernard, A., 3rd Topical Conference on Pulsed High Beta Plasmas, Culham, England, Pergamon Press, Oxford, 1976.
- [16] Bernard, A., *et al.*, 6th International Conference on Plasma Physics and Controlled Nuclear Fusion Research, IAEA-CN-35 E/18-4, Berchtesgaden, 1976.
- [17] Oppenländer, T., *et al.*, "The Plasma Focus Current in the Compression Phase," Plasma Physics, Vol. 19, pp. 1075-1083 (1977).

- [18] Stygar, *et al.*, "Particle Beams Generated by a 6 - 12.5 kJ Dense Plasma Focus," Nuclear Fusion, Vol. 22, No. 9, pp. 1161-1172 (1982).
- [19] Decker, G., *et al.*, "Neutron Emission Parameters in Plasma Focus Devices," Proceedings of the Seventh International Conference on Plasma Physics and Controlled Nuclear Fusion Research, Vol. 2, Innsbruck, IAEA, 23-30 August 1978.
- [20] Decker, G., and Wienecke, R., "Plasma Focus Devices," Physica, Vol. 82C, pp. 155-164 (1976).
- [21] Herold, H., *et al.*, "Comparative Analysis of Large Plasma Focus Experiments Performed at IPF, Stuttgart, and at IPJ, Swierk," Nuclear Fusion, Vol. 29, No. 8, pp. 1255-1269 (1989).
- [22] Shyam, A., and Srinivasan, M., "Experimental Study of Plasma Characteristics of Plasma Focus Devices," Indian Journal of Pure & Applied Physics, Vol. 21, pp. 286-288 (May 1983)
- [23] Leakeas, C. L., "Parametric Studies of Dense Plasma Focus for Fusion Space Propulsion with D-³He," PL-TR-91-3014, Phillips Laboratory, March 1991 [Master's Degree Project, School of Nuclear Engineering, Purdue University, May 1991].
- [24] Cox, L. T., "Thermonuclear Reaction Bibliography with Cross-Section Data for Four Advanced Reactions," AL-TR-89-006, Air Force Astronautics Laboratory, Edwards Air Force Base CA, March 1989.
- [25] Cox, L. T., "Thermonuclear Cross Section and Reaction Rate Parameter Data Compilation," AL-TR-90-053, Phillips Laboratory, July 1991.
- [26] Cox, L. T., "Synchrotron Radiation Considerations in the Dense Plasma Focus (DPF) Magnetoplasmodynamic (MPD) Thruster," PL-TR-92-3035, Phillips Laboratory, July 1992.
- [27] Haloulakos, V. E., and Bourque, R. F., "Fusion Propulsion Study," AL-TR-89-005, Astronautics Laboratory, Edwards Air Force Base CA, July 1989.
- [28] El-Wakil, L., L., Nuclear Energy Conversion, American Nuclear Society, Lagrange Park IL, 1982.
- [29] Choi, C. K., "Nuclear Spin Polarization of Advanced Fuels," AL-TR-89-036, Astronautics Laboratory, September 1989.
- [30] Gerdin, G., *et al.*, "A Scaling Law for Macroscopic Stability of the Mather-type Plasma Focus," Plasma Physics and Controlled Fusion, Vol. 31, No. 9, pp. 1341-1363 (1989).
- [31] Dolan, T. J., Fusion Research, Vol. I, Pergamon Press, Elmsford NY, 1982.
- [32] Pottër, D. E., "Numerical Studies of the Plasma Focus," Physics of Fluids, Vol. 14, No. 9, pp. 1911-1924 (September 1971).
- [33] Hirano, K., *et al.*, "Investigation of Plasma Dynamics and Emission in a Dense Plasma Focus," IAEA-CN-47 / D-IV-5-1, pp. 583-592, 1986.
- [34] Nakafuji, G. T., Private Communication, April 1994.

[35] Beg, F. N., *et al.*, "Effect of Insulator Sleeve Material on Neutron Emission from a Plasma Focus," Physica Scripta, Vol. 46, pp. 152-154 (1992).

APPENDIX A

For the 18 test cases mentioned earlier in this report, the graphical results for the 60 mission cases are illustrated, continuing from the earlier presentation of these results in Figures 4.18 and 4.19. For the figures shown, 2 mission cases are presented on each figure, while all 18 test cases are shown on each figure. The "+" marks in the "F/W Ratio = 0" plane indicate the projections from the surfaces shown regarding each of the 18 test cases. Figures A.1 and A.2 are Figures 4.18 and 4.19 repeated.

In viewing these graphs, one should keep in mind that for every four graphs relating to cases of 1, 2, 3, and 4 thrusters being used, the values of Δv and mass flow rate are held constant. Within each group of four graphs, the parameter to watch is the F/W ratio, as the pinch current and specific impulse will not change among the four. If comparisons are made to observe how the F/W ratio and I_{sp} values vary for a set number of thrusters, then one would need to compare the captions under appropriate figures in order to choose the graphs with appropriate values of Δv and mass flow rate. For example, if one wishes to see how the F/W ratio varies with Δv for a 4-thruster system with a mass flow rate of 10 [kg/s], then the graphs needed for the comparison are Figures A.14, A.16, and A.18. It would be evident that moving from a Δv of 10 [km/s] to one of 40 [km/s] causes the F/W ratio to decrease from above 0.1 to below 0.02. The pinch current values for each of the 18 test cases in each graph remain unchanged, as pinch current is the differentiating characteristic of the test cases. Recall Figure 4.16 to see the assumed values of ion number density and axial velocity used to determine each of the 18 pinch currents used.

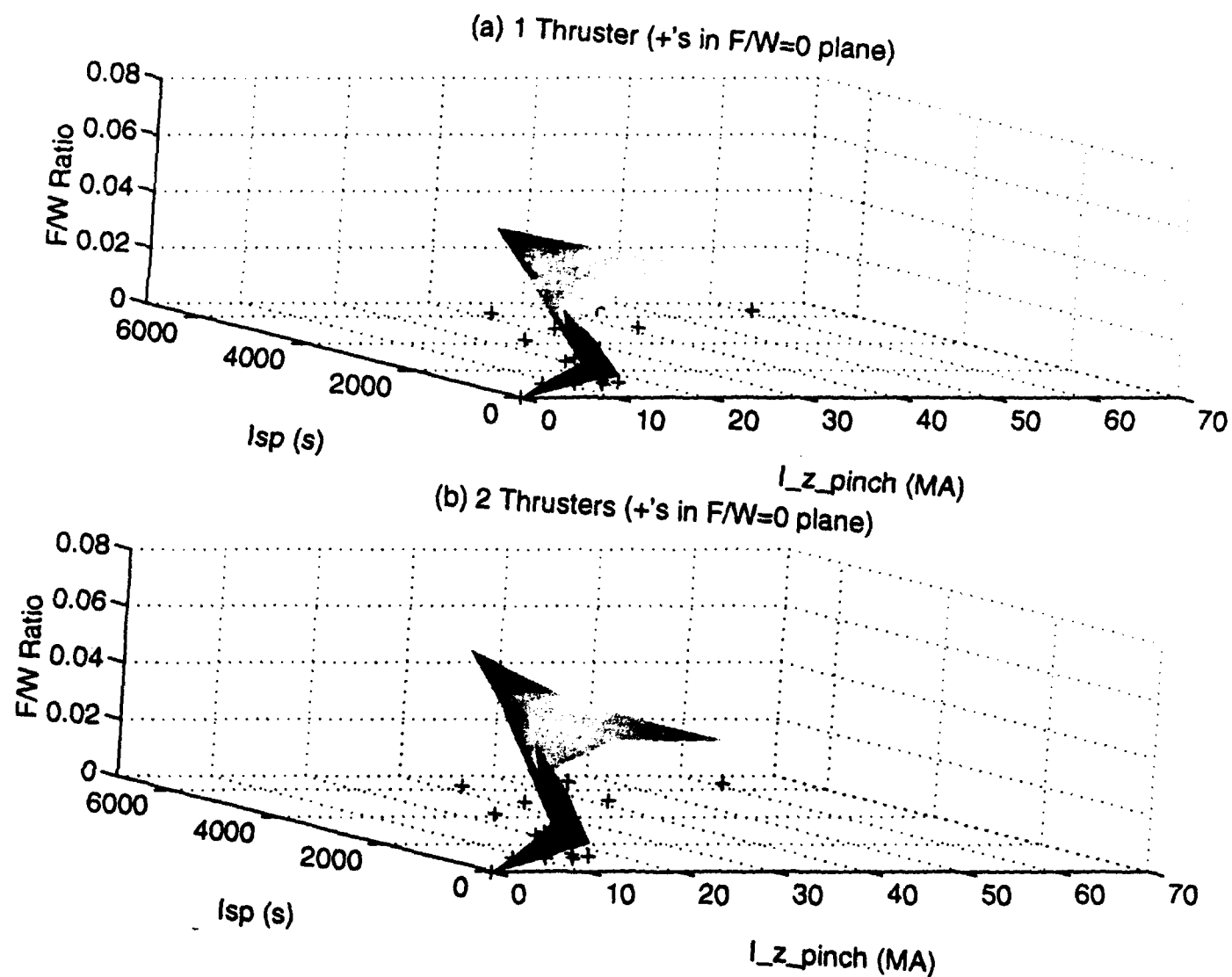


Figure A.1
Pinch Current, Specific Impulse, and F/W Ratio for Propellant Mass Flow Rate of 1.0 [kg/s] and $\Delta v = 10$ [km/s] with (a) 1 Thruster and (b) 2 Thrusters

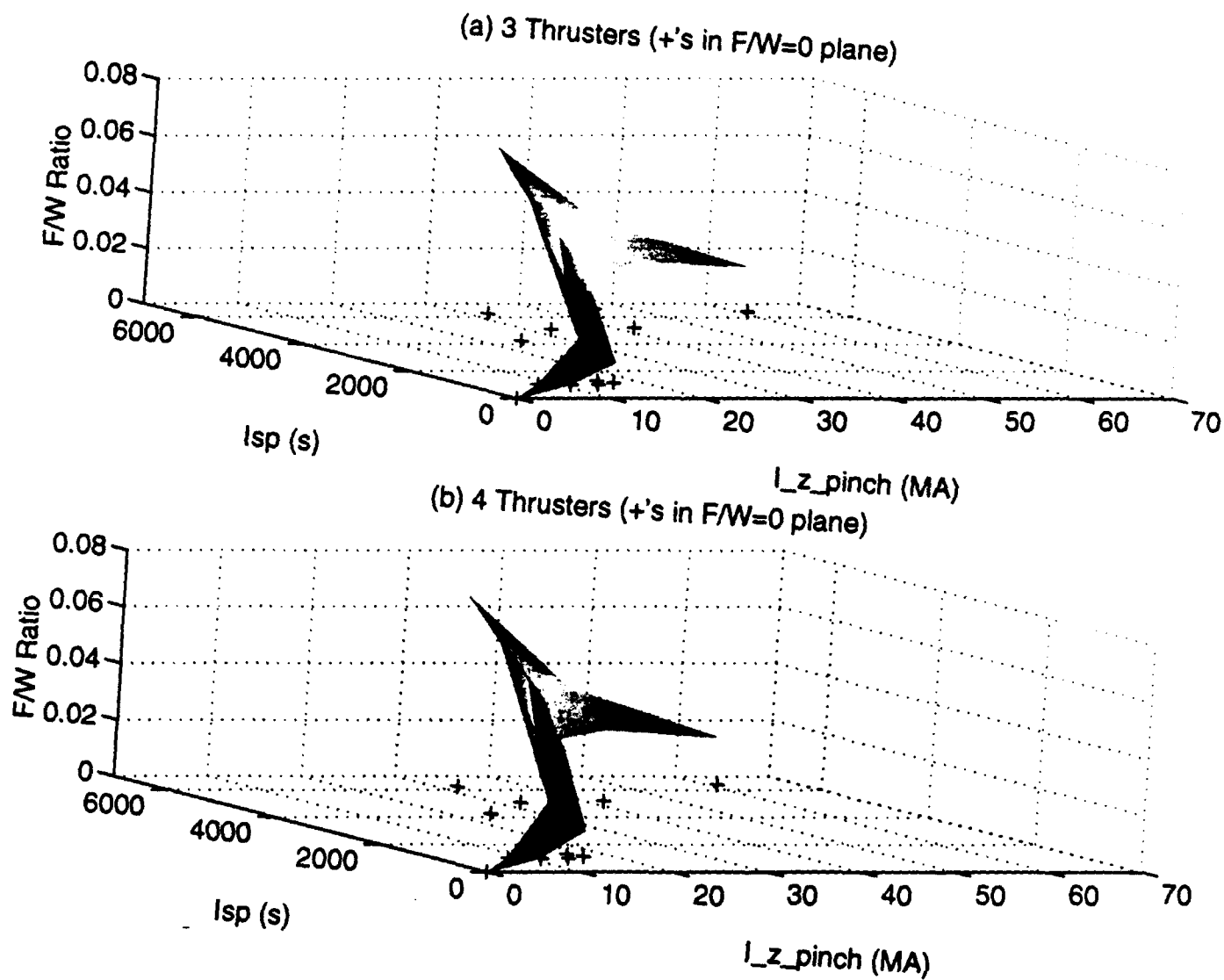


Figure A.2
Pinch Current, Specific Impulse, and F/W Ratio for Propellant Mass Flow Rate of 1.0 [kg/s] and $\Delta v = 10$ [km/s] with (a) 3 Thrusters and (b) 4 Thrusters

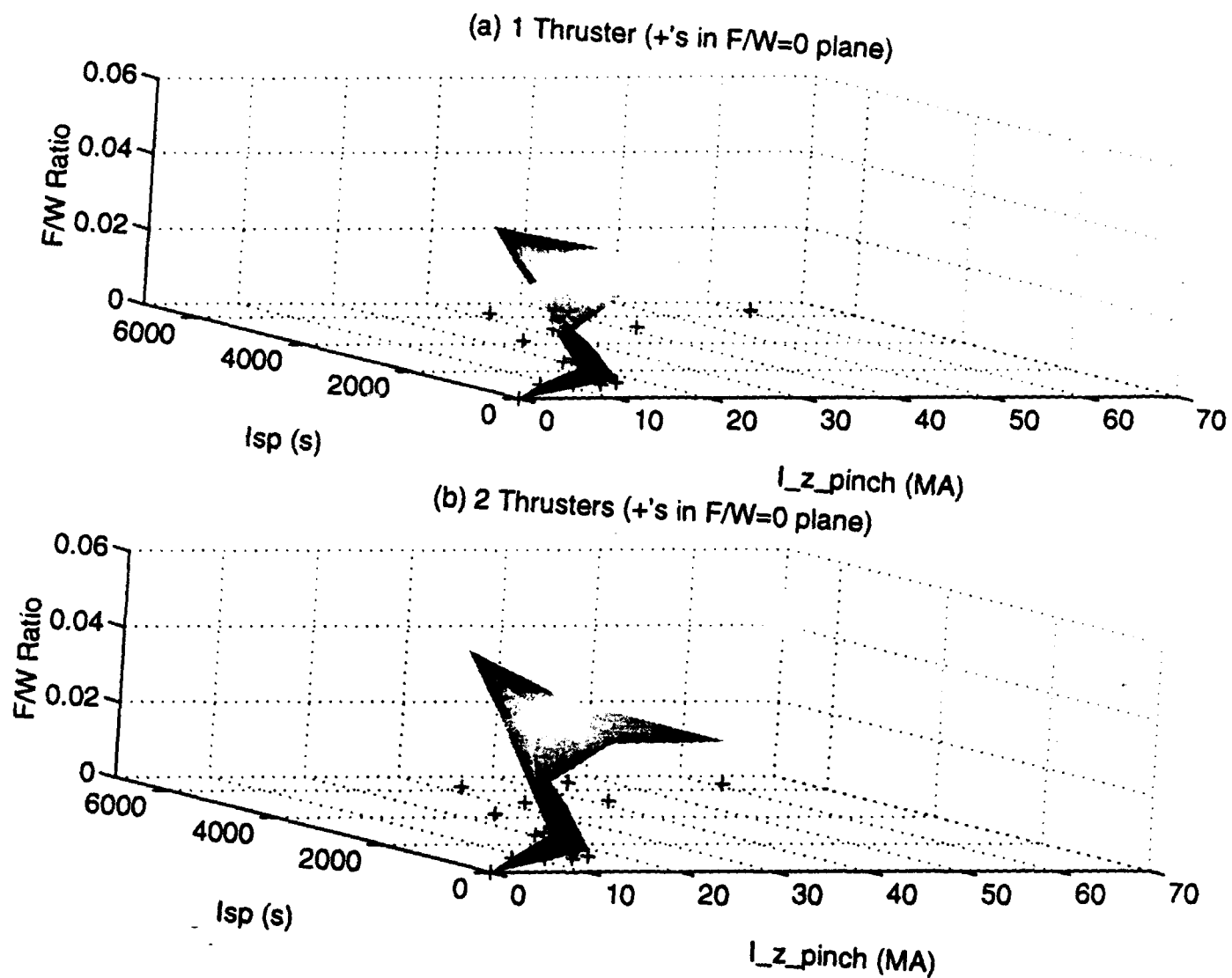


Figure A.3
Pinch Current, Specific Impulse, and F/W Ratio for Propellant Mass Flow Rate of 1.0 [kg/s] and $\Delta v = 20 \text{ [km/s]}$ with (a) 1 Thruster and (b) 2 Thrusters

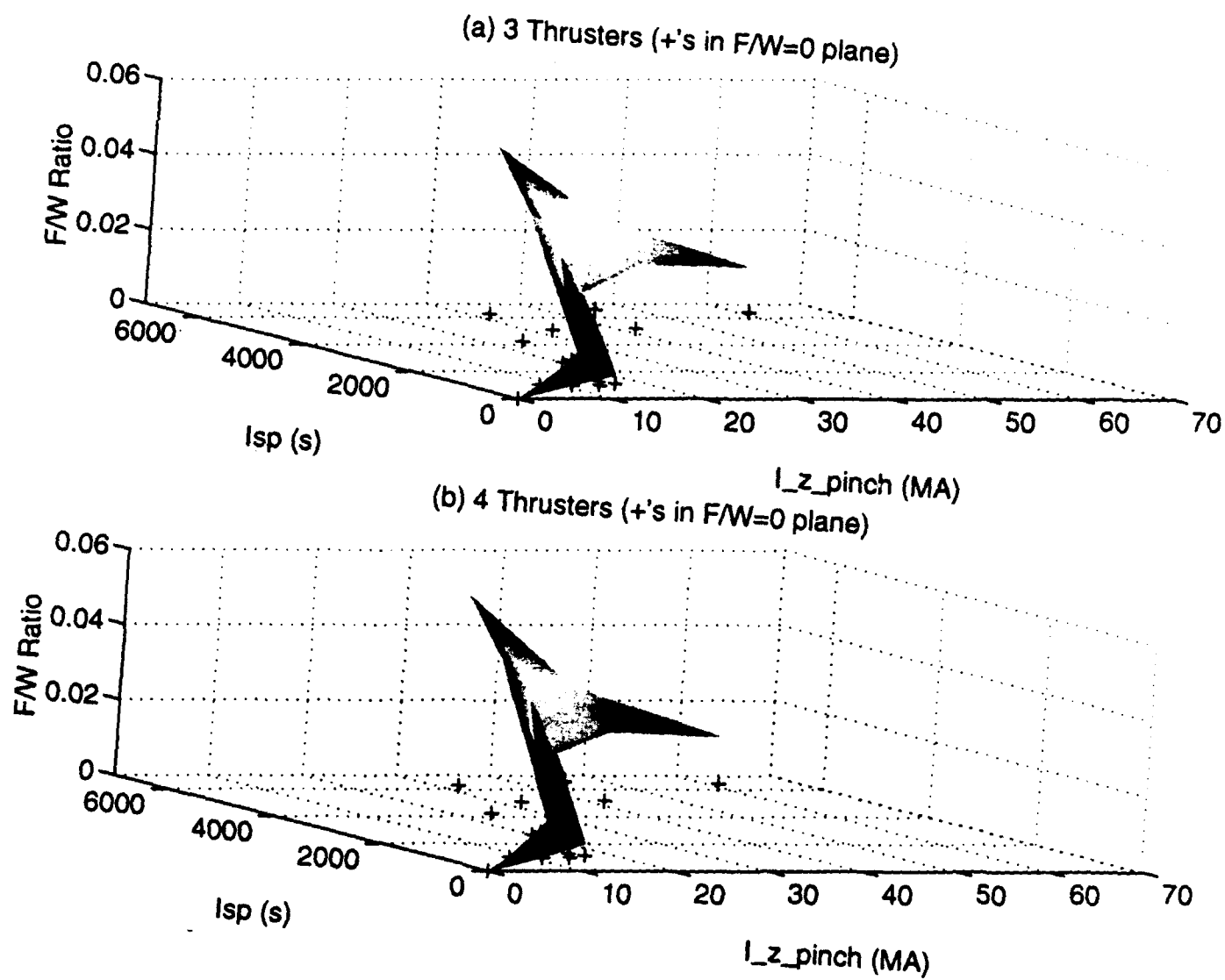


Figure A.4
Pinch Current, Specific Impulse, and F/W Ratio for Propellant Mass Flow Rate of 1.0 [kg/s] and $\Delta v = 20$ [km/s] with (a) 3 Thrusters and (b) 4 Thrusters

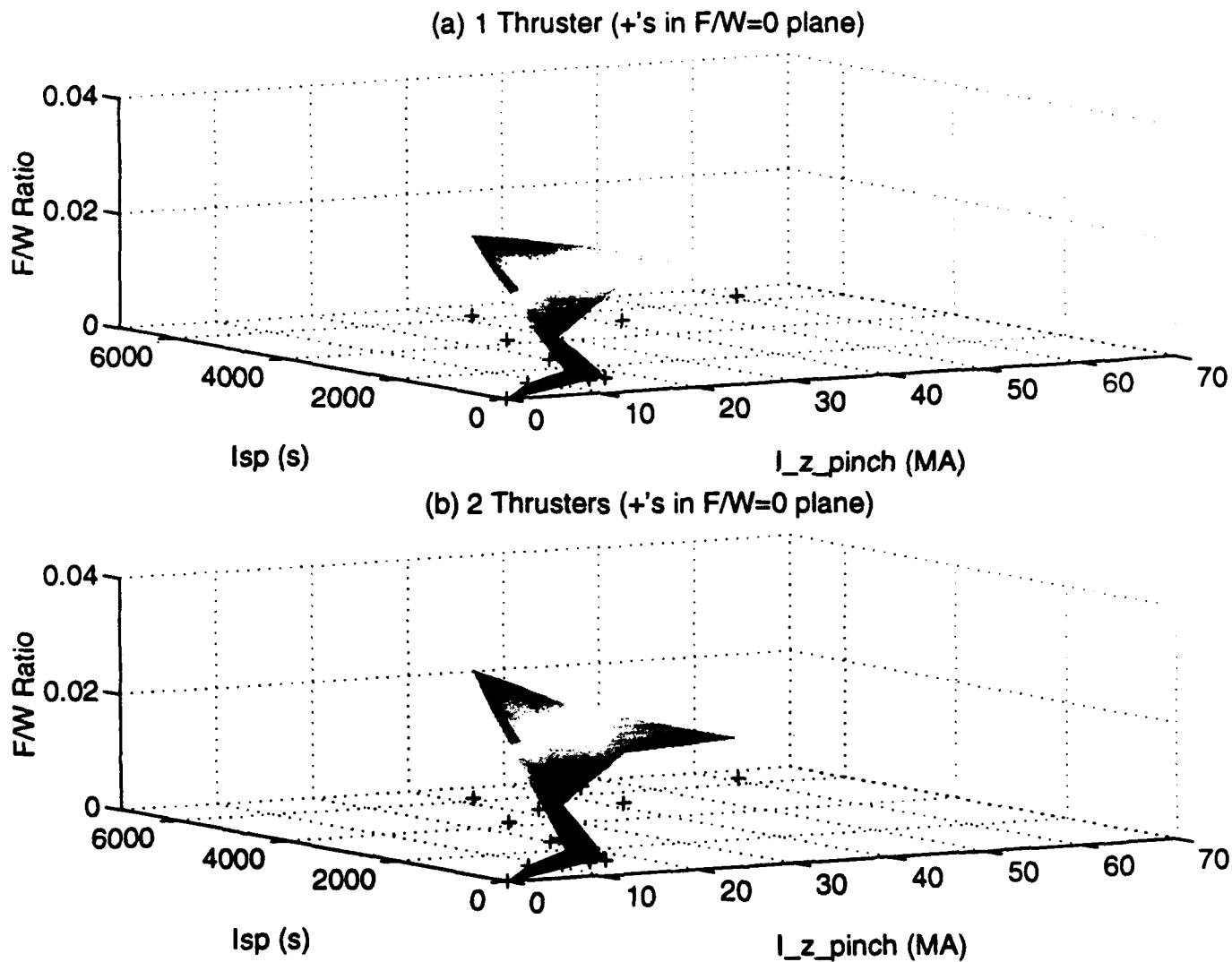


Figure A.5
Pinch Current, Specific Impulse, and F/W Ratio for Propellant Mass Flow Rate of 1.0 [kg/s] and $\Delta v = 40$ [km/s] with (a) 1 Thruster and (b) 2 Thrusters

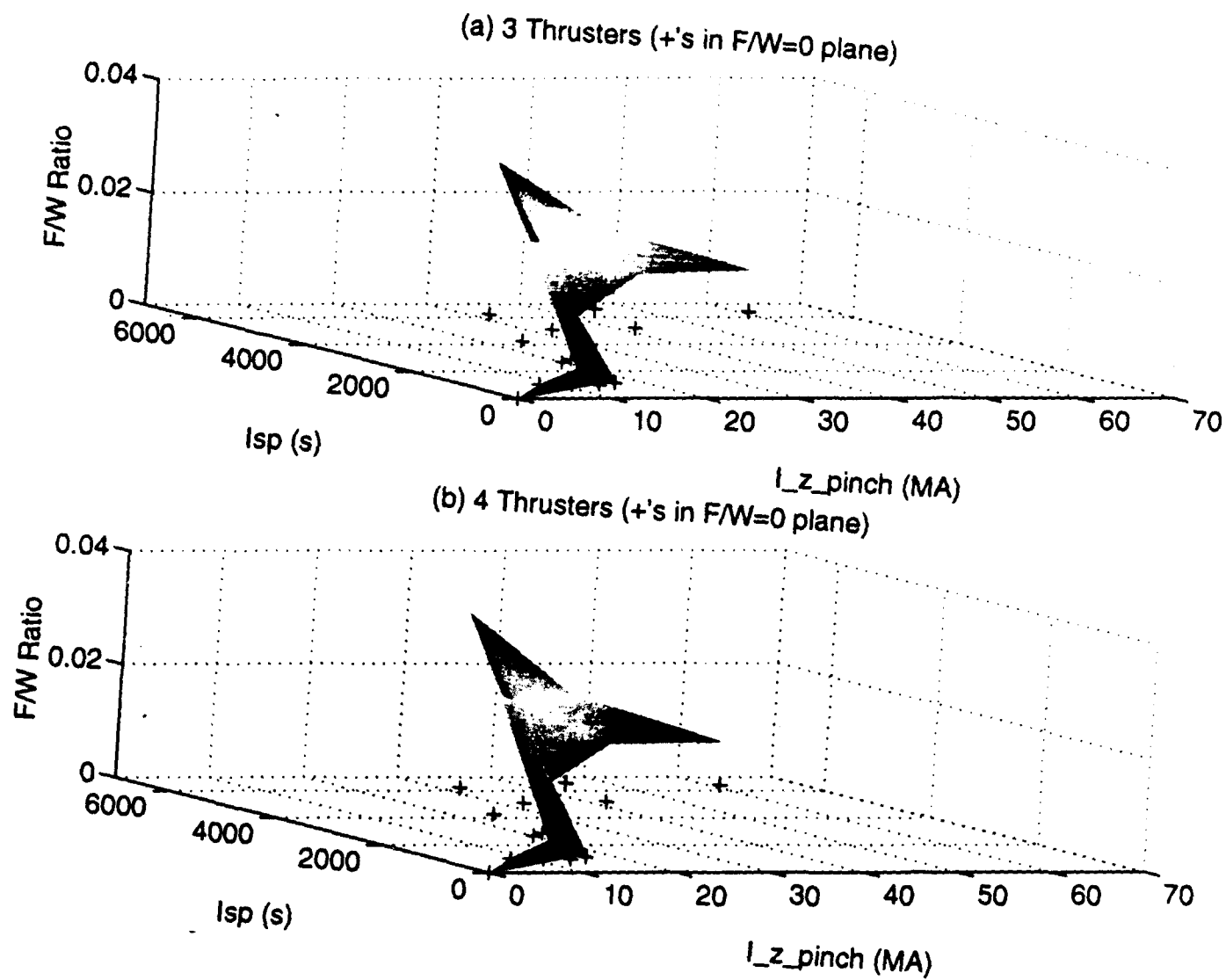


Figure A.6
Pinch Current, Specific Impulse, and F/W Ratio for Propellant Mass Flow Rate of 1.0 [kg/s] and $\Delta v = 40$ [km/s] with (a) 3 Thrusters and (b) 4 Thrusters

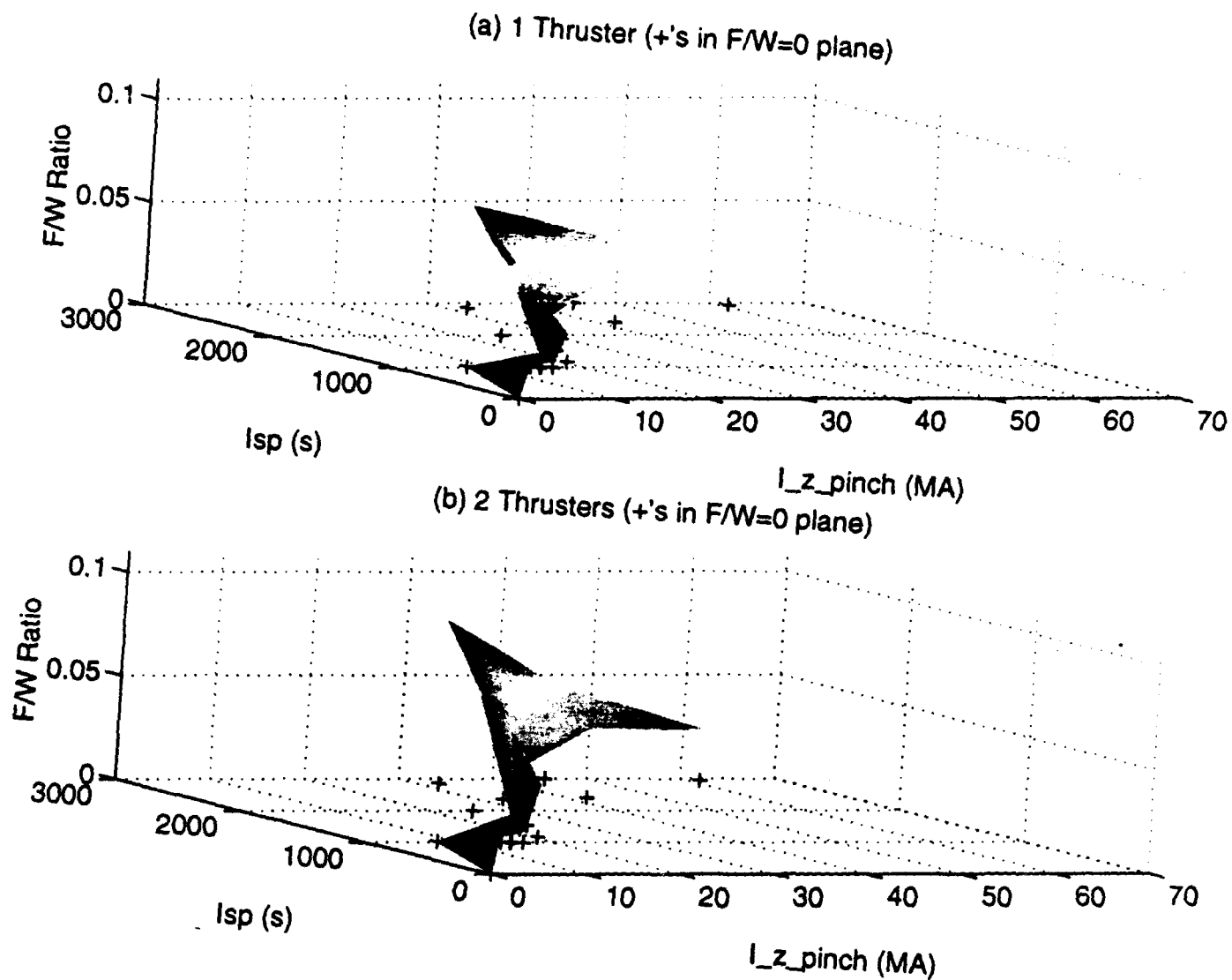


Figure A.7
Pinch Current, Specific Impulse, and F/W Ratio for Propellant Mass Flow Rate of 5.0 [kg/s] and $\Delta v = 10$ [km/s] with (a) 1 Thruster and (b) 2 Thrusters

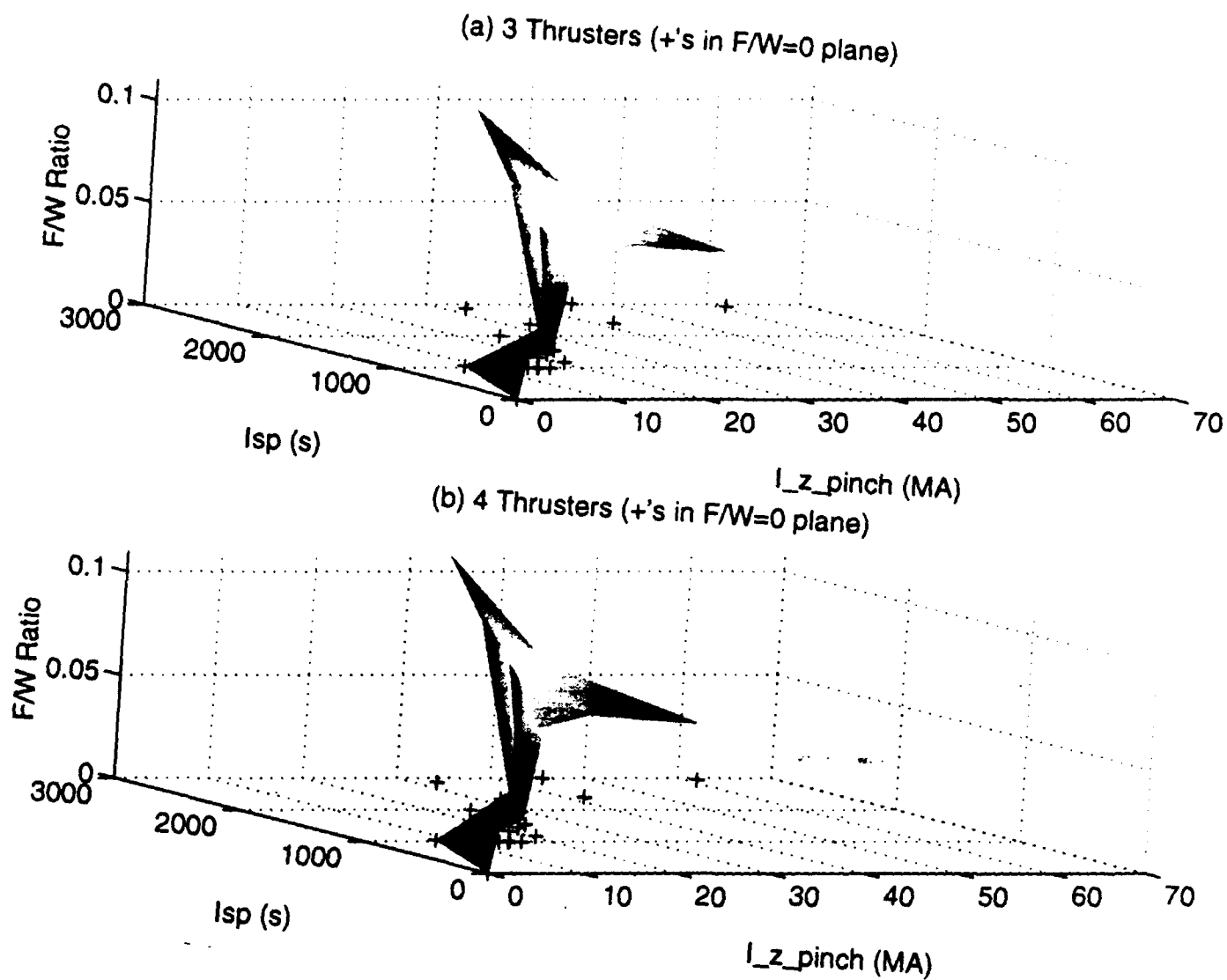


Figure A.8
Pinch Current, Specific Impulse, and F/W Ratio for Propellant Mass Flow Rate of 5.0 [kg/s] and $\Delta v = 10$ [km/s] with (a) 3 Thrusters and (b) 4 Thrusters

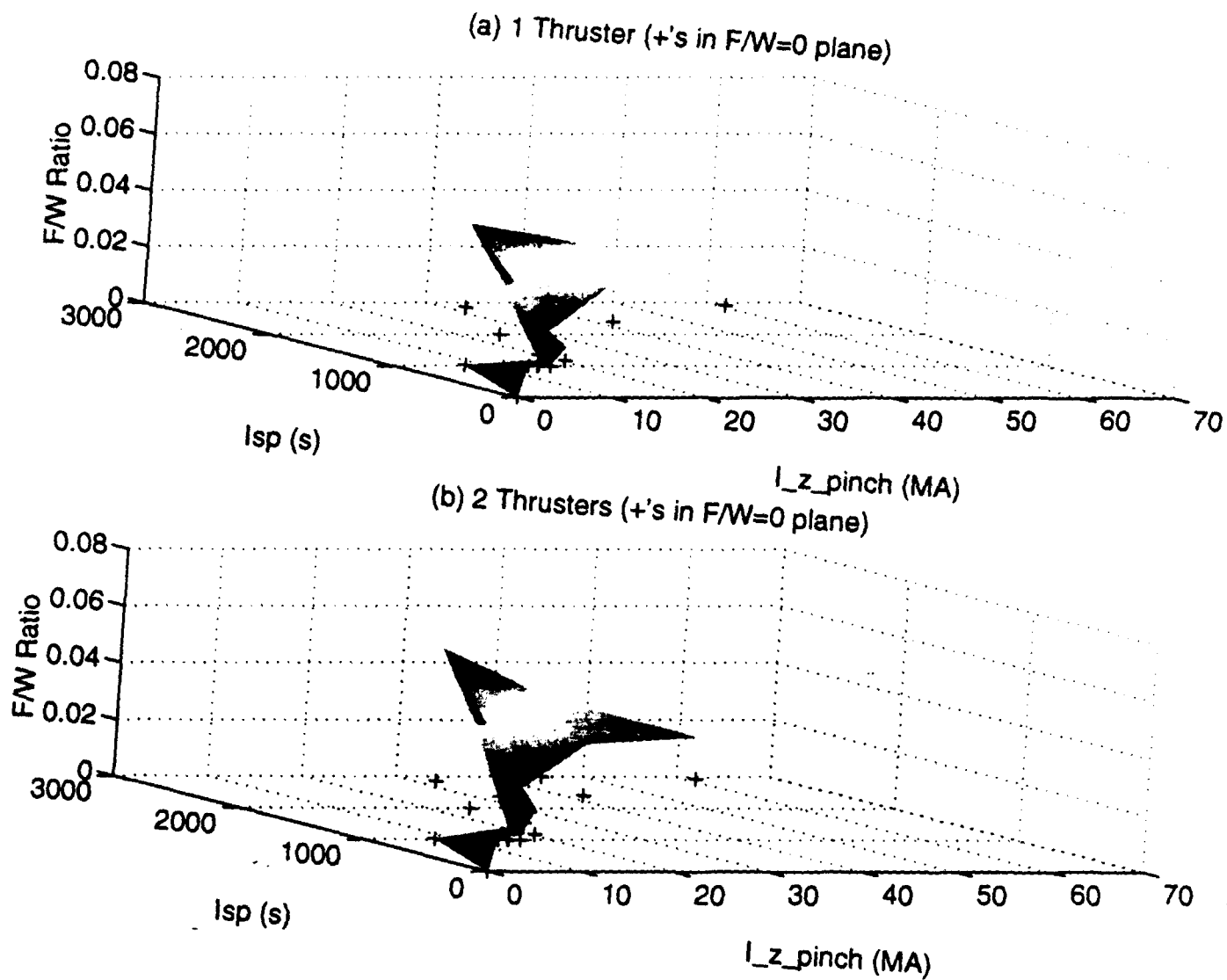


Figure A.9
Pinch Current, Specific Impulse, and F/W Ratio for Propellant Mass Flow Rate of 5.0 [kg/s] and $\Delta v = 20 \text{ [km/s]}$ with (a) 1 Thruster and (b) 2 Thrusters

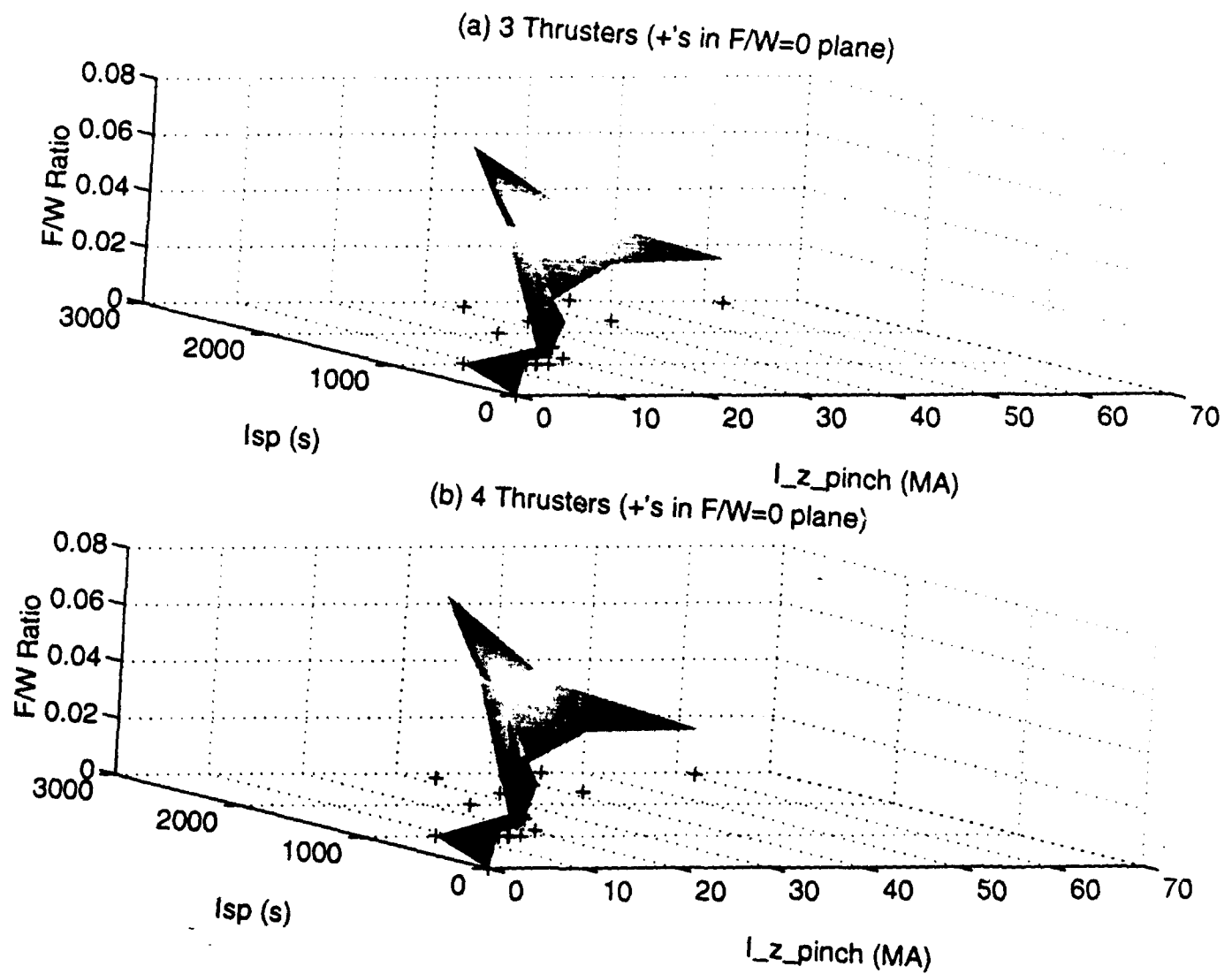


Figure A.10
Pinch Current, Specific Impulse, and F/W Ratio for Propellant Mass Flow Rate of 5.0 [kg/s] and $\Delta v = 20$ [km/s] with (a) 3 Thrusters and (b) 4 Thrusters

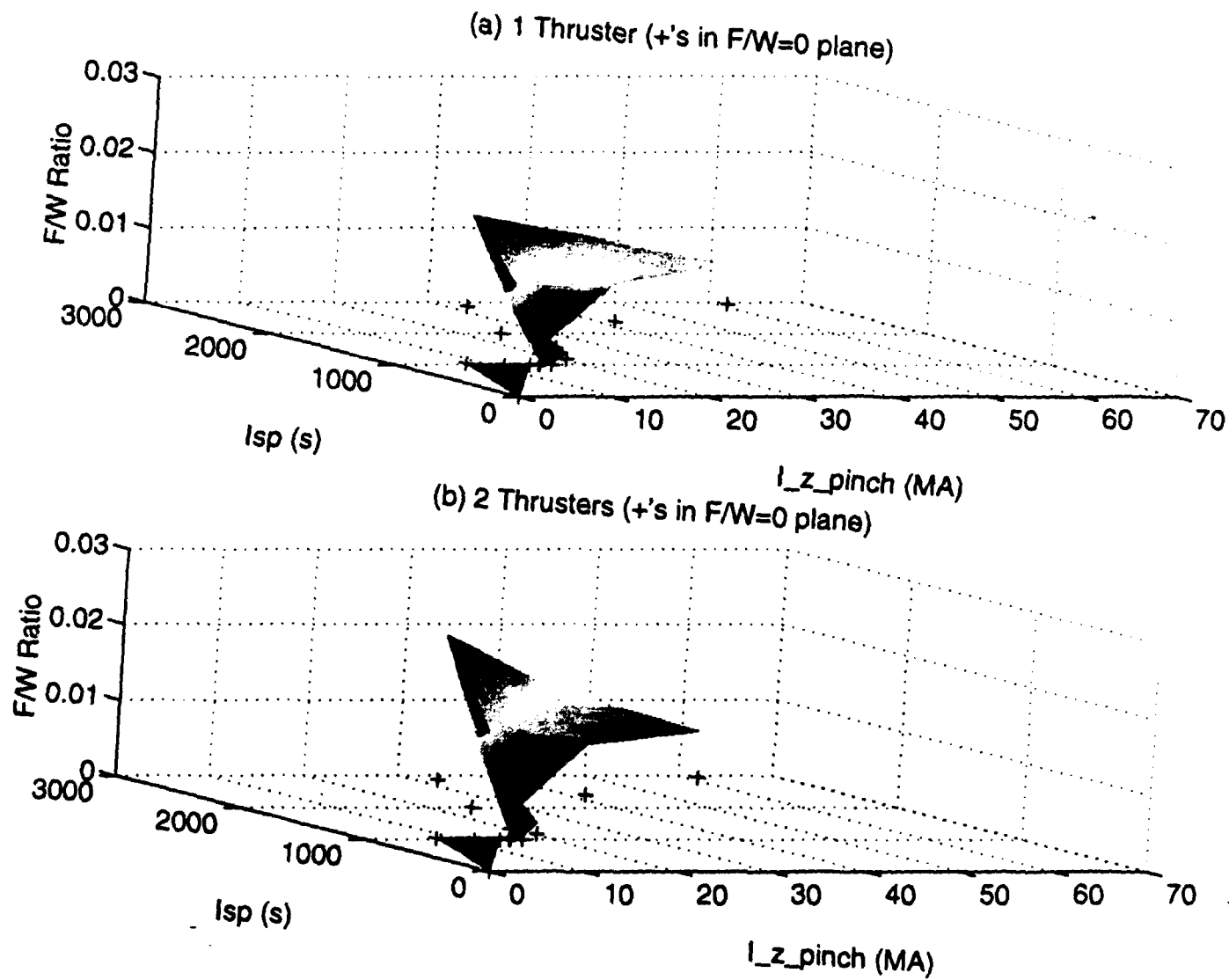


Figure A.11
Pinch Current, Specific Impulse, and F/W Ratio for Propellant Mass Flow Rate of 5.0 [kg/s] and $\Delta v = 40$ [km/s] with (a) 1 Thruster and (b) 2 Thrusters

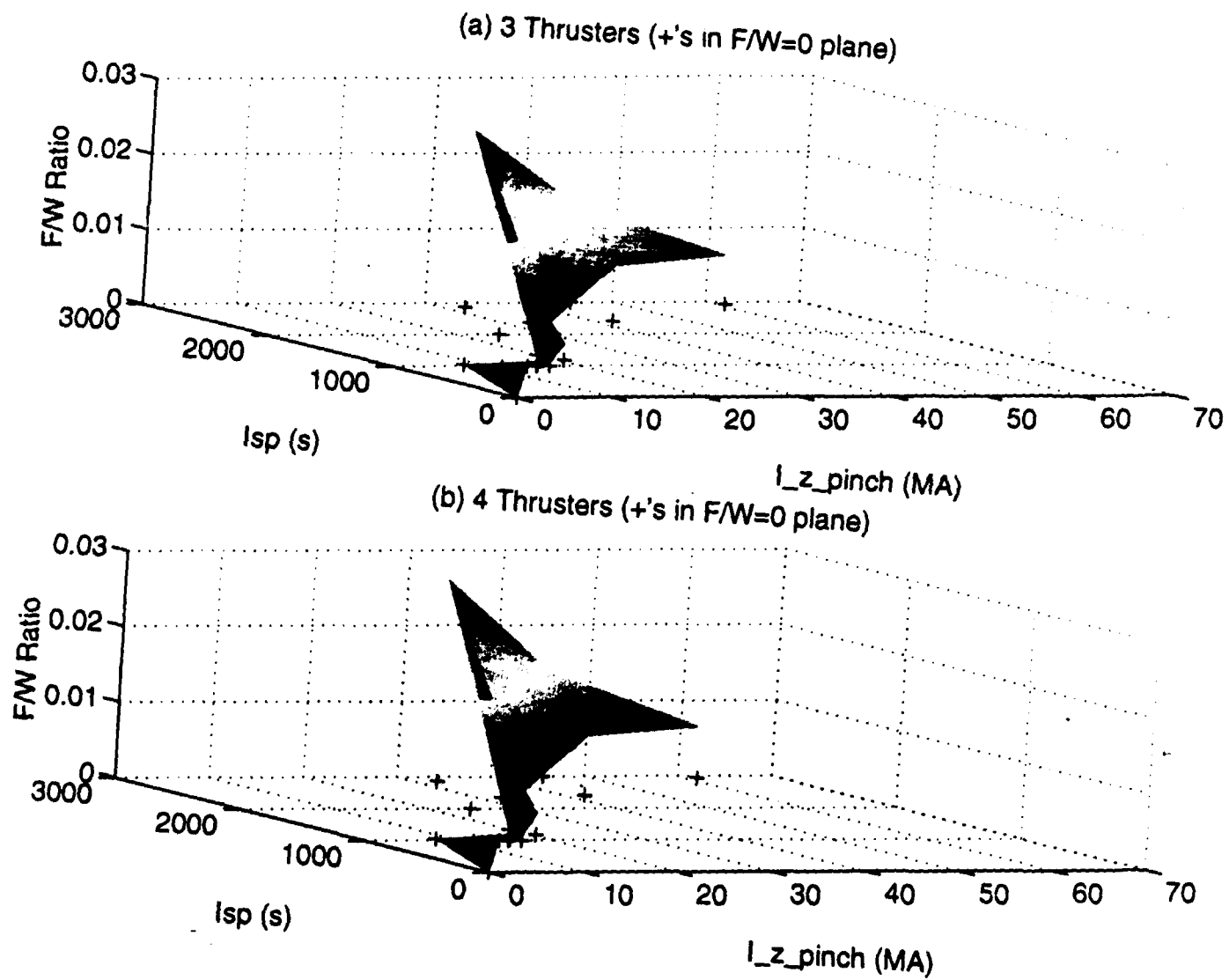


Figure A.12
Pinch Current, Specific Impulse, and F/W Ratio for Propellant Mass Flow Rate of 5.0 [kg/s] and $\Delta v = 40$ [km/s] with (a) 3 Thrusters and (b) 4 Thrusters

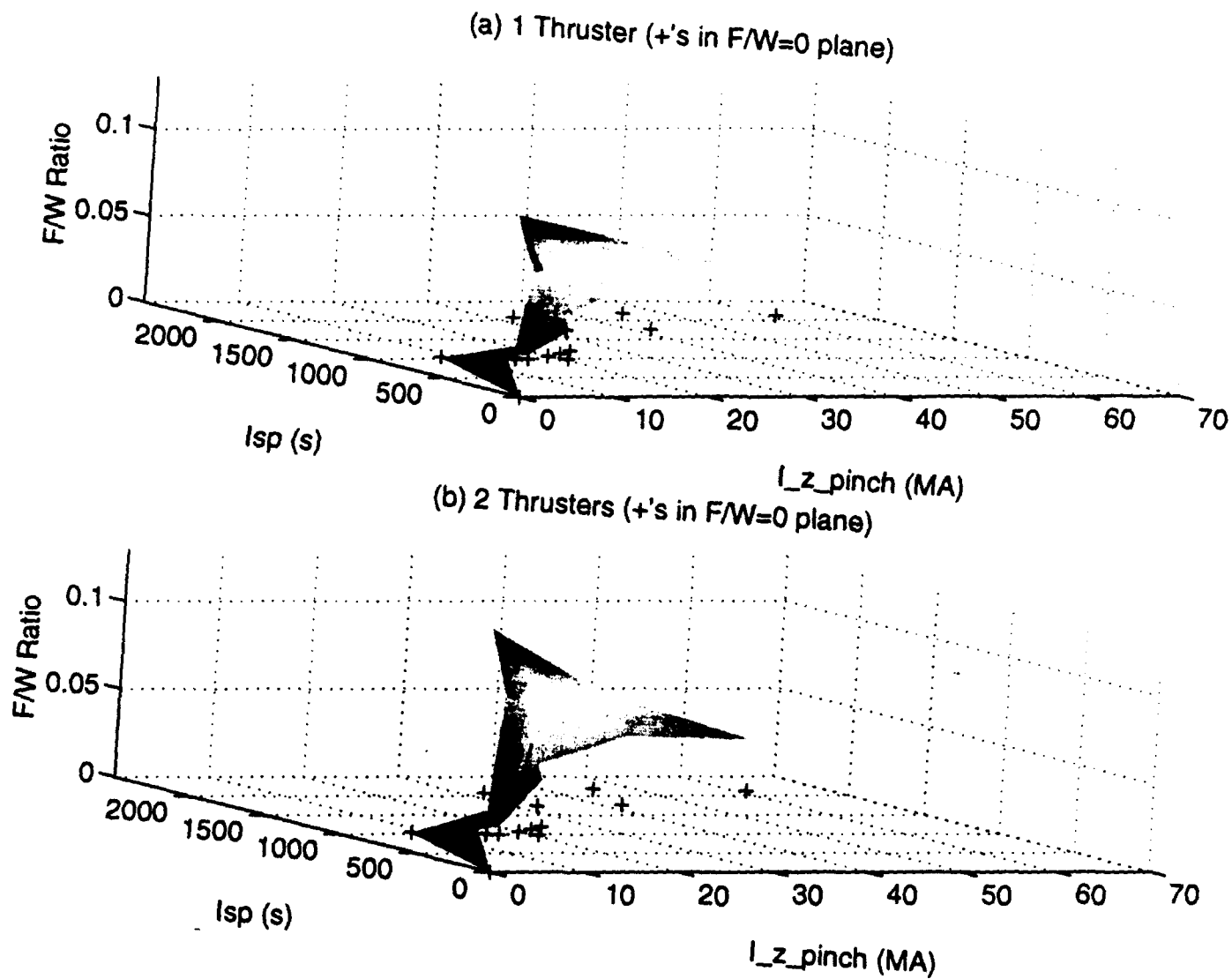


Figure A.13
Pinch Current, Specific Impulse, and F/W Ratio for Propellant Mass Flow Rate of 10.0 [kg/s] and $\Delta v = 10$ [km/s] with (a) 1 Thruster and (b) 2 Thrusters

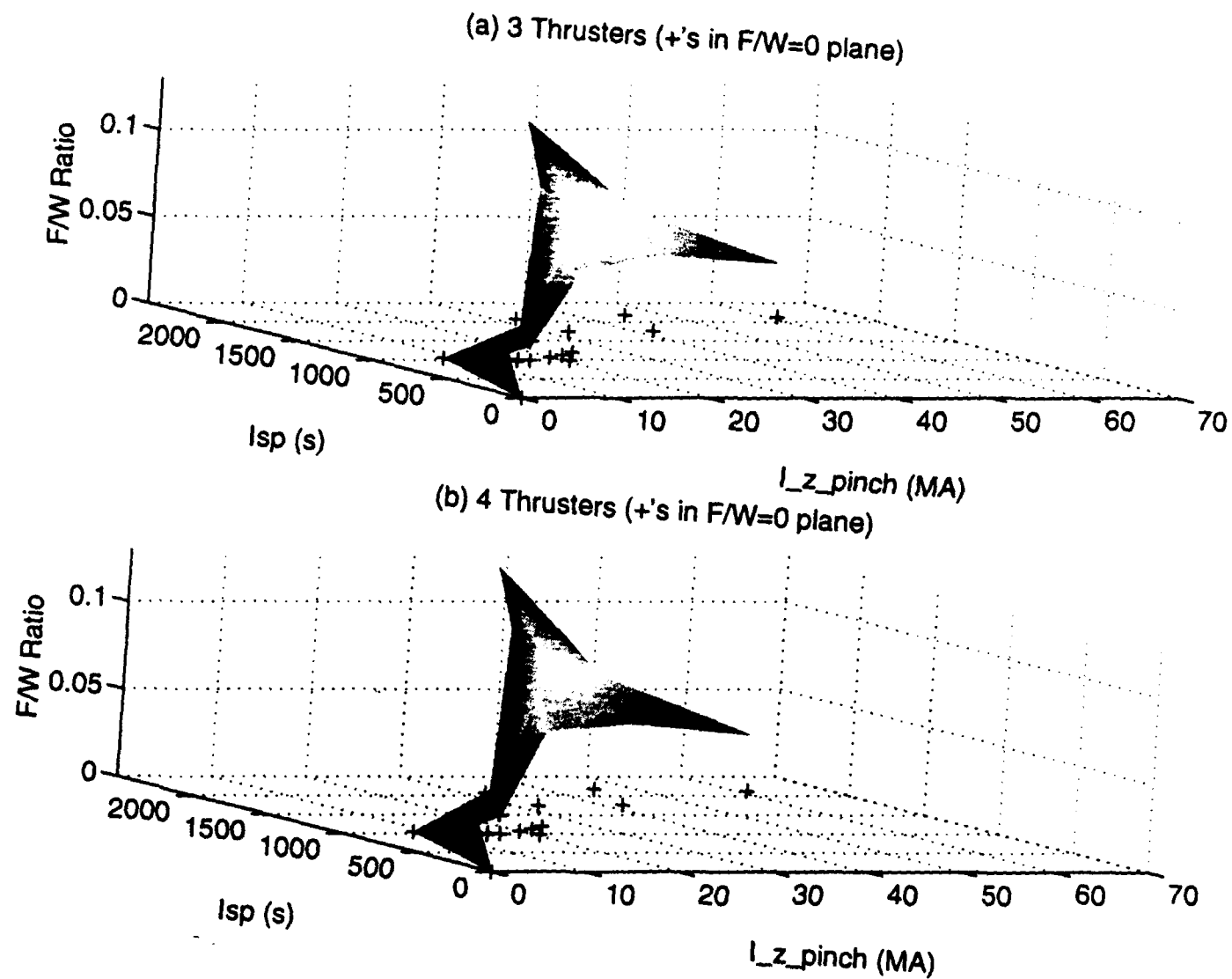


Figure A.14
Pinch Current, Specific Impulse, and F/W Ratio for Propellant Mass Flow Rate of 10.0 [kg/s] and $\Delta v = 10$ [km/s] with (a) 3 Thrusters and (b) 4 Thrusters

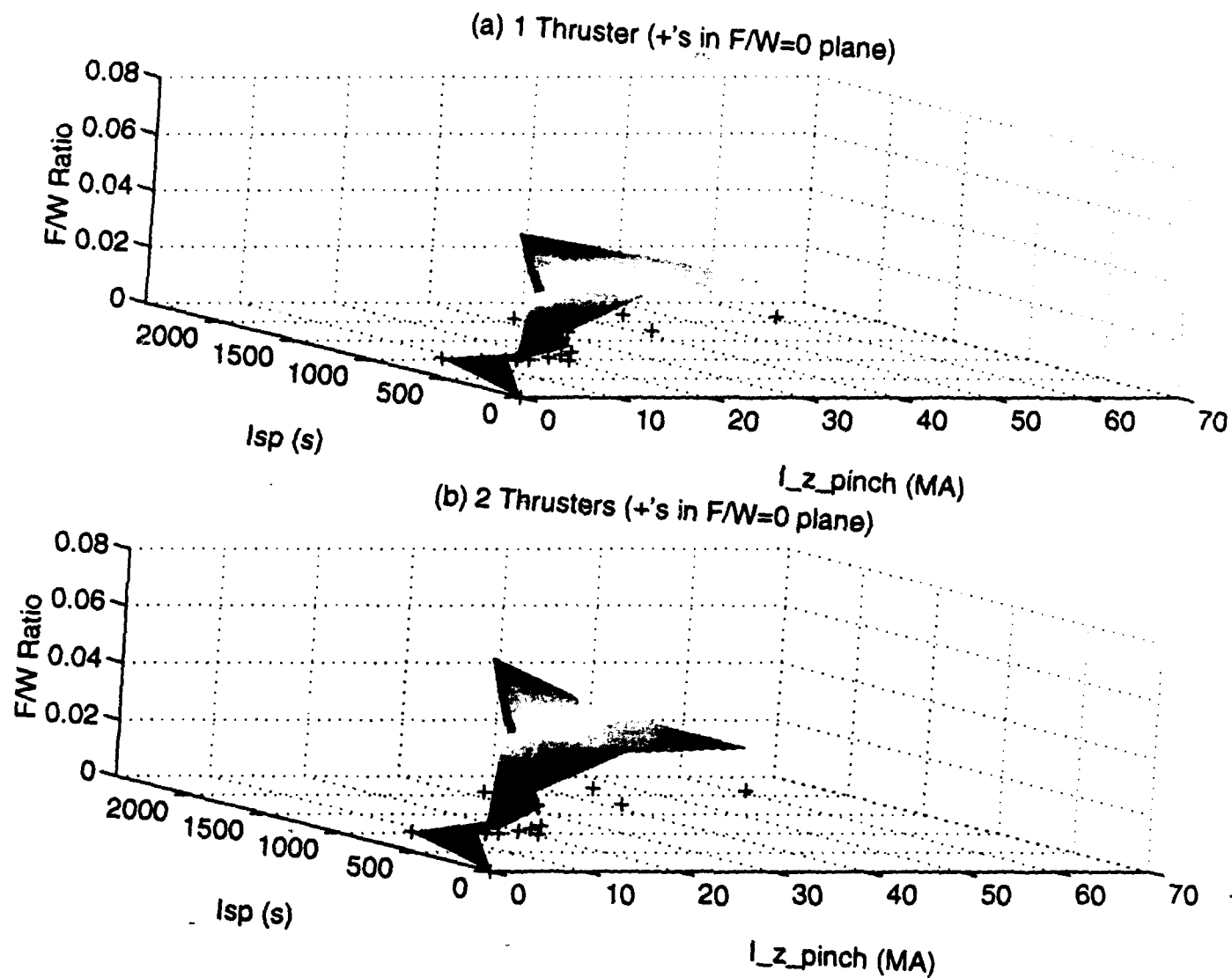


Figure A.15
 Pinch Current, Specific Impulse, and F/W Ratio for Propellant Mass Flow Rate of 10.0 [kg/s] and $\Delta v = 20$ [km/s] with Thruster and (b) 2 Thrusters

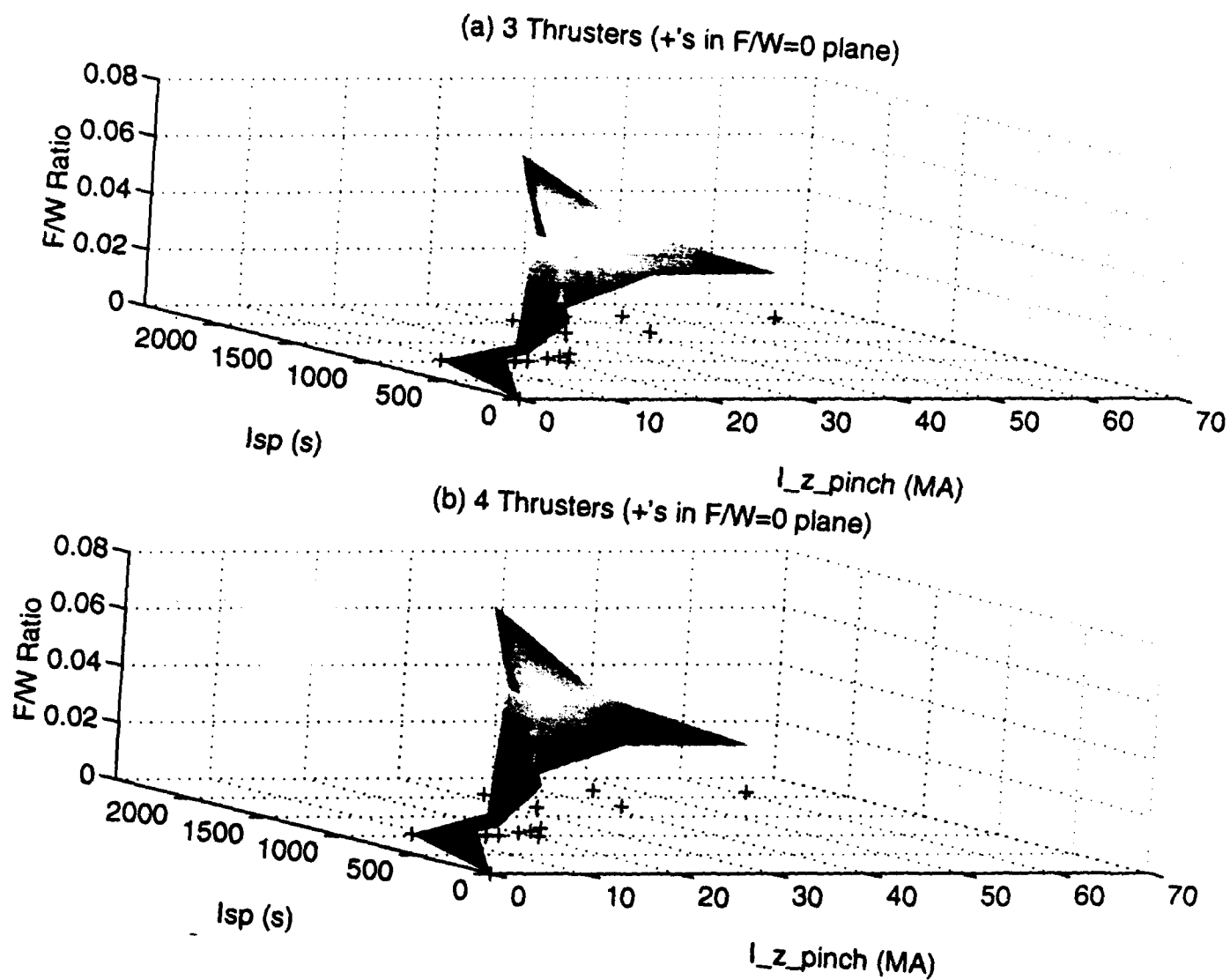


Figure A.16
Pinch Current, Specific Impulse, and F/W Ratio for Propellant Mass Flow Rate of 10.0 [kg/s] and $\Delta v = 20$ [km/s] with (a) 3 Thrusters and (b) 4 Thrusters

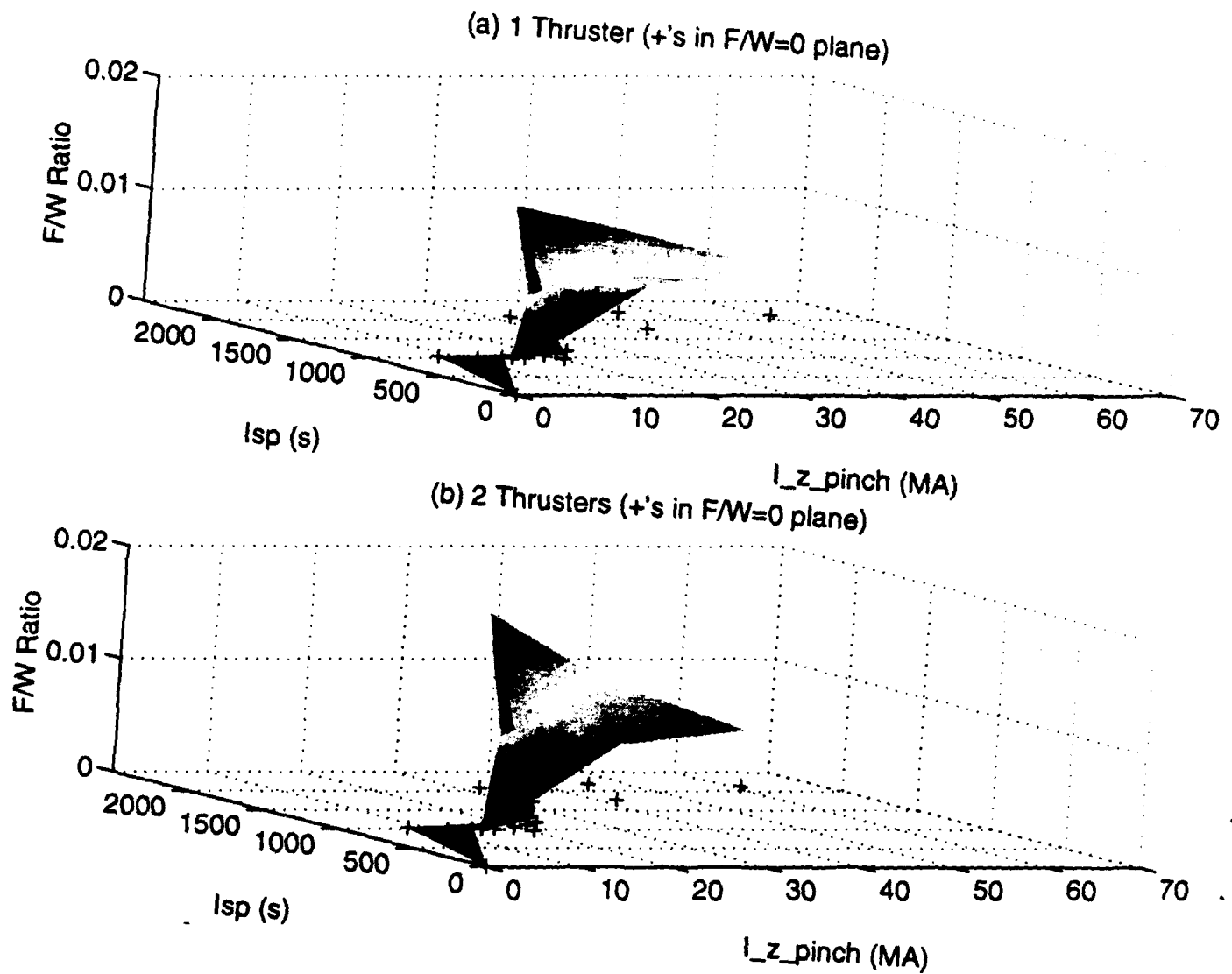


Figure A.17
Pinch Current, Specific Impulse, and F/W Ratio for Propellant Mass Flow Rate of 10.0 [kg/s] and $\Delta v = 40$ [km/s] with (a) 1 Thruster and (b) 2 Thrusters

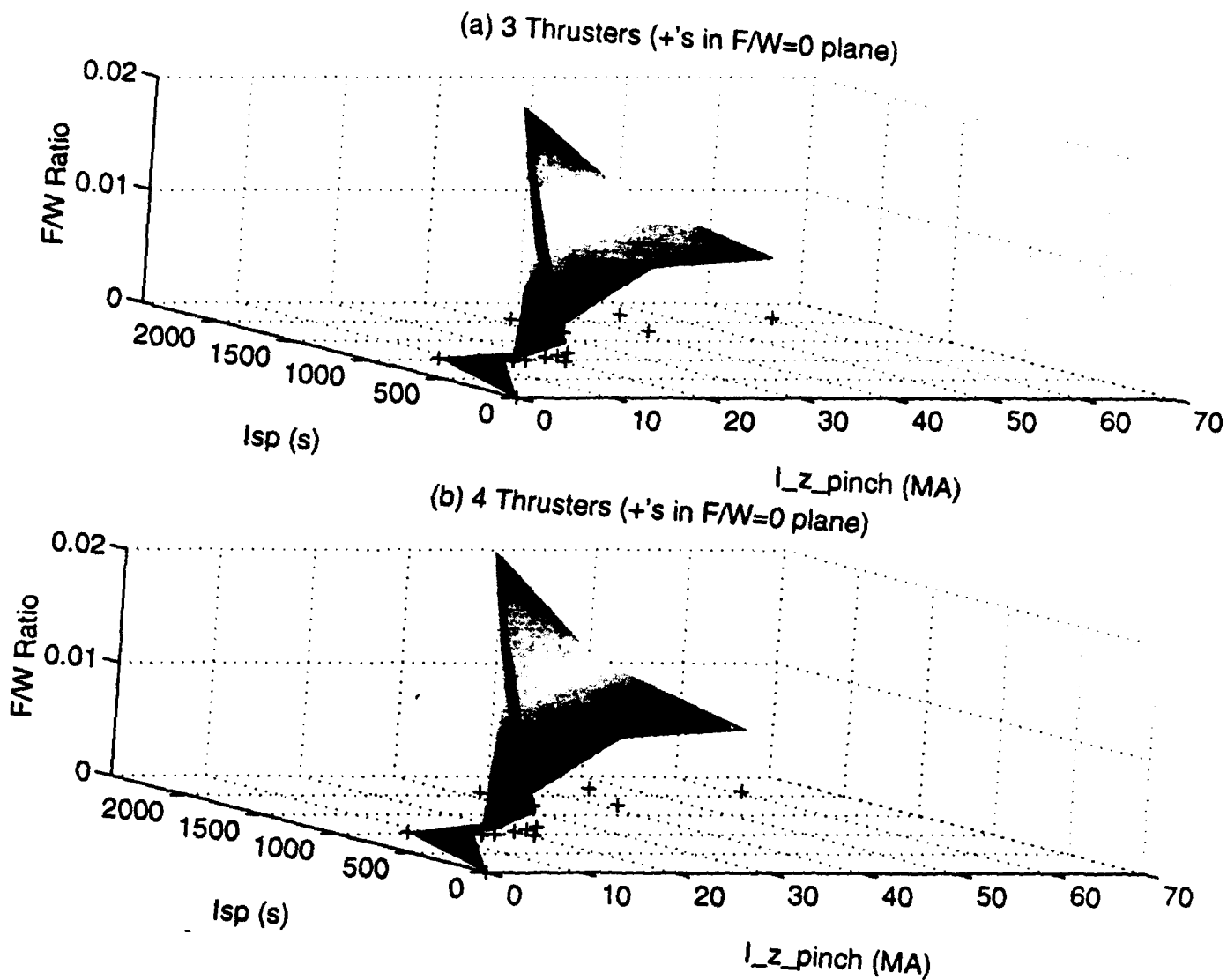


Figure A.18
Pinch Current, Specific Impulse, and F/W Ratio for Propellant Mass Flow Rate of 10.0 [kg/s] and $\Delta v = 40$ [km/s] with (a) 3 Thrusters and (b) 4 Thrusters

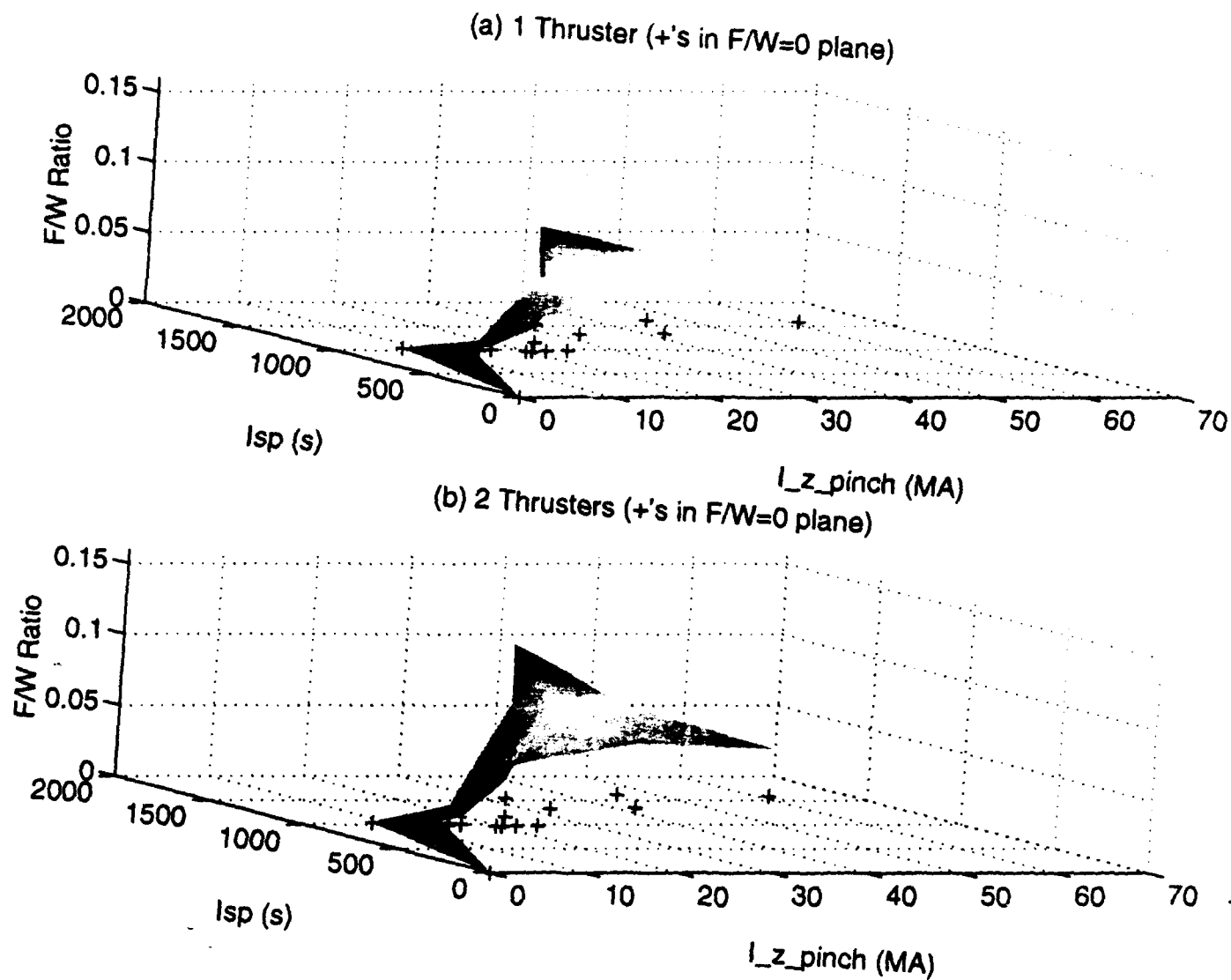


Figure A.19
Pinch Current, Specific Impulse, and F/W Ratio for Propellant Mass Flow Rate of 20.0 [kg/s] and $\Delta v = 10$ [km/s] with (a) 1 Thruster and (b) 2 Thrusters

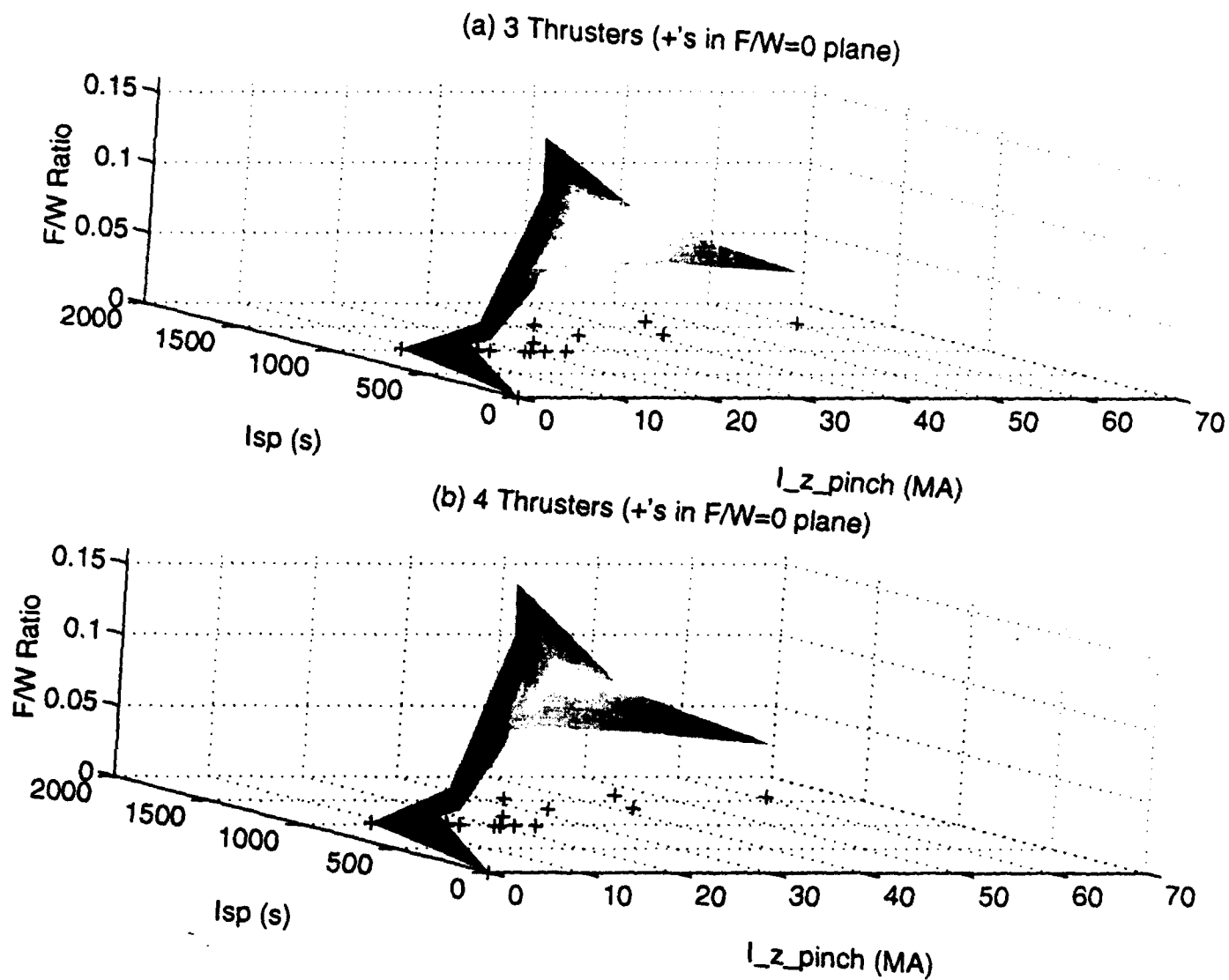


Figure A.20
Pinch Current, Specific Impulse, and F/W Ratio for Propellant Mass Flow Rate of 20.0 [kg/s] and $\Delta v = 10$ [km/s] with (a) 3 Thrusters and (b) 4 Thrusters

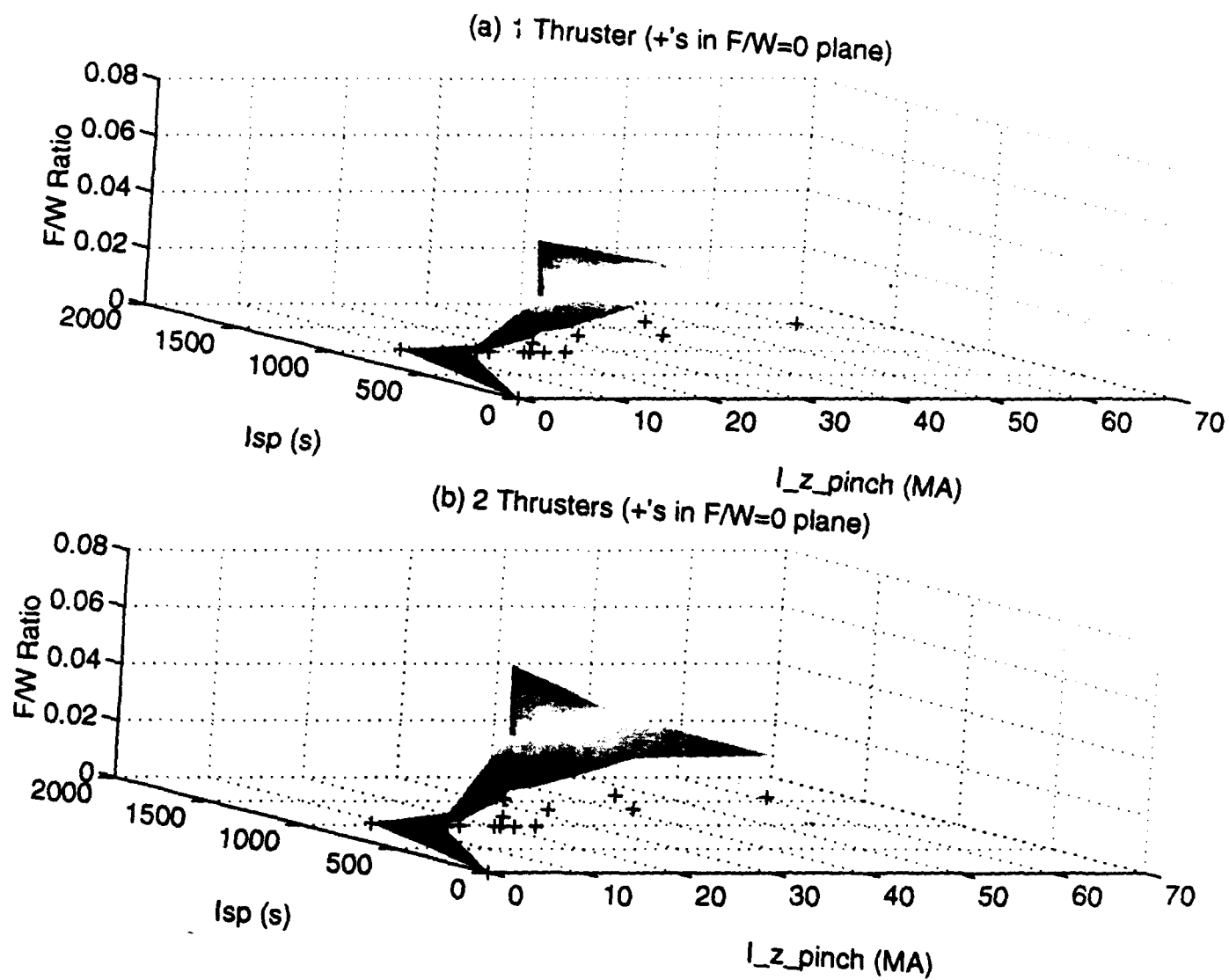


Figure A.21
Pinch Current, Specific Impulse, and F/W Ratio for Propellant Mass Flow Rate of 20.0 [kg/s] and $\Delta v = 20$ [km/s] with (a) 1 Thruster and (b) 2 Thrusters

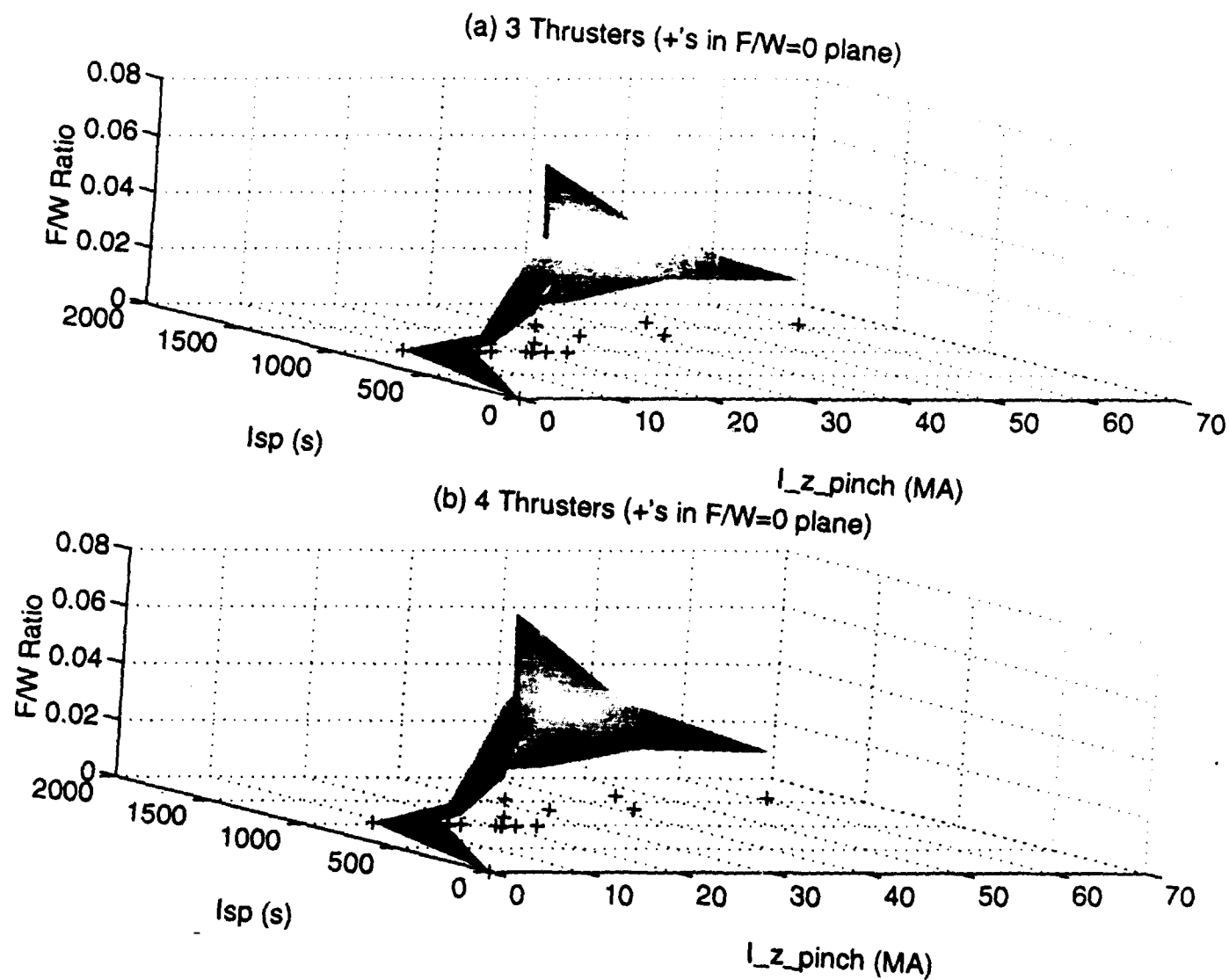


Figure A.22
Pinch Current, Specific Impulse, and F/W Ratio for Propellant Mass Flow Rate of 20.0 [kg/s] and $\Delta v = 20$ [km/s] with (a) 3 Thrusters and (b) 4 Thrusters

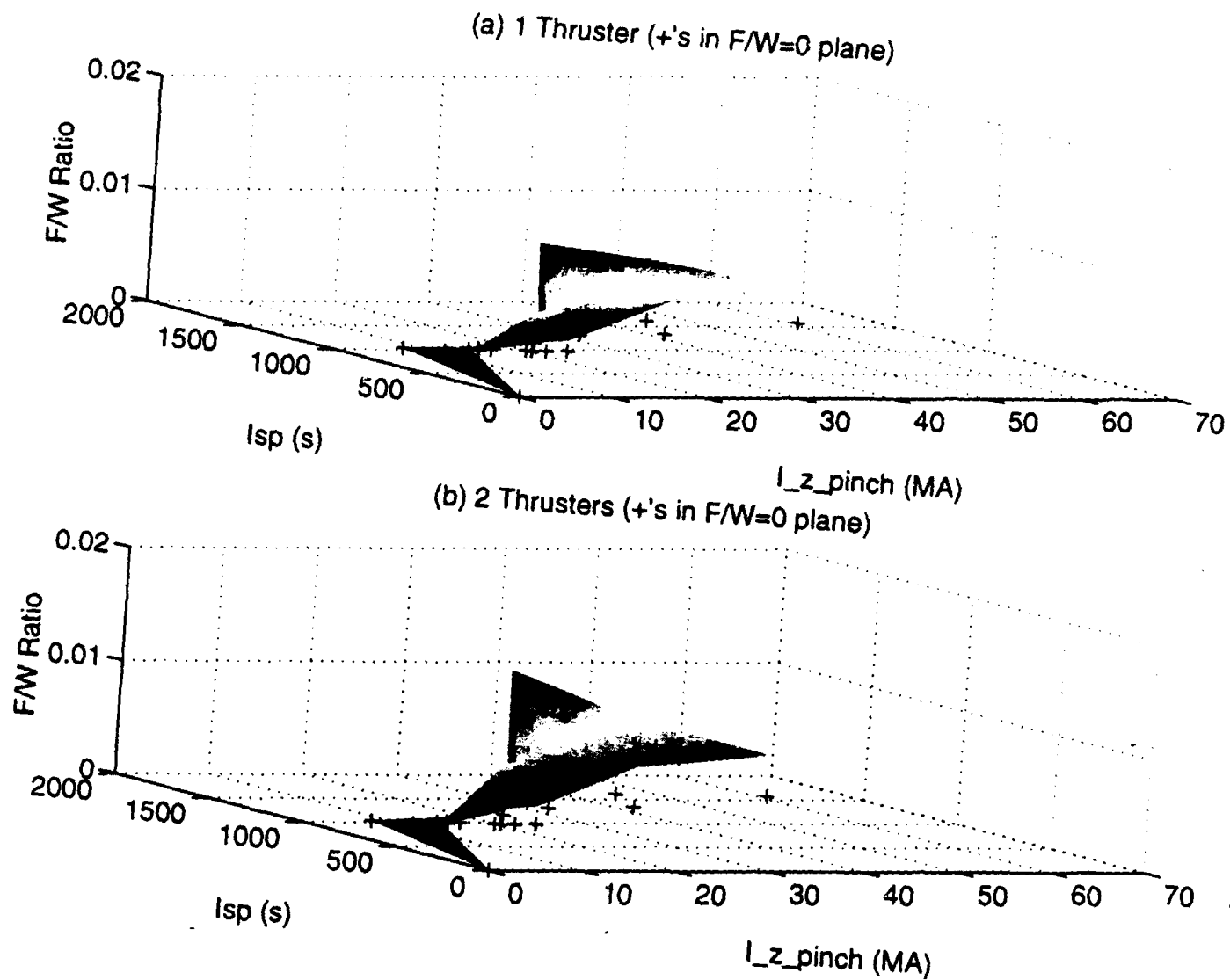


Figure A.23
Pinch Current, Specific Impulse, and F/W Ratio for Propellant Mass Flow Rate of 20.0 [kg/s] and $\Delta v = 40$ [km/s] with (a) 1 Thruster and (b) 2 Thrusters

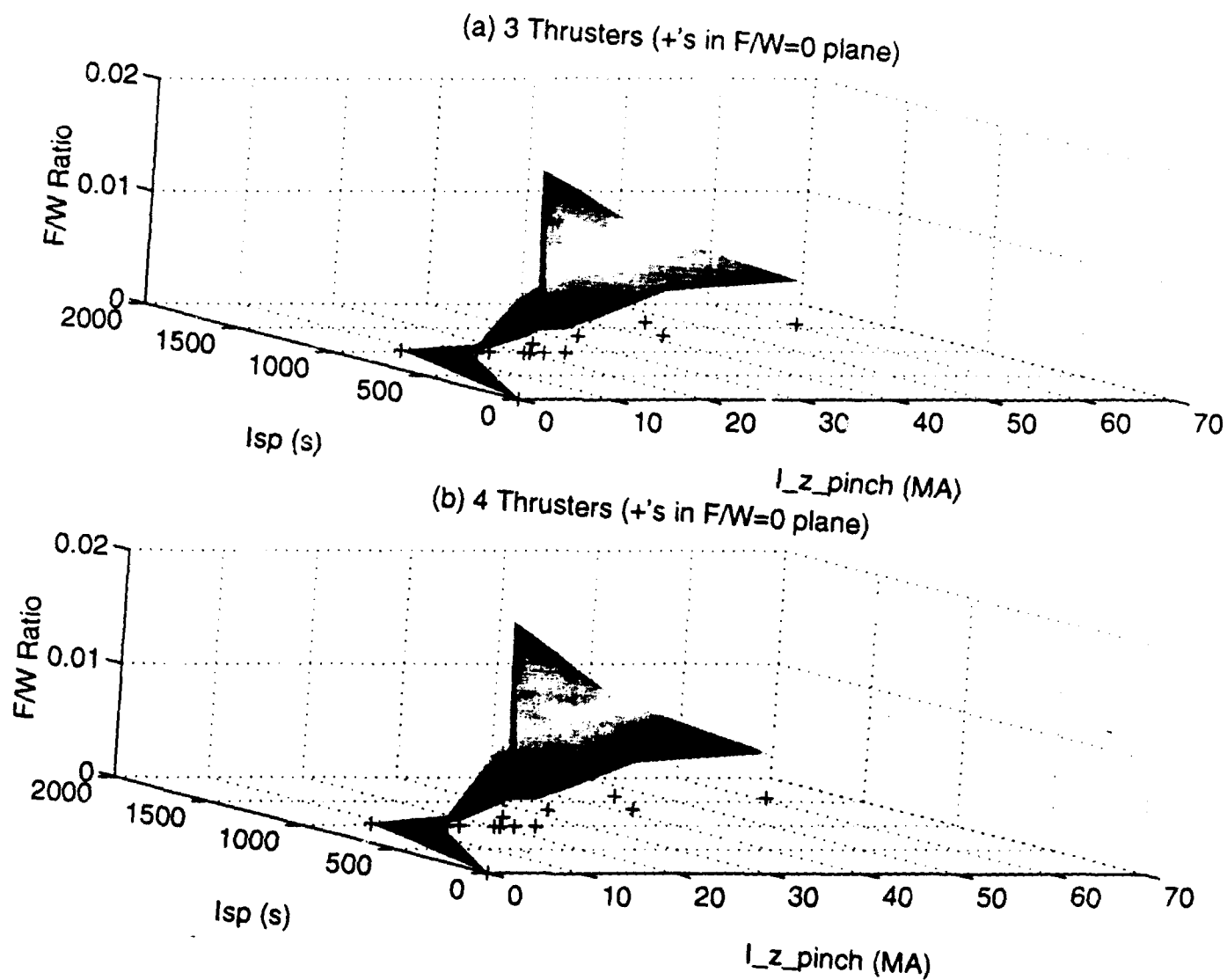


Figure A.24
Pinch Current, Specific Impulse, and F/W Ratio for Propellant Mass Flow Rate of 20.0 [kg/s] and $\Delta v = 40$ [km/s] with (a) 3 Thrusters and (b) 4 Thrusters

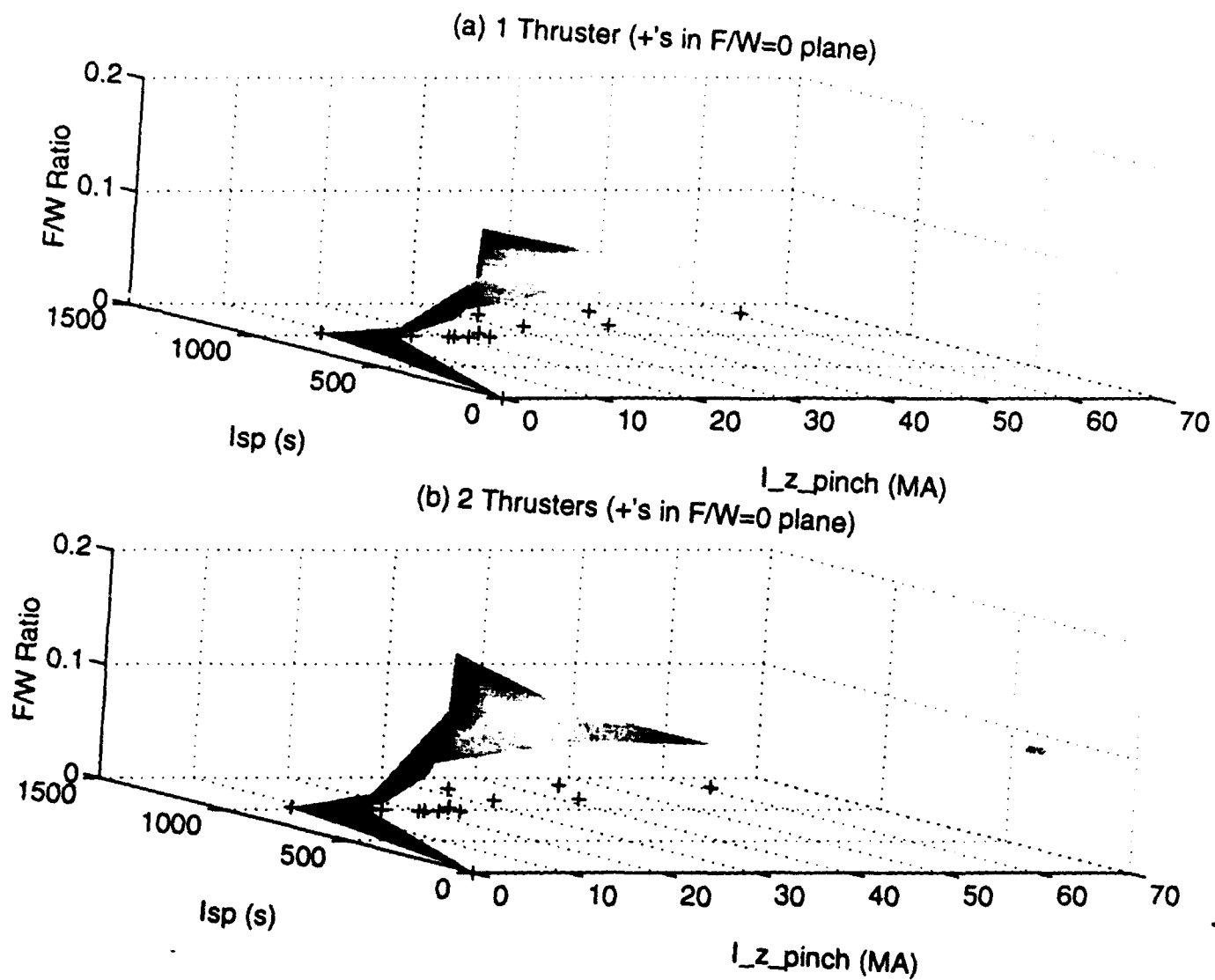


Figure A.25
Pinch Current, Specific Impulse, and F/W Ratio for Propellant Mass Flow Rate of 30.0 [kg/s] and $\Delta v = 10$ [km/s] with (a) 1 Thruster and (b) 2 Thrusters

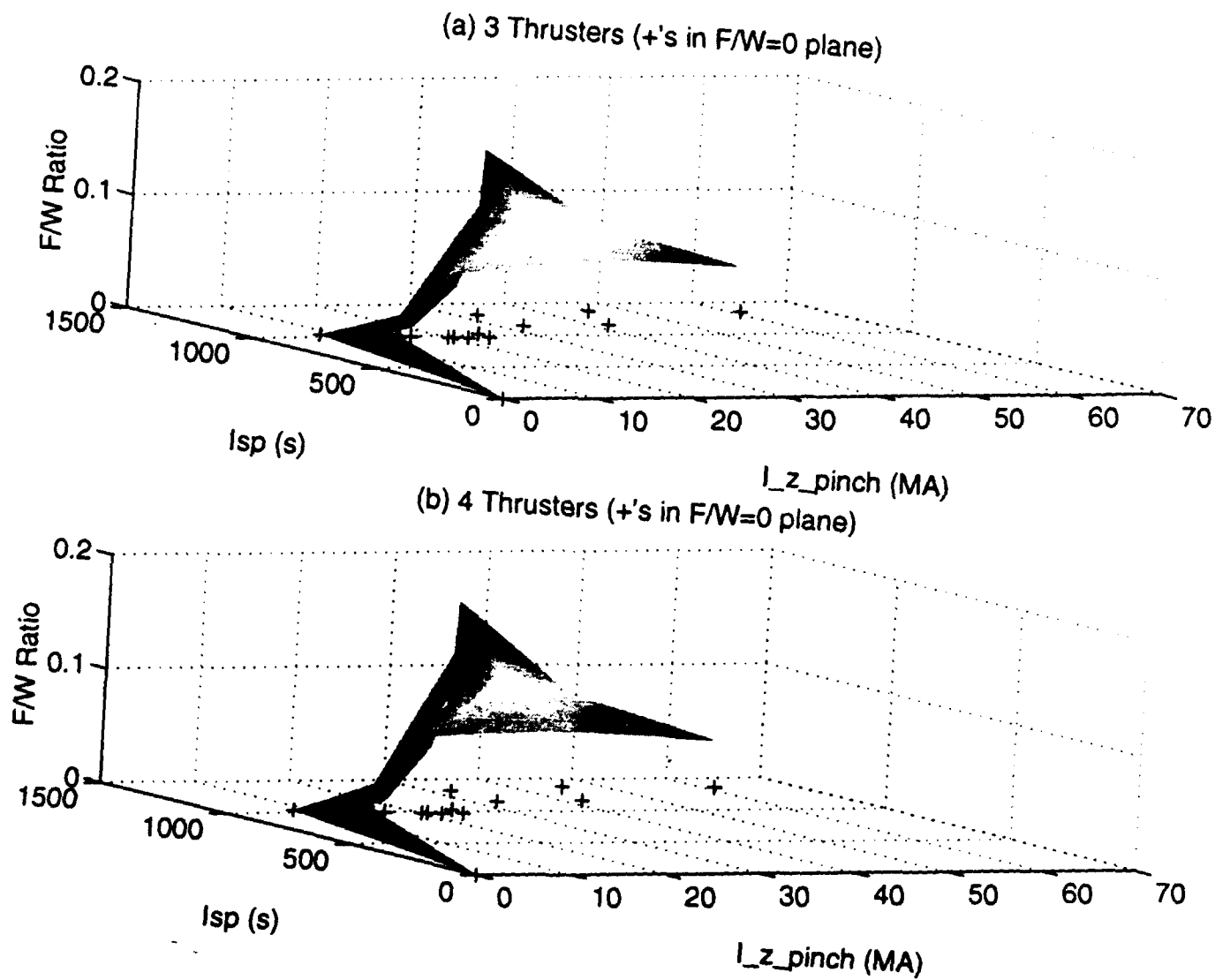


Figure A.26
Pinch Current, Specific Impulse, and F/W Ratio for Propellant Mass Flow Rate of 30.0 [kg/s] and $\Delta v = 10$ [km/s] with (a) 3 Thrusters and (b) 4 Thrusters

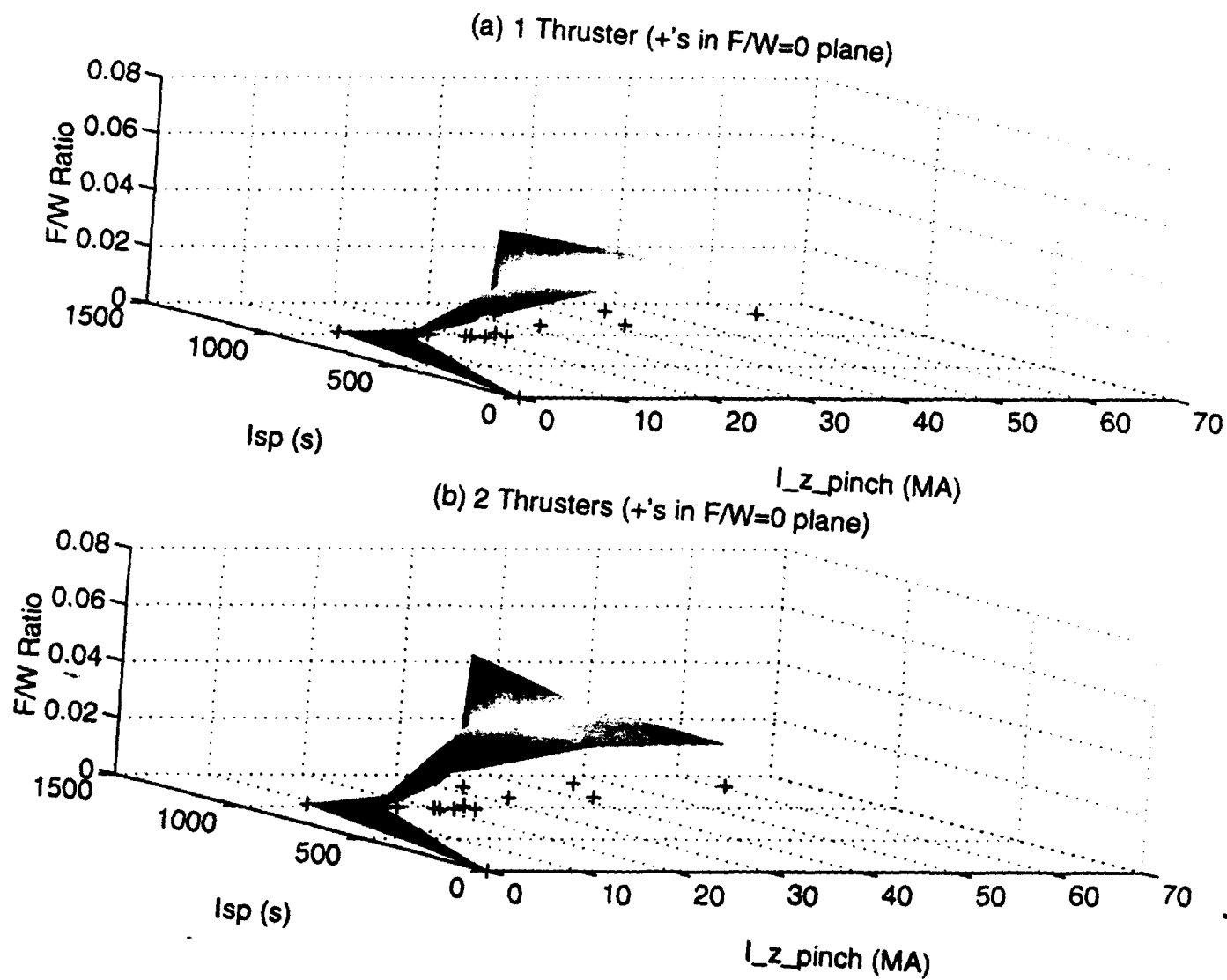


Figure A.27
Pinch Current, Specific Impulse, and F/W Ratio for Propellant Mass Flow Rate of 30.0 [kg/s] and $\Delta v = 20$ [km/s] with (a) 1 Thruster and (b) 2 Thrusters

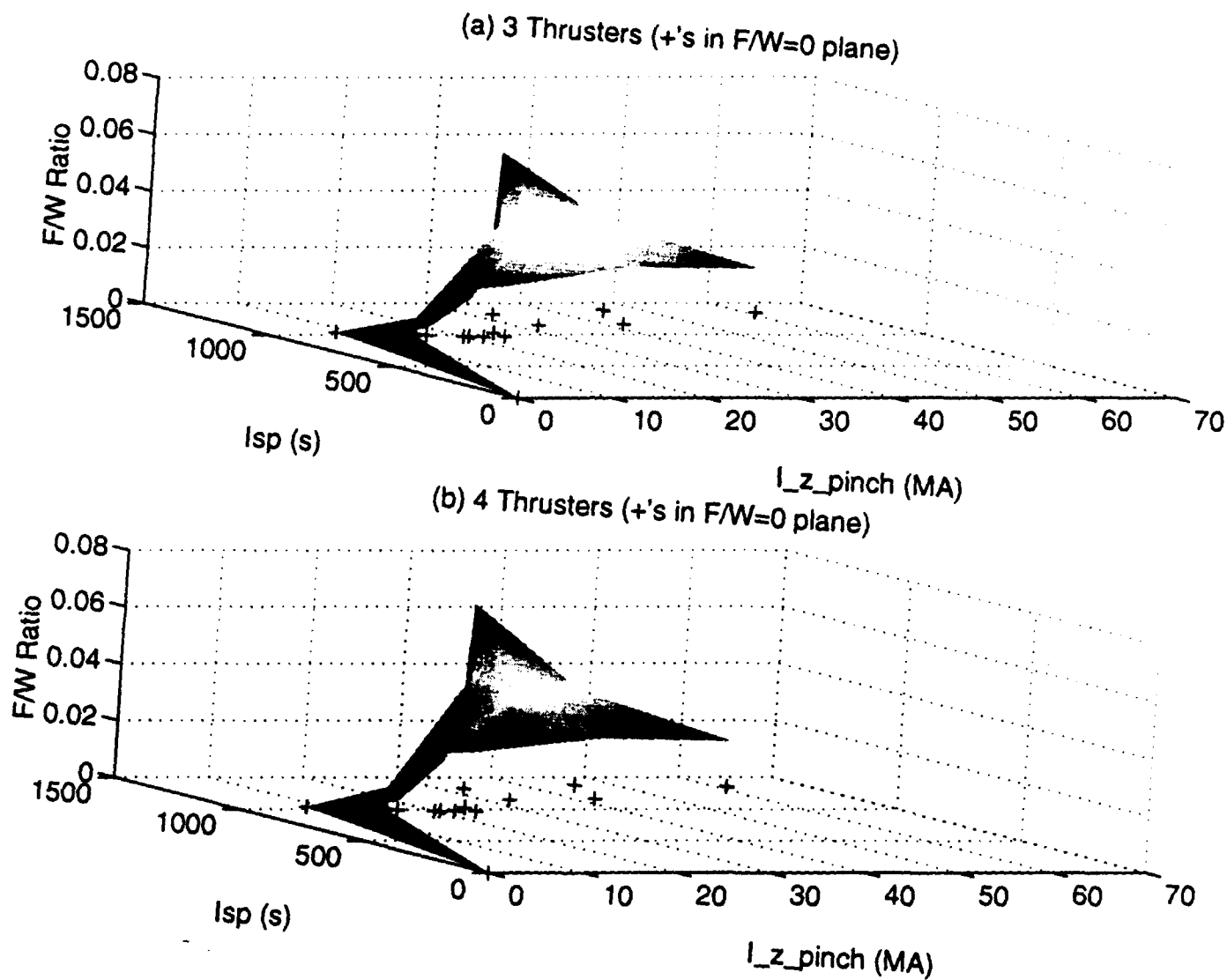


Figure A.28
Pinch Current, Specific Impulse, and F/W Ratio for Propellant Mass Flow Rate of 30.0 [kg/s] and $\Delta v = 20$ [km/s] with (a) 3 Thrusters and (b) 4 Thrusters

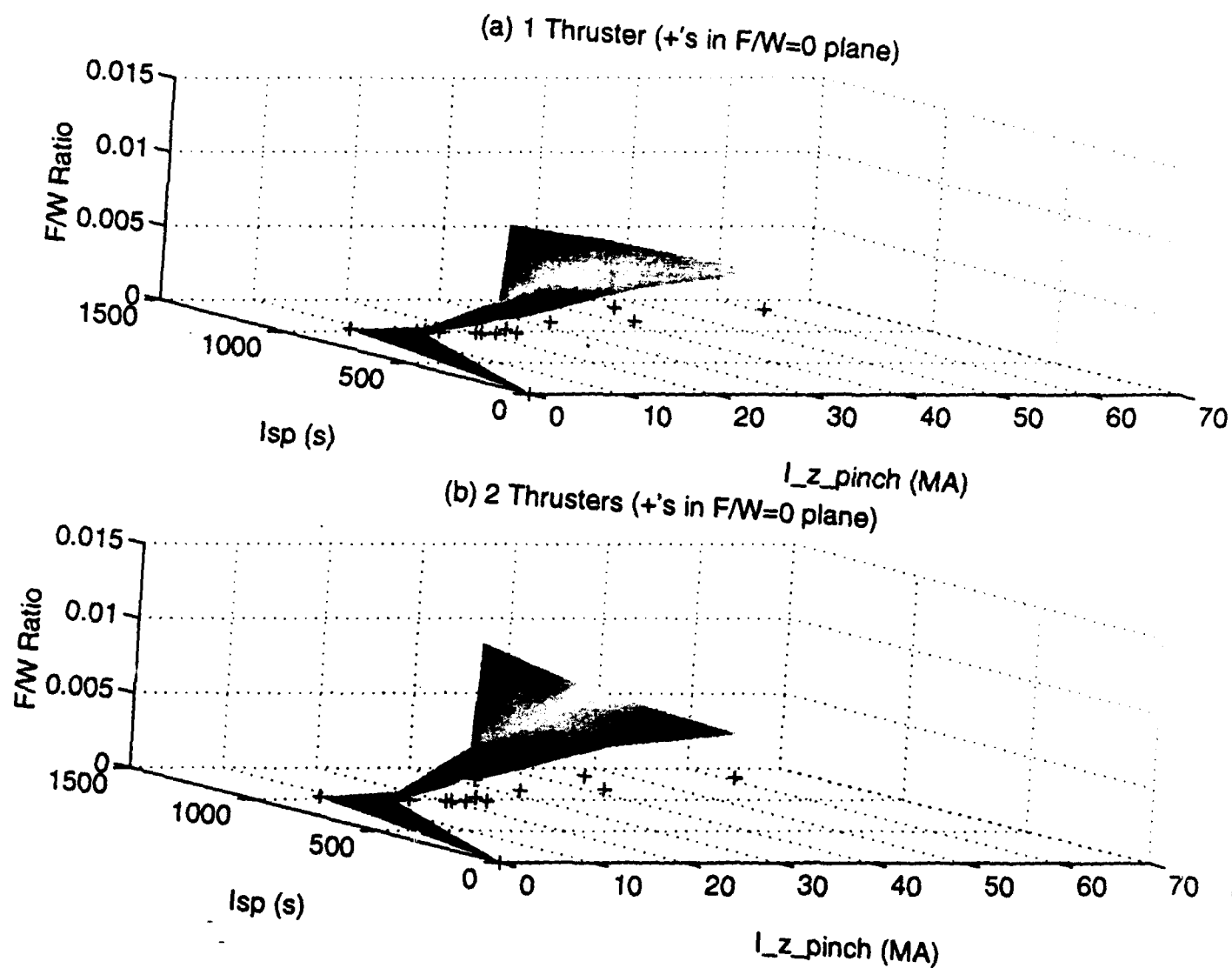


Figure A.29 -
Pinch Current, Specific Impulse, and F/W Ratio for Propellant Mass Flow Rate of 30.0 [kg/s] and $\Delta v = 40$ [km/s] with (a) 1 Thruster and (b) 2 Thrusters

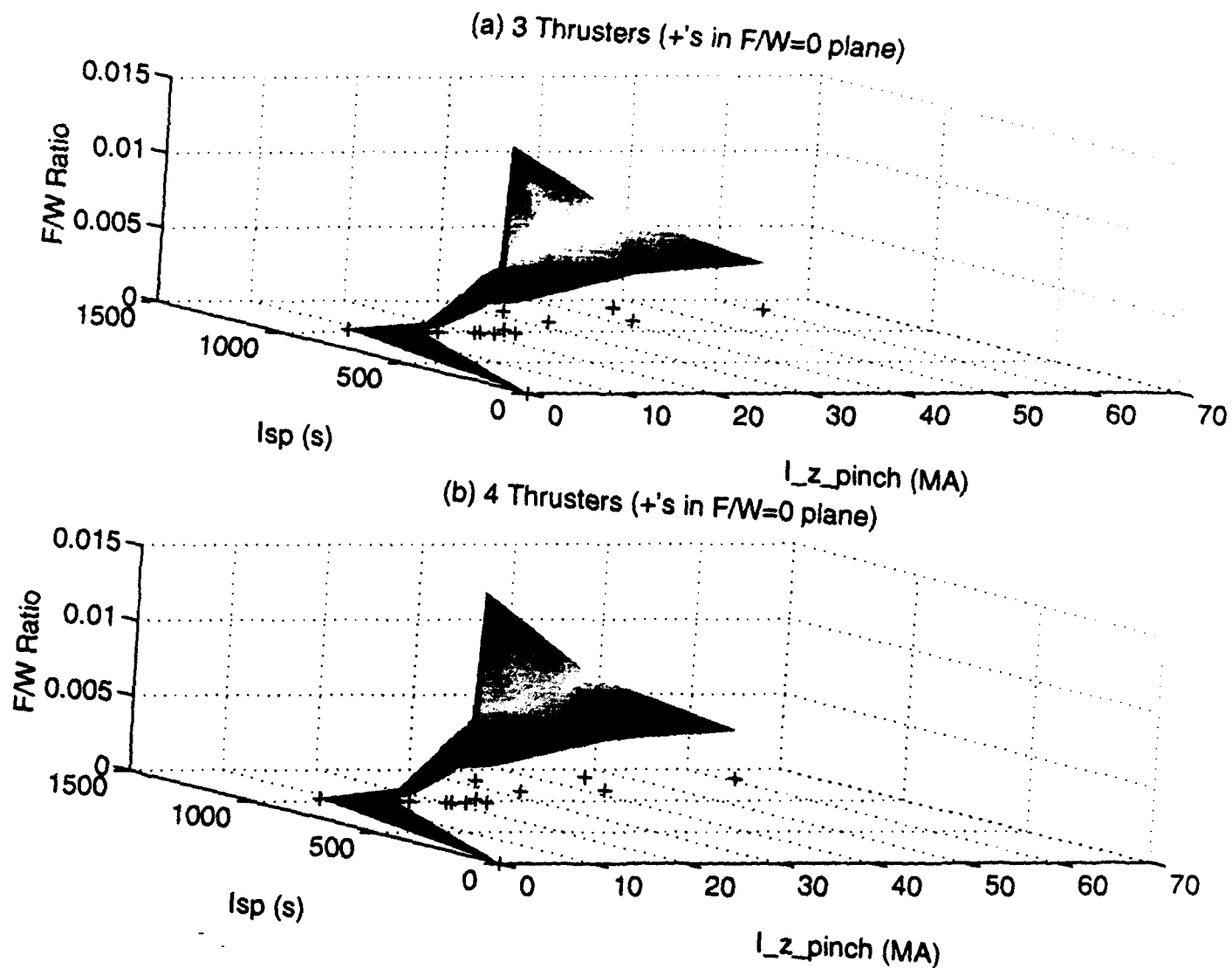


Figure A.30
Pinch Current, Specific Impulse, and F/W Ratio for Propellant Mass Flow Rate of 30.0 [kg/s] and $\Delta v = 40$ [km/s] with (a) 3 Thrusters and (b) 4 Thrusters

APPENDIX B

Presented on the following pages is the pinch calculation code used to determine the kinetic temperature and local magnetic field profiles throughout the pinch, as well as the axially averaged groupings of properties. Imbedded within the code is a subroutine used to determine the velocity profile values at each of the mesh points. Another FORTRAN code was used to create the input file containing the number density profile values at the mesh points. This input file was the only input file used with the pinch calculation code. The profile graphs were made using output data files from the pinch calculation code and imported into MATLAB to produce their graphical form.

C23456
 C Version created on 6 April 1994
 C
 C23456

PROGRAM DPF_RZ_HALF_RPROF

IMPLICIT NONE

INTEGER I, J, K, L, RDIV, ZDIV, IERR, CONV

PARAMETER (RDIV = 40)

PARAMETER (ZDIV = 20)

DOUBLE PRECISION CONST, TPREV, FACTN, FACTT, CURATZ, FACT
 DOUBLE PRECISION ZMAT(RDIV+1, ZDIV+1), NONHOM(RDIV+1)
 DOUBLE PRECISION ALPHA(RDIV+1), BETA(RDIV+1), DR, TFACT
 DOUBLE PRECISION SLOPE(RDIV+1, ZDIV+1), RSPACE(RDIV+1, ZDIV+1)
 DOUBLE PRECISION N(RDIV+1, ZDIV+1), T(RDIV+1, ZDIV+1)
 DOUBLE PRECISION VZ(RDIV+1, ZDIV+1), VR(RDIV+1, ZDIV+1)
 DOUBLE PRECISION DVZR(RDIV+1, ZDIV+1), DVZZ(RDIV+1, ZDIV+1)
 DOUBLE PRECISION DVRR(RDIV+1, ZDIV+1), DVRZ(RDIV+1, ZDIV+1)
 DOUBLE PRECISION RMID, ZMID, RRATIO, BTHETA(RDIV+1, ZDIV+1)
 DOUBLE PRECISION MASSD, KEVCON, E, AVTATZ, AVPDZ, TOTP, BEDGE
 DOUBLE PRECISION EPS, NU, MU0, RAL, AVVZZ, AVCUR, AVCURD, TCURD
 DOUBLE PRECISION NMAX, TMAX, PI, VDRIFT, AVNATZ
 DOUBLE PRECISION Z, BLOCAL(RDIV/2+1, ZDIV+1)
 DOUBLE PRECISION RWEIGH, AVT, TOT, DZ, SUMAVT, SUMAVN
 DOUBLE PRECISION CURENT, RADIUS, TOTN, AVN, TOTVZ, AVVZ, TPOWD
 DOUBLE PRECISION KTLOG, RRDHE3, RRDDN, RRDDP, POWDEN, RAV
 DOUBLE PRECISION AVPOWD, VOLUME, EHE3, EDDN, EDDP, POWFUS
 DOUBLE PRECISION OLD, RHIDE, NPREV

PARAMETER (E = 1.60219D-19)

PARAMETER (KEVCON = 1.60219D-16)

PARAMETER (MASSD = 3.343468D-27)

PARAMETER (PI = 3.141592654D0)

PARAMETER (MU0 = 4.D0*PI*1.D-7)

C
 C These energy outputs per reaction are in [J]
 C

EHE3 = 2.93166D-12

EDDN = 5.23854D-13

EDDP = 6.45606D-13

READ *, RMID

READ *, ZMID

READ *, RRATIO

READ *, NMAX

READ *, TMAX

READ *, VDRIFT

READ *, FACT

EPS = ZMID / RMID

NU = RRATIO

RAL = RMID / NU

C
 C READ in the solution matrices with B.C.'s and initial values

CALL BOUNDS(N, T)

OPEN (UNIT=1, FILE='output', STATUS='UNKNOWN')

OPEN (UNIT=3, FILE='tzpro', STATUS='UNKNOWN')

OPEN (UNIT=4, FILE='nzpro', STATUS='UNKNOWN')

OPEN (UNIT=5, FILE='trpro', STATUS='UNKNOWN')

OPEN (UNIT=9, FILE='nrpro', STATUS='UNKNOWN')

OPEN (UNIT=11, FILE='tzbeg', STATUS='UNKNOWN')

```

OPEN (UNIT=12, FILE='trbeg', STATUS='UNKNOWN')
OPEN (UNIT=21, FILE='bzloc', STATUS='UNKNOWN')
OPEN (UNIT=22, FILE='brloc', STATUS='UNKNOWN')
OPEN (UNIT=33, FILE='rdim', STATUS='UNKNOWN')
OPEN (UNIT=44, FILE='z', STATUS='UNKNOWN')
OPEN (UNIT=49, FILE='r', STATUS='UNKNOWN')
OPEN (UNIT=54, FILE='blocc', STATUS='UNKNOWN')
OPEN (UNIT=55, FILE='tp', STATUS='UNKNOWN')
OPEN (UNIT=56, FILE='np', STATUS='UNKNOWN')
OPEN (UNIT=60, FILE='avt', STATUS='UNKNOWN')
OPEN (UNIT=61, FILE='avn', STATUS='UNKNOWN')
OPEN (UNIT=62, FILE='avvz', STATUS='UNKNOWN')
OPEN (UNIT=63, FILE='avpd', STATUS='UNKNOWN')
OPEN (UNIT=64, FILE='zlen', STATUS='UNKNOWN')
OPEN (UNIT=70, FILE='zvals', STATUS='UNKNOWN')

DO 120 J = 1, RDIV/2+1
  DO 110 I = 1, ZDIV+1
    z = dble(i-1) * 2.d0*zmid / dble(zdiv)
    write (11,*) z, t(j,i)
    write (12,*) rspace(j,i), t(j,i)
110    CONTINUE
120 CONTINUE

C
C Fit the streamlines to the function  $r = A z^2 + B z + C$  and fill RSPACE
C and SLOPE matrices

CALL CURVE(SLOPE, RSPACE, RMID, ZMID, RRATIO)

DZ = 2.D0*ZMID / DBLE(ZDIV)

CALL VELOCITY(VZ, VR, DVZR, DVZZ, DVRR, DVRZ, SLOPE, DZ, RSPACE, CURENT, N,
& VDRIFT)

TCURD = 0.D0
RAV = 0.D0
SUMAVT = 0.D0
SUMAVN = 0.D0

DO 500 I = 1, ZDIV+1
  RADIUS = RSPACE(1,I)
  Z = DBLE(I-1) * 2.D0*ZMID / DBLE(ZDIV)
  WRITE (70,*) Z+0.01D0
  TOTT = 0.D0
  TOTN = 0.D0
  TOTVZ = 0.D0
  TOTP = 0.D0

  DO 390 J = 2, RDIV/2+1
    RWEIGH = RSPACE(J,I)
    TOTN = TOTN+N(J,I)*RWEIGH*(RSPACE(1,I)-RSPACE(2,I))
    TOTVZ = TOTVZ+VZ(J,I)*RWEIGH*(RSPACE(1,I)-RSPACE(2,I))
390    CONTINUE

  AVNATZ = 2.D0*TOTN / (RSPACE(1,I))**2.D0
  AVVZZ = 2.D0*TOTVZ / (RSPACE(1,I))**2.D0
C   print *, avvzz
  CURATZ = AVNATZ*AVVZZ*E*PI*RSPACE(1,I)**2.D0

C
C From Ampere's Law... (we get the vacuum B_theta value)...
  BTHETA(1,I) = MU0*CURATZ / (2.D0*PI*RSPACE(1,I))
C   PRINT *, I, CURATZ, BTHETA(1,I)
C
C From the beta = 1 condition at the edge...

```

```

C Since B_theta = 0 on the centerline axis...
  CONST = BTHETA(1,1)**2.D0*(2.D0/MU0)
  BTHETA(RDIV/2+1,1) = 0.D0
  T(RDIV/2+1,1) = CONST * N(RDIV/2+1,1)      KEVCON
  N(1,1) = 0.D0
  T(1,1) = 0.D0

DO 395 J = 2, RDIV/2
  BTHETA(J,1) = BTHETA(1,1) -
&              DBLE(J-1)/DBLE(RDIV/2) * BTHETA(1,1)
  T(J,1) = (CONST - BTHETA(J,1)**2.D0*(2.D0/MU0)) / N(J,1)
  T(J,1) = T(J,1) / KEVCON
395  CONTINUE

DO 400 J = 2, RDIV/2+1
  KTLOG = DLOG10(T(J,1))

  RRDHE3 = 0.35356D0*KTLOG**3.D0 - 3.3104D0*KTLOG**2.D0
&          + 10.105D0*KTLOG - 25.673D0
  RRDHE3 = 1.D-6*10.D0**RRDHE3
  RRDDN = 0.29811D0*KTLOG**3.D0 - 2.0830D0*KTLOG*KTLOG
&          + 5.7014D0*KTLOG - 22.0878D0
  RRDDN = 1.D-6*10.D0**RRDDN
  RRDDP = -0.053051D0*KTLOG**4.D0 + 0.57170*KTLOG**3.D0
&          - 2.4046D0*KTLOG*KTLOG + 5.6436D0*KTLOG
&          - 21.971
  RRDDP = 1.D-6*10.D0**RRDDP
  POWDEN = N(J,1)*N(J,1)*(RRDHE3*EME3/4.D0 +
&          RRDDP*EDDN/8.D0 + RRDDP*EDDP/8.D0)

  RWEIGH = RSPACE(J,1)
  IF (J.EQ.1) RWEIGH = 0.5D0 * RSPACE(J,1)
  TOTP = TOTP+POWDEN*RWEIGH*(RSPACE(1,1)-RSPACE(2,1))
  TOTT = TOTT+T(J,1)*RWEIGH*(RSPACE(1,1)-RSPACE(2,1))
  IF (J.EQ.2) RAV = RAV + 1.D0/2.D0*RSPACE(1,1)
  TOTN = TOTN+N(J,1)*RWEIGH*(RSPACE(1,1)-RSPACE(2,1))
C 400  CONTINUE

  AVNATZ = 2.D0 * TOTN / (RSPACE(1,1))**2.D0
  AVTATZ = 2.D0 * TOTT / (RSPACE(1,1))**2.D0
  SUMAVT = SUMAVT + AVTATZ*AVNATZ
  SUMAVN = SUMAVN + AVNATZ
  write (60,*) AVTATZ
  write (61,*) AVNATZ
  write (62,*) AVVZZ
  AVPDZ = 2.D0 * TOTP / (RSPACE(1,1))**2.D0
  write (63,*) AVPDZ
  write (64,*) Z
  TCURD = TCURD + AVNATZ*AVVZZ*E
  TPOWD = TPOWD + AVPDZ
500  CONTINUE

  RAV = 2.D0 * DZ * RAV / (2.D0*ZMID)
  AVCURD = 2.D0 * DZ * TCURD / (2.D0*ZMID)
  AVCUR = AVCURD * PI * RAV * RAV
  AVPOWD = 2.D0 * DZ * TPOWD / (2.D0*ZMID)
  AVN = SUMAVN / DBLE(ZDIV+1)
  AVT = SUMAVT / DBLE(ZDIV+1) / AVN
  VOLUME = PI * RAV * RAV * (2.D0*ZMID)
  POWFUS = AVPOWD * VOLUME

  WRITE(1,*) 'Average Radius = ',RAV,' [m]. '
  WRITE(1,*) 'Average Power Density = ',AVPOWD/1.D6,' [MW/m**3]. '
  WRITE(1,*) 'Pinch Volume = ',VOLUME,' [m**3]. '
  WRITE(1,*) 'Fusion Power Produced = ',POWFUS/1.D6,' [MW]. '

```

```

WRITE(1,*) 'Average Pinch Current = ',AVCUR,1.D6,' [MA]'
WRITE(1,*) 'Average Pinch Number Density = ',AVN,' [m**3]'
WRITE(1,*) 'Average Pinch Kinetic Temperature = ',AVT,' [keV]'
WRITE(1,*) 'Average Z Drift Velocity = ',AVVZ,' [m/s]'
WRITE(1,*) 'Overall Energy Density = ',AVN*AVT,' [J.m**3]'

C
C Print out the final form of the solution matrices
C
DO 600 J = 1,RDIV/2+1
  DO 590 I = 1,ZDIV+1
    z = dble(i-1) * 2.d0*zmid / dble(zdiv)
    write (4,*) z, n(j,i)
    zmat(j,i) = z
    write (9,*) rspace(j,i), n(j,i)
    write (3,*) z, t(j,i)
    write (5,*) rspace(j,i), t(j,i)
    write (33,*) z, rspace(j,i)
    WRITE (66,*) T(J,I)

    IF (J.GT.1) THEN
      write (21,*) z, blocal(j,i)
      write (22,*) rspace(j,i), blocal(j,i)
    ENDIF
590  CONTINUE
    write (44,591) (zmat(j,i),i=1,zdiv+1)
591  format (21(f6.4,1x))
    write (44,*)
    write (49,592) (rspace(j,i),i=1,zdiv+1)
592  format (21(f7.5,1x))
    write (49,*)
    write (54,595) (btheta(j,i),i=1,zdiv+1)
595  format (21(f7.1,1x))
    write (54,*)
    write (55,597) (t(j,i),i=1,zdiv+1)
597  format (21(f6.2,1x))
    write (55,*)
    write (56,599) (n(j,i),i=1,zdiv+1)
599  format (21(e9.3,1x))
    write (56,*)
600 CONTINUE

    PRINT *, 'N Matrix:'
C    DO 700 I = 1,ZDIV+1
C      PRINT *, 'n [m-3] Column Z = ',I
C      PRINT *, (N(L,I),L=1,RDIV/2+1)
C 700 CONTINUE

    PRINT *, 'T Matrix:'
C    DO 800 I = 1,ZDIV+1
C      PRINT *, 'kT [keV] Column Z = ',I
C      PRINT *, (T(L,I),L=1,RDIV/2+1)
C 800 CONTINUE

    CLOSE (UNIT=1)
    CLOSE (UNIT=3)
    CLOSE (UNIT=4)
    CLOSE (UNIT=5)
    CLOSE (UNIT=9)
    CLOSE (UNIT=11)
    CLOSE (UNIT=12)
    CLOSE (UNIT=21)
    CLOSE (UNIT=22)
    CLOSE (UNIT=33)
    CLOSE (UNIT=44)
    CLOSE (UNIT=49)
    CLOSE (UNIT=54)

```

```

CLOSE (UNIT=55)
CLOSE (UNIT=56)
CLOSE (UNIT=60)
CLOSE (UNIT=61)
CLOSE (UNIT=62)
CLOSE (UNIT=63)
CLOSE (UNIT=64)
CLOSE (UNIT=70)

```

```

STOP
END

```

```

C=====
C23456

```

```

SUBROUTINE BOUNDS(N,T)

INTEGER RDIV,ZDIV

PARAMETER (RDIV = 40)
PARAMETER (ZDIV = 20)

DOUBLE PRECISION N(RDIV+1,ZDIV+1),T(RDIV+1,ZDIV+1)

READ *, N
READ *, T

RETURN
END

```

```

C=====
C23456

```

```

SUBROUTINE CURVE(SLOPE,RSPACE,RMID,ZMID,RRATIO)

IMPLICIT NONE

INTEGER RDIV,ZDIV,I,J

PARAMETER (RDIV = 40)
PARAMETER (ZDIV = 20)

DOUBLE PRECISION SLOPE(RDIV+1,ZDIV+1),RSPACE(RDIV+1,ZDIV+1)
DOUBLE PRECISION RMID,ZMID,NU,EPS,Z,RVAL,RAL
DOUBLE PRECISION NUOLD,EPSOLD,SURFR(ZDIV+1)

EPS = ZMID / RMID
EPSOLD = EPS
NU = RRATIO
NUOLD = NU
RAL = RMID / NU

```

```

C
C Compute the curve fits and load the RSPACE and SLOPE matrices
C
C Load the LEFT END, and, therefore, the RIGHT END also:
C

```

```

SURFR(1) = RAL
SURFR(ZDIV+1) = RAL

DO 1000 J = 1,RDIV/2
  RSPACE(J,1) = RAL * DBLE(RDIV/2+1-J) / DBLE(RDIV/2)
  RSPACE(RDIV+2-J,1) = RSPACE(J,1)
  RSPACE(J,ZDIV+1) = RSPACE(J,1)
  RSPACE(RDIV+2-J,ZDIV+1) = RSPACE(J,1)
1000 CONTINUE

```

```

C
C Load the r = 0 R-AXIS:

```

```

C
DO 1020 I = 1,ZDIV+1
  RSPACE(RDIV/2+1,I) = 0.D0
  SLOPE(RDIV/2+1,I) = 0.D0
1020 CONTINUE

C
C Load the z = ZMID Z-AXIS (SLOPE values only):
C
DO 1030 J = 1,RDIV+1
  SLOPE(J,ZDIV/2+1) = 0.D0
1030 CONTINUE

C
C Load the TOP and BOTTOM boundaries:
C
DO 1050 I = 1,ZDIV-1
  Z = 2.D0 * ZMID * DBLE(I) / DBLE(ZDIV)
  RSPACE(1,I+1) = RVAL(NU,EPS,RAL,Z)
  SURFR(I+1) = RSPACE(1,I+1)
  RSPACE(RDIV+1,I+1) = RSPACE(1,I+1)
1050 CONTINUE

DO 1057 I = 2,ZDIV
  SLOPE(1,I) = (RSPACE(1,I+1)-RSPACE(1,I-1)) /
& (2.D0 * 2.D0 * ZMID * 1.D0 / DBLE(ZDIV))
1057 CONTINUE

C
C Load the remaining points:
C
DO 1080 I = 2,ZDIV
  DO 1070 J = 2,RDIV/2
    RSPACE(J,I) = SURFR(I)*DBLE(RDIV/2+1-J)/DBLE(RDIV/2)
    RSPACE(RDIV+2-J,I) = RSPACE(J,I)
1070 CONTINUE
1080 CONTINUE

DO 1100 I = 2,ZDIV/2
  DO 1090 J = 2,RDIV/2
    SLOPE(J,I) = (RSPACE(J,I+1)-RSPACE(J,I-1)) /
& (2.D0 * 2.D0 * ZMID * 1.D0 / DBLE(ZDIV))
    SLOPE(J,ZDIV+2-I) = -SLOPE(J,I)
    SLOPE(RDIV+2-J,I) = -SLOPE(J,I)
    SLOPE(RDIV+2-J,ZDIV+2-I) = SLOPE(J,I)
1090 CONTINUE
1100 CONTINUE

DO 1107 J = 2,RDIV/2
  SLOPE(J,1) = (RSPACE(J,2)-RSPACE(J,1)) /
& (2.D0 * ZMID / DBLE(ZDIV))
  SLOPE(RDIV+2-J,1) = -SLOPE(J,1)
  SLOPE(J,ZDIV+1) = -SLOPE(J,1)
  SLOPE(RDIV+2-J,ZDIV+1) = SLOPE(J,1)
1107 CONTINUE

SLOPE(1,1) = SLOPE(2,1) + SLOPE(2,1)-SLOPE(3,1)
SLOPE(1,ZDIV+1) = -SLOPE(1,1)
SLOPE(RDIV+1,1) = -SLOPE(1,1)
SLOPE(RDIV+1,ZDIV+1) = SLOPE(1,1)

OPEN (UNIT=1,FILE='rstuff',STATUS='UNKNOWN')
DO 1141 J = 1,RDIV/2+1
DO 1138 I = 1,ZDIV/2+1
  Z = 2.D0 * ZMID * DBLE(I-1) / DBLE(ZDIV)
  WRITE (1,*) Z,RSPACE(J,I)

```



```

1135 CONTINUE
1141 CONTINUE
DO 1147 J = 1,RDIV/2+1
DO 1145 I = 1,ZDIV/2+1
    Z = 2.D0 * ZMID * DBLE(I-1) / DBLE(ZDIV)
    WRITE (1,*) Z,SLOPE(J,I)
1145 CONTINUE
1147 CONTINUE
CLOSE (UNIT=1)

RETURN
END

```

```

C=====
C23456

```

```

DOUBLE PRECISION FUNCTION RVAL(NU,EPS,RAL,Z)

IMPLICIT NONE

DOUBLE PRECISION NU,EPS,RAL,Z

RVAL = (1.D0-NU)/(EPS*NU) * (Z*Z/(EPS*NU*RAL)-2.D0*Z) + RAL
RETURN
END

```

```

C=====
C23456

```

```

DOUBLE PRECISION FUNCTION DERIV(NU,EPS,RAL,Z)

IMPLICIT NONE

DOUBLE PRECISION NU,EPS,RAL,Z

DERIV = 2.D0*(1.D0-NU)/(EPS*NU) * (Z/(EPS*NU*RAL) - 1.D0)

RETURN
END

```

```

C=====
C23456

```

```

SUBROUTINE VELOCITY(VZ,VR,DVZR,DVZZ,DVRR,DVRZ,
& SLOPE,DZ,RSPACE,CURRENT,N,VDRIFT)

IMPLICIT NONE

INTEGER I,J,RDIV,ZDIV

PARAMETER (RDIV = 40)
PARAMETER (ZDIV = 20)

DOUBLE PRECISION E,CURRENT,VZ(RDIV+1,ZDIV+1),VR(RDIV+1,ZDIV+1)
DOUBLE PRECISION PI,DVZR(RDIV+1,ZDIV+1),DVZZ(RDIV+1,ZDIV+1)
DOUBLE PRECISION DVRR(RDIV+1,ZDIV+1),DVRZ(RDIV+1,ZDIV+1)
DOUBLE PRECISION SLOPE(RDIV+1,ZDIV+1),DZ,RSPACE(RDIV+1,ZDIV+1)
DOUBLE PRECISION N(RDIV+1,ZDIV+1),VDRIFT,FACTOR,VFACT(ZDIV+1)

PARAMETER (E = 1.602D-19)
PARAMETER (PI = 3.14159D0)

```

```

C DATA VFACT /0.80D0,0.76D0,0.71D0,0.65D0,0.68D0,0.73D0,0.77D0,
C & 0.83D0,0.88D0,0.93D0,0.97D0,1.02D0,1.05D0,1.07D0,
C & 1.08D0,1.09D0,1.12D0,1.15D0,1.13D0,1.17D0,1.20D0/
DATA VFACT /21*1.D0/

```

```

DO 2000 J = 1,RDIV+1
DO 1900 I = 1,ZDIV+1

```

```

        FACTOR = VFACT(I)
        VR(J,I) = SLOPE(J,I) * VDRIIFT * FACTOR
        VZ(J,I) = DSQRT((VDRIIFT*FACTOR)**2.D0 - VR(J,I)**2.D0)
C      if(i.eq.1)print*,rspace(j,i),slope(j,i),vz(j,i)
1900      CONTINUE
2000 CONTINUE

      DO 2200 J = 2,RDIV
        DO 2100 I = 2,ZDIV
          DVRR(J,I) = (VR(J+1,I)-VR(J-1,I)) /
&          (RSPACE(J+1,I)-RSPACE(J-1,I))
          DVRZ(J,I) = (VR(J,I+1)-VR(J,I-1)) /
&          (2.D0*DZ)
          DVZR(J,I) = (VZ(J+1,I)-VZ(J-1,I)) /
&          (RSPACE(J+1,I)-RSPACE(J-1,I))
          DVZZ(J,I) = (VZ(J,I+1)-VZ(J,I-1)) /
&          (2.D0*DZ)
          IF (J.EQ.RDIV/2+1) THEN
            DVRR(J,I) = 0.D0
            DVRZ(J,I) = 0.D0
            DVZR(J,I) = 0.D0
            DVZZ(J,I) = 0.D0
          ENDIF
2100      CONTINUE
2200 CONTINUE

      OPEN (UNIT=2,FILE='velout',STATUS='UNKNOWN')
      WRITE(2,*) 'DVRR'
      WRITE(2,*) DVRR
      WRITE(2,*) 'DVRZ'
      WRITE(2,*) DVRZ
      WRITE(2,*) 'DVZR'
      WRITE(2,*) DVZR
      WRITE(2,*) 'DVZZ'
      WRITE(2,*) DVZZ
      CLOSE (UNIT=2)

      RETURN
      END

```